Lancaster University

PhD Thesis

Terahertz Magnetic Dynamics in Rare-Earth Transition Metal Oxides

by

Mykola R. Vovk

Supervisor:

Dr. Rostislav V. Mikhaylovskiy

This thesis is submitted for the degree of

Doctor of Philosophy

December 2024

Abstract

Over the past decade, the field of terahertz driven magnetic phenomena has witnessed a remarkable surge of interest, particularly in the study of antiferromagnetic materials, which has emerged as a captivating sub-field within the area of ultrafast pump-probe spectroscopy studies.

This thesis is dedicated to theoretical and experimental studies of a specific class of magnetic oxides, namely rare-earth orthoferrites (REOs) and the magnetic crystal known as Terbium Gallium Garnet (TGG). These materials are characterised by a plethora of fascinating physical phenomena, including the occurrence of spin reorientation phase transitions (SRTP), which can be effectively manipulated and controlled through the use of THz driving/excitation.

The first two chapters of this thesis explain the motivations behind this research and provide an overview of the theoretical and experimental methods necessary for understanding the later chapters.

Chapter 3 develops the theoretical formalism used to describe THz-driven magnetic switching phenomena in rare-earth orthoferrites with non-Kramers ions. It provides insights into the dynamics induced by THz radiation on iron spins and analyses the mechanisms that facilitate the iron spin-switching process during the spin-reorientation phase transition in Thulium orthoferrite ($TmFeO_3$). Based on the available experimental data this chapter analyses static and dynamic properties of $TmFeO_3$ in the course of SRPT, explains the effects responsible for the spin switching behaviour and presents theoretical results with the realistic values of threshold fields necessary for achieving effective and minimally dissipative iron spin switching showing a good match with experimental findings.

Chapter 4 delves into our experimental results on the signatures of the magnetic analogue of the Jahn-Teller effect during the spin-reorientation phase transition in Terbium orthoferrite, ($TbFeO_3$), supported by a developed theoretical analysis. It also explores the features of the strong coupling regime between Fe and Tb ions, comparing $TbFeO_3$ with other strongly coupled systems as reported in previous research.

Chapter 5 describes the experimental comparison of THz- and optically-induced spin dynamics of Tb ions in Terbium Gallium Garnet ($Tb_3Ga_5O_{12}$). This crystal is well-known for its magneto-optical properties but lacks the specific magnetic order found in orthoferrites, making it an ideal candidate for investigating the features of low-temperature magnetism of pure Tb^{3+} ions unaffected by interactions with other magnetic ions.

The final chapter summarises our theoretical and experimental results obtained throughout this research. It provides an outlook of how these results correlate with

each other, and discusses future experimental and theoretical steps that emerged in the course of this work.

Acknowledgements

Here, I would like to take the opportunity to summarize the past four years of my life and express my sincere gratitude to all those who made this work possible. First and foremost, I am grateful to my supervisor, Dr. Rostislav Mikhaylovskiy, for giving me the opportunity to start a PhD in a completely new field for me. Rostislav, it has been a challenging time, but I truly appreciate the opportunity to learn from your unique expertise as both a theoretician and an experimentalist.

Secondly, I am indebted to all my colleagues from our group in Lancaster. I would like to extend special thanks to Dr. Oleksandr (Sasha) Kovalenko for his guidance, support, and for teaching me how to conduct pump-probe experiments. Sasha, you are an exceptional experimentalist with knowledge and skills far beyond the ordinary, and I sincerely hope you secure a permanent academic position soon. Moreover, it was comforting to have another countryman nearby during such turbulent times for our country and people. To my fellow PhD colleagues, Ruben Leenders and Yuichi Saito, thank you guys for your companionship and assistance in the lab and for the good times outside of it. I also would like to acknowledge Farhan Nur Kholid, a former postdoc, for his help and guidance during the first year of my PhD. Special thanks to Deborah Dunne, Post Graduate Research Coordinator in the Physics Department, and Shonah Ion, Departmental Superintendent, for their help and support throughout these years. Additionally, I would like to thank the teams in the Physics Department's mechanical and electronics workshops for their invaluable contributions to setting up the experiment and constructing parts of the setup. I would also like to express my sincere gratitude to Dr. Elena Ezerskaya and Dr. Aleksandr Ort, my lecturers and mentors from the Physics department of my alma mater KhNU, for their inexhaustible support, guidance, and interest in my research path since my early student years.

I am grateful to all my colleagues from other universities who participated in the COMRAD project. Our international meetings, conferences, and workshops were invaluable components of the project and my PhD journey. I especially want to acknowledge the participants from organizations where I had the opportunity to intern. Special thanks to Prof. Alexey Kimel from Radboud University in Nijmegen, Netherlands, for the opportunity to join his group for a one-month internship. My fellow PhD colleague, Dinar Khusyainov, thank you for teaching me the fundamentals of the magnetic force microscopy technique during my internship at Radboud University, and for the collaborative work on the data that resulted in the article we recently submitted. Timur Gareev, I appreciate your support during my stay in Nijmegen and your reciprocal visit to Lancaster University. Thanks to your

contribution, we managed to collect significant results from the DyFeO3 samples, which I believe will lead to an interesting publication soon. Lastly, I want to thank Alexandr Buzdakov for our collaborative theoretical work during my two visits to I-FEVS in Turin, Italy, and for your visit in the spring of 2024. Sasha, it has been a pleasure to work together and share our theoretical insights.

I am sincerely grateful to my friends here in the UK and Portugal, who have become dear to my family and me. Dr Volodymyr Khotkevych helped me immensely in starting my life in the UK and has guided me over the years along the “тернистий шлях” —of British academia. Dr Iryna Labunska and Victor Sologub are always very welcoming, supportive and helpful whenever I visit them in Exeter. Dr Sergiy Rozhko and Iryna Stupak-Rozhko, I am tremendously grateful for your constant interest in my PhD progress and for welcoming me into your cosy home in Orwell. Dr. Vitor Manuel Pinto Semões, caro amigo, cada vez que o visito em Portugal, é uma alegria e uma experiência maravilhosa. Obrigado por receber a mim e à minha família. To all these wonderful people, you have been a tremendous support during these turbulent times for me and other Ukrainians, and I am infinitely grateful to you!

Last but not least, I would like to thank my beloved family: my parents, Olga and Ruslan, my younger sibling, Svyatoslav, my godmother Tamara, and my cousin Sveta and her wonderful family. I am blessed to have you all, and this work is devoted to you!

Дорогі Мама, Тато, брат Святослав, Хрещена, Света і Все наше слобожансько-київське родинне коло! Немає таких слів, щоб виразити мою вдячність за Вашу любов, підтримку, та допомогу незалежно від часу і обставин, все що я маю та досяг є безпосередньо завдяки Вам!

Declaration

Hereby I affirm that this thesis, titled "Terahertz Magnetic Dynamics in Rare-Earth Transition Metal Oxides," is entirely the result of my own work, except as explicitly noted in quotations, and has not been submitted for any other academic distinction.

The work presented in this thesis was supported by the European Union Horizon 2020 research and innovation program under Marie Sklodowska Curie Grant Agreement No. 861300 Cold Opto-Magnetism for Random Access Devices (COMRAD) project.

The research findings presented in this thesis has resulted in or contributed to the following publications or publications in preparation at the time of writing:

- Chapter III. N.R. Vovk, E.V. Ezerskaya, R.V. Mikhaylovskiy, "Theory of THz-driven magnetic switching in rare-earth orthoferrites: the case of $TmFeO_3$" (*Physical Review B,* vol. 111, no. 6, pp. 064411 (2025), *selected as an Editor`s Suggestion*).
- Chapter IV. O.Yu. Kovalenko, N.R. Vovk, R.V. Mikhaylovskiy et al. "Terahertz spin dynamics across Jahn-Teller-like magnetic phase transition" (*in preparation*)
- Chapter V. N.R.Vovk, O.Yu. Kovalenko, R.V. Mikhaylovskiy et al. "Light-induced spin dynamics in $Tb_3Ga_5O_{12}$" (*in preparation*)

I also published works related to the field of magnonics and contributed to some other works within the field of ultrafast magnetism and spintronics during PhD course.

- O.V. Dobrovolskiy, N.R. Vovk et al. "Spin-wave eigenmodes in direct-write 3D nanovolcanoes", Appl. Phys. Lett. 2021, 118, 132405.
- Vovk, A.; Bunyaev, S.A.; Štrichovanec, P.; Vovk, N.R.; et al. "Control of structural and magnetic properties of polycrystalline Co_2FeGe films via deposition and annealing temperatures", Nanomaterials 2021, 11, 1229.
- R.A. Leenders et al., "Rare-earth mediated linear response of Fe^{3+} spins to THz-magnetic fields in $ErFeO_3$" (*submitted*)
- D. Khusyainov et al., "Laser-induced helicity and texture-dependent switching of nanoscale stochastic domains in a ferromagnetic film" (*submitted*)
- O.Yu. Kovalenko, N.R.Vovk, T.Gareev, R.V. Mikhaylovskiy et al. "THz spin dynamics in $DyFeO_3$" (*in preparation*)

Contents

List of conventional abbreviations and notations

AFM	antiferromagnet
AFMR	antiferromagnetic resonance
AO-HDS	All-optical helicity-dependent switching
BBO	beta Barium Borate
BS	beam splitter
CME	Cotton Mouton effect
DBS	dichroic beam splitter
DMI	Dzyaloshinskii-Moriya Interaction
EOS	Electro-optic (EO) Sampling
$ErFeO_3$	Erbium orthoferrite
FE	Faraday effect
FIR	far infra-red
FM	ferromagnet
GaP	Gallium phosphide
IFE	Inverse Faraday effect
IR	infra-red
LLG	Landau-Lifshitz-Gilbert
$LiNbO_3$	Lithium niobate
MCD	Magnetic circular dichroism
MLB	Magnetic linear birefringence
MOKE	Magneto-optical Kerr effect
NIR	near infra-red
PD	photodetectors
PSD	phase-sensitive detection
REO	rare-earth orthoferrites

SNR	signal-to-noise ratios
SPHE	spin-polarised hot-electrons
SRPT	spin reorientation phase transition
TGG /$Tb_3Ga_5O_{12}$	Terbium gallium garnet
THz	terahertz
THz-TDS	Terahertz time-domain spectroscopy
TP	Thermodynamic potential
$TbFeO_3$	Terbium orthoferrite
$TmFeO_3$	Thulium orthoferrite
WP	Wollaston prism
$YbFeO_3$	Ytterbium orthoferrite
ZnTe	Zinc telluride
q-AFM	quasi-ferromagnetic
q-FM	quasi-antiferromagnetic
$\lambda/2$	half-wave plate
$\lambda/4$	quarter-wave plate

List of symbols

$\vec{F}$ vector of ferromagnetism (net magnetisation) of Fe subsystem

$\vec{G}$ vector of antiferromagnetism (Neel) of Fe subsystem

$\vec{f}$ vector of ferromagnetism of R subsystem

$\vec{c}$ vector of antiferromagnetism

A isotropic *d-d* exchange

d Dzyaloshinskii constant

K_{ab}, K_{ac}, K_2, K_2', K_2'' crystallographic anisotropy constants

$\vec{M}_0$ magnetisation of the Fe sublattices

$\vec{H}$ magnetic field vector

$\vec{E}$ electric field vector

$\sigma^i_{\xi,\zeta}$ mean values of the Pauli matrices for the two-level system of R^{3+} ion

$\vec{\mu}^i_0$ magnetodipolar moment

Δ_{cf} energy splitting of the crystal field

Δ_R total energy splitting parameter

α polarisability coefficient

a isotropic *d-f* exchange interaction constant

b anisotropic *d-f* exchange interaction constant

λ_{ij} *f-f* exchange interaction constants

H Hamiltonian

Φ Thermodynamic potential

$\mathcal{L}$ Lagrangian

ξ, η, ζ indices for the axes to a local coordinate system of rare-earth sublattices

Chapter I. Introduction

1.1. Magnetism through the history

Lodestones in myths & legends. Magnetism has enchanted natural philosophers for more than three millennia, evolving from lodestone folklore to quantum field theory and nanoscale technology. Chinese chronicles place the earliest written evidence of magnetite in the *Book of the Devil Valley Master* (~4th c. BCE), which portrays a south-indicating lodestone spoon spinning on polished bronze [1]. Archaeologists have dated the "compass spoon" to as early as 2000 BCE [2]. In Europe, the etymology of *magnet* is traced to Magnesia in Anatolia, where Greek shepherd Magnes allegedly found iron nails sticking to his sandals. Homeric hymns invoke "stone of Hercules," while Indian Ayurvedic texts prescribe *aya-kashtha* (iron-wood) as a tonic [3]. These myths foreshadow two perennial themes: magnetism as marvel and as instrument. Pre-Socratic thinkers saw purposeful spirits in the stone. Thales (c. 600 BCE) ascribed lodestone's vitality to a soul-like essence [4], while animists such as Anaxagoras wove magnetism into elemental cosmography. By the 4th c. BCE mechanists—Leucippus, Democritus—proposed invisible *effluvia*. Lucretius Carus rendered these corpuscular chains in evocative Latin verse (1st c. BCE) describing "So strong the Magnet's virtue as it darts from ring to ring and knits the attracted parts" [6]. Yet neither school measured or predicted magnetism; explanation remained poetic.

Medieval compass & practical magnetism (8th–15th c.). Between China's Han dynasty and the Tang–Song transition, the floating "south-pointing fish" refined direction-finding for geomancy and maritime navigation [6]. By 1044 CE, Chinese military manuals illustrated an iron fish pivoting toward the south. Islamic scholars transmitted the device westward; Al-Ashraf's treatise (1282 CE) records a dry pivot compass [7]. In Europe, Pierre Peregrinus de Maricourt authored his *Epistola de Magnete* (1269), mapping poles, demonstrating attraction/repulsion symmetry, and inventing the *terrella*, a small spherical magnet modelling Earth [8].

The first experimental treatise, Gilbert's *De Magnete* (1600), declared Earth itself a giant magnet and rejected folkloric superstitions ("onions and garlic ruin compass needles" — they do not) [9]. René Descartes answered with a mechanistic theory of *parties cannelées*—threaded particles streaming through one-way ducts (1644) [10]. In the 18th c. electricity and magnetism were cast as *fluids*. Gray's conduction experiments (1729) prompted Benjamin Franklin's "one-fluid" model;

Franz Aepinus (1759) adapted it to magnetism [11]. Rival "two-fluid" views by du Fay, Wilcke and Brugmans labelled poles *austral* and *boreal*. The decisive step was Coulomb's torsion balance (1785) confirming an inverse-square force between magnetic poles and positing molecular polarisation [12]. Siméon-Denis Poisson then framed magnetostatics with a scalar potential V (1824) [13].

19th – 20th centuries. On 21 April 1820, Hans Christian Ørsted watched a current jolt a compass needle—linking electricity and magnetism [14]. Within months Arago, Ampère, Biot and Savart quantified the phenomenon. Ampère proposed microscopic circulating currents producing magnetism; Weber and Ewing refined molecular models. Michael Faraday pursued field lines, discovering diamagnetism and the rotation of polarisation (1845) [15]. James Clerk Maxwell unified Faraday's experimental findings with mathematics by formulating his famous equations, which demonstrated that electric and magnetic fields are aspects of a single fundamental force—electromagnetism—and that light is an electromagnetic wave, thereby linking optics with electromagnetism [16].

Gas-discharge studies led G. Johnstone Stoney to coin term "electron" (1874) and J. J. Thomson to measure it (1897) [17]. Pieter Zeeman discovered split of spectral lines due to the action of external magnetic field (1896) and H. A. Lorentz theoretically explained it [18]. Pierre Curie's systematic measurements yielded susceptibility χ and identified a critical temperature, the Curie point [19]. Paul Langevin explained diamagnetism as Lenz-induced electron orbits and paramagnetism as thermal alignment of permanent moments [20]. Pierre Weiss introduced "molecular field" concept in 1907 to explain ferromagnetism, where the internal magnetic field within a material is proportional to the magnetisation of the material, and established the Curie–Weiss law: $\chi = C/(T - T_C)$ [21].

In the beginning of 20th century new experimental and theoretical foundations appeared: Stern–Gerlach split silver-atom beams, proving space quantisation (1922) [22]. Pauli proposed the electron's intrinsic spin and exclusion principle, defining the Bohr magneton μ_B (1920) [23]. Heisenberg (1928) derived exchange interaction J force from quantum overlap, while Dirac merged relativity and spin, predicting the positron [24]. Felix Bloch identified spin waves (magnons) and derived his $T^{3/2}$ magnetisation law (1930) [25]. Louis Néel conceived antiferromagnetism with negative J between two sublattices [26].

Band, domain & micromagnetic Pictures (1930–1980). Stoner and Slater advanced itinerant-electron ferromagnetism, using band filling to rationalize Ni–Cu

alloys and predicting a Stoner criterion for spontaneous polarisation [27]. Landau and Lifshitz (1935) and W.F. Brown Jr. (1962) independently formulated the equations describing the domain wall motion; Barkhausen clicks (1919) supplied experimental proof [28]. Heisenberg sketched domain theory for Co; Bloch, Landau, Becker and Bozorth elaborated micromagnetics, culminating in Thiele's analytic treatment of bubble domains (1969) and Callen–Josephs simplification (1971) [29]. Bubble memory—cylindrical domains in orthoferrite films—became a 1970s data-storage technology [30]. Dilute magnetic alloys spurred conceptual revolutions. J. Friedel questioned why certain impurities keep local moments in Cu [31]; P. W. Anderson modelled the impurity level hybridizing with the conduction band (1961) [32]. Jun Kondo explained the low-temperature resistance minimum via antiferromagnetic *s–d* exchange and logarithmic scattering (1964) [33]; K. G. Wilson's renormalization group (1975) and Andrei/Wiegmann Bethe-ansatz solutions (1980–81) closed the many-body circle [34,35]. Low dimensions forced new paradigms. Onsager's exact 2-D Ising solution (1944) prefigured Mermin–Wagner's theorem forbidding 2-D Heisenberg order at finite T (1966) [36]. The Berezinskii–Kosterlitz–Thouless transition revealed topological vortices as order parameters (1973) [37]. Work by Stanley & Kaplan (1966) underscored the richness of XY models.

Magnetism in superconductivity & spintronics (1987 → Nowadays). The discovery of high-temperature superconductivity made by Bednorz & Müller (1986) [38] raised a fundamental question about nature of the superconductivity, not fitting into BCS [39] - the theory of superconductivity made in (1957). Neutron work by Tranquada exposed charge and spin stripes in CuO_2 planes linking magnetism to superconducting pairing [37]. Meanwhile, Albert Fert (1988) and Peter Grünberg (1989) discovered giant magnetoresistance, launching spintronics field; dense perpendicular-recording disks (Seagate 2005) echo magnetic-bubble physics. Magnetic semiconductors, first studied by Methfessel & Mattis (1960s), returned as Dilute Magnetic Semiconductors (GaMnAs, 1990s) for spin-valves and logic [40]. Ab-initio density-functional calculations (Kohn–Sham, 1965; LDA + U, 1990s) now predict magnetic order and anisotropy from first principles. Single-domain magnetite nanoparticles power the orientation of magnetotactic bacteria, salmon, sea turtles and possibly migratory birds [41]. Ferrimagnetic greigite (Fe_3S_4) fulfils a similar role. On planetary scales, convection of Earth's liquid iron core drives the geodynamo; paleomagnetic stripes recorded on ocean floors underpinned plate-tectonic theory [42].

Technological advancements & modern applications.

The commercial patenting of ferrites in 1909 ushered in a new age of magnetic materials engineering. Soft ferrites now permeate power electronics: transformers, inductors and electromagnetic-interference filters that raise energy efficiency and suppress noise in consumer devices and electric-vehicle drivetrains. Hard ferrites provide robust permanent magnets for wind-turbine generators, loudspeakers and computer hard-disk actuators, reinforcing the twin revolutions in renewable energy and data storage [43].

Today's frontier technologies increasingly couple magnetism to other degrees of freedom. In biotechnology, super-paramagnetic nanoparticles guide chemotherapeutics directly to tumours and sharpen the contrast in magnetic-resonance imaging (MRI). In micro- and nano-electronics, magneto-resistive effects underpin non-volatile memories; recent NiO-based devices even exploit voltage-controlled magnetic modulation to boost endurance and speed [44]. **Magnonics**—the use of magnons (spin-wave quanta) as information carriers—promises logic circuits that dissipate orders-of-magnitude less heat than charge-based transistors [45]. Finally, **spintronics**, which manipulates the electron's spin alongside its charge, has evolved from giant-magnetoresistance read-heads to racetrack memories and spin-transfer-torque MRAM, targeting ultrafast, energy-efficient data centres.

1.2. Ultrafast magnetic recording technology

The foundational work of Lev Landau and Evgeny Lifshitz, in which they introduced their famous dynamical equation [46,47], provided theoretical insights into how magnetisation responds to external stimuli over microsecond to millisecond timescales. However, major experimental advancements became possible only with the development of femtosecond (fs) lasers in 80`s [48]. The 1990s marked a significant shift with the discovery of ultrafast magnetisation dynamics triggered by femtosecond laser pulses. This breakthrough, made by Beaurepaire et al. [49], revealed that magnetisation could be manipulated on timescales far shorter than previously considered possible, leading to rapid demagnetisation within picoseconds of laser exposure paving a new way to approach ultrafast magnetic recording technologies [50].

1.2.1. Role of thermal and nonthermal effects in magnetisation

Understanding the role of thermal and nonthermal effects in magnetisation dynamics is crucial for the advancement of ultrafast magnetic recording technologies. Initially, it was believed that thermal effects, primarily laser-induced

heating, dominated the ultrafast demagnetisation process. However, recent studies have highlighted the significance of nonthermal effects, such as direct interactions between laser electromagnetic fields and the electronic structure of magnetic materials, which can alter magnetisation without significant heating [50]. This distinction is vital for designing more efficient magnetic recording technologies, as nonthermal effects allow for precise magnetisation control with reduced energy input. The following subsections explore these effects in more detail.

Thermal effects involve heat generation in laser-driven ferromagnetic systems, as modelled in ultrafast thermodynamics frameworks. These models help understand heat dissipation in materials like FeNi and CoFeB thin films, providing insights into controlling heat production in magnetic systems [51]. The three-temperature model, which considers electron, spin, and lattice reservoirs, is used to simulate ultrafast demagnetisation in materials like body centered-cubic Fe and face centered-cubic Co. This model shows that lattice dynamics, particularly lattice damping, significantly influence magnetisation dynamics [52].

Nonthermal effects include the transport of ultrashort spin-polarised hot-electrons (SPHE), which can manipulate magnetisation in ferrimagnetic alloys. These effects are characterised by spin transfer torque and thermal fluctuations induced by SPHE, as observed in $Fe_{74}Gd_{26}$ films [53]. Coherent magnetisation dynamics studies in nickel films reveal that nonthermal effects, such as spin wave excitations, play a crucial role in the remagnetisation process after ultrafast demagnetisation [54].

Below, we provide a few recent examples of research directions in the area of ultrafast magnetisation recording using thermal or nonthermal mechanisms.

1.2.2. All-optical helicity-dependent switching (AO-HDS)

All-optical helicity-dependent switching (AO-HDS) represents a significant advancement in magnetic recording technologies by enabling the control of magnetisation direction using the helicity of laser light, without external magnetic fields. This technique offers a faster and more energy-efficient method for data writing, with switching events occurring in less than 20 ps and heat loads below 6 J/cm^3 [55].

Mechanisms of AO-HDS

1. **Inverse Faraday effect and Magnetic circular dichroism**: AO-HDS primarily relies on the inverse Faraday effect (IFE) and magnetic circular dichroism (MCD) to induce magnetisation switching. The IFE generates a magnetic moment within the material, enhancing the switching probability, while MCD ensures helicity-dependent absorption. This leads to distinct electron temperatures and magnetisation quenching, effectively controlling the magnetisation state [56].
2. **Landau-Lifshitz-Gilbert equation**: The optical control of magnetisation via AO-HDS can be described using the Landau-Lifshitz-Gilbert (LLG) equation, where ultrashort optical pulses induce a helicity-dependent torque. This facilitates rapid and precise changes in magnetisation, allowing for efficient and controlled switching [57].

Material and laser specifics

1. **$NiCo_2O_4$ thin films**: Demonstrating practical applications at room temperature, $NiCo_2O_4$ thin films exhibit helicity-dependent AOS. The switching efficacy is influenced by laser pulse characteristics and the operational temperature, showcasing the adaptability of AO-HDS in real-world applications [58].
2. **GdFe alloys and other materials**: Different materials, such as GdFe alloys, show varying responses to AO-HDS. The minimum achievable bit size for these materials is around 25 nm, which is governed by factors such as ultrafast lateral electron diffusion and optical damage thresholds. This highlights the material-specific considerations necessary for optimising AO-HDS [59].

Speed and efficiency

AO-HDS can achieve magnetisation switching within 1-10 ps, making it a highly promising candidate for ultrafast data storage technologies. The process's efficiency and speed are heavily dependent on the specific material and laser properties, with some materials requiring multiple pulses for effective switching, emphasising the need for tailored approaches in different application scenarios [60].

1.2.3. Hot-electron pulses

Hot electrons, generated by intense laser pulses or electrical currents, can effectively and efficiently manipulate the magnetisation state. When electrons in a material are excited to higher energy states, they can transfer their angular

momentum to the magnetic lattice, altering its magnetic state. This process, demonstrated in materials like GdFeCo [61], enables for magnetisation reversal within 40 picoseconds, highlighting the potential of hot-electron pulses for ultrafast magnetisation control. This method is particularly promising for nanoscale spintronic devices due to its efficiency and the potential for integration without external magnetic fields.

Mechanisms of hot-electron pulses

1. **Spin-polarised hot electrons**: Femtosecond laser pulses can generate spin-polarised hot electrons, which play a crucial role in ultrafast demagnetisation and magnetisation switching. These electrons can induce spin transfer torque and thermal fluctuations, leading to changes in magnetisation states in materials. This demonstrates the significant potential of hot-electron pulses in manipulating magnetisation states, offering promising applications in spintronics.

2. **Wave function engineering**: In two-dimensional ferromagnets, ultrafast magnetisation can be achieved by controlling the spatial distribution of electron wavefunctions, rather than changing the carrier density. This method, known as wavefunction engineering, allows for sub-picosecond magnetisation manipulation, further expanding the capabilities of hot-electron pulses in advanced material systems [56].

Applications in spintronics

1. **Skyrmion-based data storage**: The manipulation of skyrmion magnetisation through high-speed carrier injections offers a robust and scalable solution for data storage. Spin-polarised electrons can dynamically change the topological state of skyrmions, enabling bitwise data storage. This application showcases the potential of hot-electron pulses in developing next-generation data storage technologies [62].

2. **Synthetic antiferromagnets**: In Co/Pt-based synthetic antiferromagnets, hot-electron spin currents assist in magnetisation switching, providing a method for ultrafast control of information operations in spintronic applications. This further underscores the versatility and efficiency of hot-electron pulses in complex magnetic systems [63].

1.2.4. Nonthermal photo-magnetic recording

Ultrafast nonthermal photo-magnetic recording in transparent media, such as ferrimagnetic cobalt-substituted garnet films, represents another emerging approach that promises to advance magnetic recording. This approach uses ultrafast laser pulses to induce changes in the magnetic state of a material without significant heating, thus maintaining the integrity of the material while achieving efficiency of magnetic recording. The technique leverages nonthermal pathways, where light-matter interactions induce changes in magnetic properties through mechanisms other than heat, such as coherent optical control and photoinduced phenomena. This method is particularly advantageous as it avoids the detrimental effects of thermal processes, thus preserving the material's longevity and performance [64].

Nonthermal pathways in magnetic recording

1. **Interaction mechanisms**: Nonthermal effects are achieved through ultrafast light-matter interactions that modify the magnetic state without heating. These interactions can result in transient modifications to the material's free-energy landscape, affecting quasiparticle populations and coupling strengths, which play a crucial role in the dynamics of magnetisation [65].
2. **Control methods**: In metallic ferromagnets, linearly polarised light can control magnetisation dynamics through optical rectification, which modulates magnetic energy via electrostriction-induced strain [66]. Additionally, the use of femtosecond laser pulses in multiferroic materials can amplify photomagnetic coupling, allowing for efficient optical control of magnetisation dynamics [67].

Advantages of nonthermal techniques

Material integrity and efficiency: Nonthermal methods prevent the thermal degradation of materials, ensuring longer-lasting magnetic properties and reducing energy consumption [66,67]. These techniques enable ultrafast control of magnetisation, significantly improving the speed and repetition rate of magnetic recording processes.

Challenges. Differentiation and analysis**:** identifying and isolating nonthermal effects from thermal ones can be challenging, requiring advanced techniques like time-resolved resonant magnetic X-ray diffraction. The integration of various ultrafast spectroscopy techniques can provide deeper insights into nonthermal phase transitions and their underlying mechanisms [50,68].

1.2.4. Antiferromagnetic spintronics

Antiferromagnetic spintronics is an emerging field that leverages the unique properties of antiferromagnetic materials for advanced spintronic applications. Unlike ferromagnetic materials, antiferromagnets do not produce stray magnetic fields, allowing for denser data storage. Moreover, the manipulation of antiferromagnetic order by external radiation (like optical or THz pump pulses) enables ultrafast switching speeds (in the THz range) and potentially greater stability against magnetic disturbances. These features make antiferromagnetic materials highly suitable for future spintronic devices where speed, density, and stability are crucial [69].

Key aspects of antiferromagnetic spintronics

1. **Spin-polarised antiferromagnetic metals.** Combining the benefits of spin polarisation with the absence of net magnetisation, these materials offer high electrical and thermal conductivities. They support strong interactions between charge transport and magnetic spin textures, crucial for spintronic applications [70]. This characteristic enables ultrafast switching speeds (in the THz range) and potentially greater stability against magnetic disturbances, making them highly suitable for future spintronic devices where speed, density, and stability are crucial.

2. **Current-induced switching and spin textures.** The ability to manipulate spin textures and the Néel vector through current-induced switching has been demonstrated in various antiferromagnetic films and bilayers. This technique enables efficient control of spin states, with the small size and topological stability of antiferromagnetic spin textures enhancing their attractiveness for applications. However, reading their magnetic state remains a challenge [71].

3. **Antiferromagnetic tunnel junctions (AFMTJs).** AFMTJs utilize the Néel vector as a state variable, allowing for efficient electric control and detection. These junctions can achieve large tunneling magnetoresistance effects and faster switching speeds compared to conventional magnetic tunnel junctions [72].

1.3. Theoretical background

Magnetic interactions. Understanding microscopic magnetic interactions is crucial for analysing the complex behaviour of materials under various magnetic

conditions. These interactions at the microscopic level dictate the magnetic properties of materials, influencing everything from basic magnetic alignment to complex phenomena like magnetic resonance and domain formation. This section explores several key types of magnetic interactions that significantly impact material properties, complemented by corresponding mathematical descriptions and characteristics drawn from the literature [73–75].

1.3.1. Exchange interaction

The exchange interaction in physics is a quantum mechanical phenomenon and is the strongest form of magnetic interaction. It arises from the indistinguishable nature of particles, like electrons, and the Pauli exclusion principle. It governs how the spin of one particle influences the spin of another, leading to magnetic ordering in materials. It originates from the Coulomb repulsion between electrons and their spin alignment. According to the Pauli exclusion principle, two fermions (e.g., electrons) cannot occupy the same quantum state. When two electrons are close to each other, their wave function becomes either symmetric (parallel spins) or antisymmetric (antiparallel spins). If the spins are aligned parallel (symmetric wave function), the electrons tend to spatially separate to reduce Coulomb repulsion, lowering their overall energy. Conversely, when the spins are antiparallel (antisymmetric wave function), the electrons can occupy the same region of space, which may increase the Coulomb energy. This energy difference gives rise to the exchange energy, which determines whether a material exhibits ferromagnetism (parallel spins) or antiferromagnetism (antiparallel spins).

1.3.2. Dzyaloshinskii-Moriya interaction (DMI)

The DMI is a form of antisymmetric exchange interaction. It is essential for understanding non-collinear spin structures in systems with broken inversion symmetry. This interaction was first described phenomenologically by Igor Dzyaloshinskii as a relativistic adjustment to the standard exchange interaction [76] and later Moriya [77] identified spin-orbit coupling as the microscopic mechanism of the antisymmetric exchange interaction. DMI is crucial in systems exhibiting weak ferromagnetism. It facilitates a minor canting of spins, leading to more complex magnetic phenomena such as the creation of skyrmions—small, topologically stable vortices that hold great promise for future uses in data storage and spintronics.

1.3.3. Zeeman interaction

The Zeeman interaction describes the effect of an external magnetic field on the energy levels of a magnetic system, such as electrons, atoms, or nuclei with magnetic moments, influenced by factors like light-induced electromagnetic waves [78]. This interaction occurs due to the coupling between the magnetic moment $\vec{\mu}$ of a particle with an external magnetic field $\vec{H}$, leading to a splitting of energy levels, a phenomenon known as the Zeeman effect. This alignment alters the atom's energy states and can be significantly affected by external influences such as light, which can modify the effect of the magnetic field.

1.3.4. Magnetic anisotropy

Magnetic anisotropy describes the directional dependence of a material's magnetic properties. It can arise from various sources such as dipolar interactions, which are responsible for the shape of anisotropy, magneto-crystalline anisotropy arising from the spin-orbit coupling and the structure of the crystal lattice, and magnetoelastic anisotropy, which directly depends on the stress applied to the material. This interaction is vital for the stability of magnetic storage media, as it defines the energy barriers that need to be overcome to reorient magnetic domains.

1.3.5. Dipolar interaction

This interaction involves forces between magnetic dipoles based on their distance and orientation relative to each other. It affects domains and domain wall formation in ferromagnetic materials, playing a key role in their macroscopic properties.

Table I below provides a comparative analysis of the strength and range of all mentioned interactions, including the formulas used for their description:

Table I

Name	Strength and Range	Formula	Explanation of Parameters
Exchange interaction	Effective within a minimal range, usually among neighbouring atoms	$W_{\text{ex}} = -J \sum_{i,j} \vec{S}_i \vec{S}_j$	J denotes the exchange integral, $\vec{S}_i$ and $\vec{S}_j$ are the spin vectors of the interacting electrons. The sign of J indicates whether the material shows ferromagnetic ($J > 0$) or antiferromagnetic ($J < 0$) behaviour.
Dzyaloshinskii-Moriya Interaction	Weaker than exchange interaction, acts at a short-range	$W_{\text{DMI}} = -\sum_{i,j} \vec{d}_{ij}(\vec{S}_i \times \vec{S}_j)$	$\vec{d}_{ij}$ is the Dzyaloshinskii vector, determining the interaction's direction and magnitude.
Zeeman interaction	Moderate strength, influenced by external magnetic fields, applicable to all magnetic moments exposed to the field	$W_{\text{H}} = -\vec{\mu}\vec{H}$	$\vec{\mu}$ is the atomic magnetic moments and $\vec{H}$ is the external magnetic field
Magnetic anisotropy	It is weaker than exchange and Zeeman interactions but crucial for maintaining magnetic orientation stability.	$W_{\text{Anis}} = = K_1 \text{Sin}^2[\theta] + K_2 \text{Sin}^4[\theta]$	K_1, K_2, are the anisotropy constants, and θ is the angle between spins and the easy axis
Dipolar Interaction	Generally weaker than exchange interactions, important for long-range magnetic order	$W_{\text{Dip}} = = -\frac{\mu_0}{4\pi} \frac{\vec{m}_1 \vec{m}_2 - 3(\vec{m}_1 \hat{\mathbf{r}})(\vec{m}_2 \hat{\mathbf{r}})}{\lvert\vec{r}\rvert^3}$	μ_0 is the vacuum magnetic permeability constant, $\vec{m}_1$ are $\vec{m}_2$ the magnetic moments of the dipoles, $\hat{r}$ is a unit vector parallel to the line joining the centers of the two dipoles, and $\lvert r \rvert$ is the distance between them

1.4. General classification of magnetic materials

According to the contemporary views, magnetic properties of materials are divided into diamagnetic, paramagnetic, ferromagnetic, antiferromagnetic and ferrimagnetic. Quantitatively, magnetic properties of materials are usually estimated by the value of magnetic susceptibility χ.

1.4.1. Diamagnetism

Diamagnets are substances whose atoms, ions, or molecules possess no permanent (intrinsic) magnetic dipole moment in the absence of an external field. When an external magnetic field B_{ext} is applied, circulating electron currents are induced (Lenz's law response). These currents generate an induced magnetic moment m_{ind} that points opposite to B_{ext}, giving a small negative magnetic susceptibility $\chi < 0$. In a non-uniform field, diamagnets are pushed toward the weaker-field region. In a uniform field, they feel no net force, but an elongated diamagnetic rod will orient perpendicular to the field lines (this minimises magnetic energy because its induced dipole is antiparallel to the field). Magnetic susceptibility in diamagnets is temperature-independent. It has to be pointed out that diamagnetism is inherent in all substances without exception: in solid, liquid and gaseous states, but it manifests itself weakly and is often suppressed by other effects.

1.4.2. Paramagnetism

Paramagnetic materials contain atoms, ions, or molecules with permanent magnetic moments (typically from one or more unpaired electron spins and, where not quenched, orbital angular momentum). Without an external field the bulk magnetisation is zero, because these moments are randomly oriented by thermal motion. Under an applied field, these intrinsic dipoles tend to align parallel to B_{ext}, producing a positive magnetic susceptibility $\chi > 0$. For non-interacting moments the susceptibility follows Curie's law, $\chi = \frac{C}{T}$; it increases as temperature decreases and saturates when most moments are aligned at very low T or high B_{ext}.

1.4.3. Ferromagnetism

Ferromagnets (FM) are substances in which the magnetic moments of atoms or ions are in a state of spontaneous magnetic ordering, and the resulting magnetic moments of each domain are nonzero. In an external magnetic field, all magnetic moments are oriented along the field direction (Fig.1.1(a)) i.e. parallel. As a result, a macroscopic magnetic moment arises, equal to the sum of the magnetic moments of

all atoms. In the absence of an external magnetic field, such a completely ordered state often becomes thermodynamically unfavourable and, as a result, breaks up into macroscopic regions (i.e. domains), within which the magnetic moments of the atom are parallel. In general, magnetic ordering results in the emergence of several magnetic sublattices, each of which combines ions with identical magnetic moments. However, the total magnetic moment of the sample is close to zero. In such materials transition to a ferromagnetic state occurs at a specific temperature known as the Curie point. FM`s exhibit very high magnetic susceptibility $\chi \gg 1$, which can vary significantly depending on the magnetic field strength and the proximity to the Curie temperature.

1.4.4. Antiferromagnetism

Antiferromagnets (AFM) are materials in which there is an orderly antiferromagnetic arrangement of magnetic moments of atoms or ions, yet no net magnetisation is present in the crystal. In the simplest case AFM structure can be depicted as two overlapping identical ferromagnetic crystalline sublattices with opposing magnetic moments $\vec{M}_1 = -\vec{M}_2$ (Fig.1.1(b)). A material typically becomes an antiferromagnet below a specific temperature, the Néel point, and maintains this state up to that temperature. The magnetic susceptibility of antiferromagnets is generally low and shows a peak near the Néel temperature due to the onset of magnetic ordering.

1.4.5. Weak ferromagnetism

Unlike "pure" AFMs, weak ferromagnets (or also called canted antiferromagnets) are characterised by a small noncollinearity (Fig.1.1(c)) of the sublattices caused by the specific relativistic Dzyaloshinskii-Moriya interaction. Since this interaction is significantly weaker than the exchange interaction, the resulting magnetic moment M is significantly smaller than the magnetisation of each of the sublattices. Examples of such structures are $\alpha - \mathrm{Fe_2O_3}, \mathrm{RFeO_3}, \mathrm{NiF_2}, \mathrm{MnCO_3}, \mathrm{CoCO_3}$ etc.

1.4.5. Ferrimagnetism

Ferrimagnetic materials feature atomic magnetic moments in different sublattices (Fig.1.1(d)) oriented antiparallel, similar to antiferromagnetic materials, but with unequal moments between the sublattices, resulting in a non-zero net magnetic moment: $\vec{M} = \sum \vec{M}_i$. In the simplest case, ferrimagnets have two collinear magnetic sublattices with different magnetic moments oriented antiparallel, so that:

$\vec{M} = \vec{M}_1 - \vec{M}_2 \neq 0$. However, in the case of three or more sublattices, collinear orientation is not needed at all. The best-known example of a ferrimagnet is yttrium iron garnet (YIG), which has 20 sublattices. Like ferromagnets, ferrimagnetics exhibit high magnetic susceptibility, but with more complex temperature dependence due to the different contributions from the different magnetic sublattices.

1.4.6. Magnetic frustration

A magnetically frustrated structure refers to a magnetic system in which the spins (magnetic moments) of atoms or ions cannot simultaneously satisfy all their magnetic interactions due to the geometry of the lattice or competing interactions. This "frustration" prevents the system from settling into a simple, ordered ground state, leading to complex or degenerate arrangements of spins. Frustration commonly arises in systems with antiferromagnetic interactions (like $Tb_3Ga_5O_{12}$), where neighbouring spins prefer to align antiparallel. For instance, in a triangular lattice (Fig.1.1(e))**,** if two spins align antiparallel, the third spin cannot satisfy its interaction with both neighbours simultaneously, resulting in frustration.

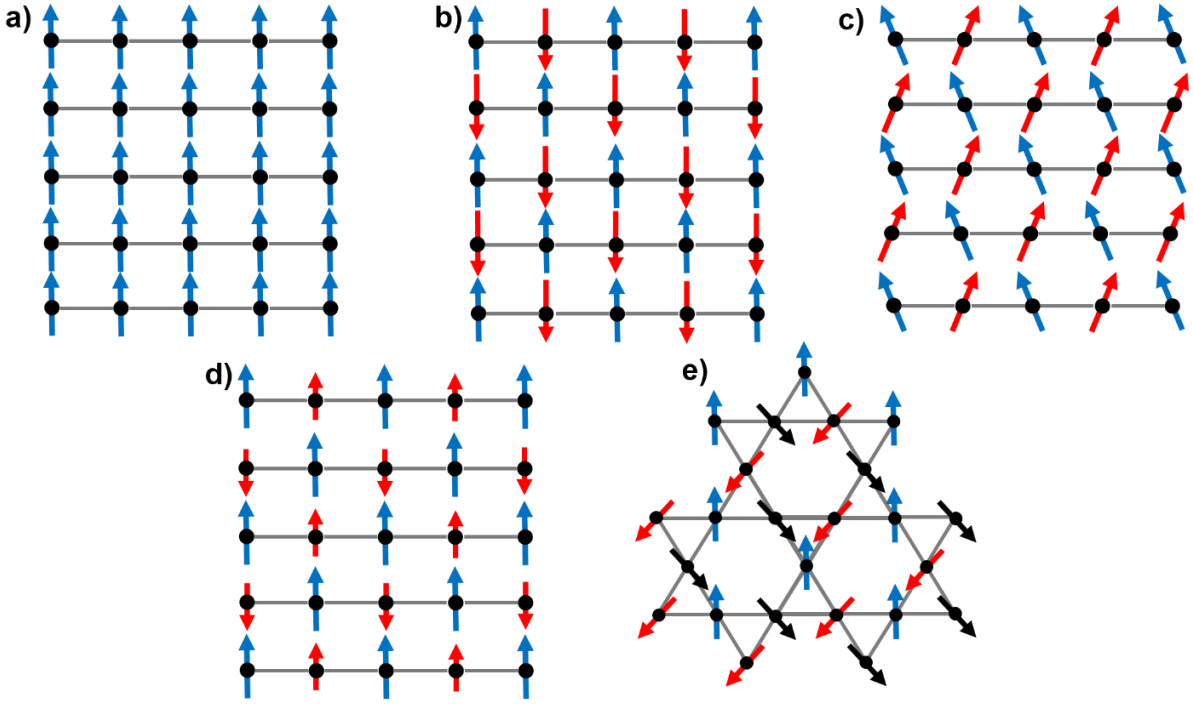

Fig.1.1. Schematic representation of different types of ordering on a two-dimensional lattice. Elements of one sublattice are highlighted in colour. (a): ferromagnet, (b) collinear antiferromagnetic structure of the Neel type with two equivalent sublattices (up-down), (c) weak ferromagnet, (d) collinear ferrimagnet, (e) frustrated magnetic structure (kagome lattice).

This phenomenon also occurs in other geometries, such as kagome lattices, pyrochlore structures, or spin ices, where multiple competing interactions contribute to frustration. Magnetic frustration leads to exotic phenomena like spin liquid states, where spins fluctuate even at very low temperatures, and spin glasses, where spins freeze into a disordered state.

1.5. Landau theory of phase transitions

Landau theory, developed by Lev Landau, provides a foundational framework for understanding phase transitions in materials, in particular those undergoing magnetic phase transitions [79–81]. This theory uses a phenomenological approach, focusing on the concept of symmetry breaking and the role of the order parameter, a measurable quantity that represents the degree of order within different phases of a material. The order parameter changes characteristically through a phase transition, distinguishing different states of matter (e.g., solid, liquid, gas) or magnetic states (e.g., ferromagnetic-paramagnetic).

1.5.1. Thermodynamic Potential and Phase Transitions

Landau's phenomenological theory posits that near a phase transition, the **thermodynamic potential** can be expanded as a power-series (Taylor expansion) in terms of an **order parameter** that characterises the emerging order. The order parameter η (magnetisation M, polarisation P, distortion, etc.) which generally depends on temperature and some other external parameters like pressure, magnetic field, etc., is chosen such that it is zero in the high-symmetry (disordered) phase and nonzero in the symmetry-broken phase, capturing the essence of the phase transition [80–82].

Near the transition point, Φ can be expanded as a power series of η:

$$\Phi = \Phi_0 + \alpha\eta + A\eta^2 + C\eta^3 + B\eta^4 + \cdots. \quad (1.1)$$

Here, Φ_0 is the regular part of the free energy that does not depend on the order parameter, and $A, B,$ and C are parameter-dependent (i.e. temperature) coefficients. The form of the expansion depends on the symmetry of the order parameter and the nature of the phase transition, which could be 1st or 2nd order. For example, if a symmetry operation of the high-temperature phase changes the sign of the order parameter, then the free energy must be an even function of that order parameter (i.e. invariant under that operation): in a ferromagnet with no external field, the Hamiltonian is invariant under **time reversal symmetry** (which flips all spins, $\vec{M} \rightarrow$

$-\vec{M}$). Therefore, the free energy in the paramagnetic phase must satisfy $\Phi(\vec{M}) = \Phi(-\vec{M})$, implying that it can only contain even powers of $\vec{M}$. Conversely, if the high-temperature phase **does not** have a symmetry that enforces $\eta \to -\eta$ equivalence, then odd-order terms are allowed in the free energy. A classic case is the liquid–gas transition: one can define an order parameter η proportional to the difference in density between liquid and gas. In general, Landau's theory states that **all terms allowed by symmetry should be included** (at least up to the lowest order that produces the observed behaviour). If an external field is applied that breaks the symmetry (e.g. a magnetic field $\vec{H}$ breaks time-reversal, or an electric field breaks inversion symmetry), then linear terms appear in Φ, changing the double-well potential landscape.

Fig 1.2. (a-b) illustrates the change of the thermodynamic potential landscape as a function of order parameter η, and (c-d) shows the change in the order parameter $\eta(T)$ across the 1st and 2nd order phase transitions.

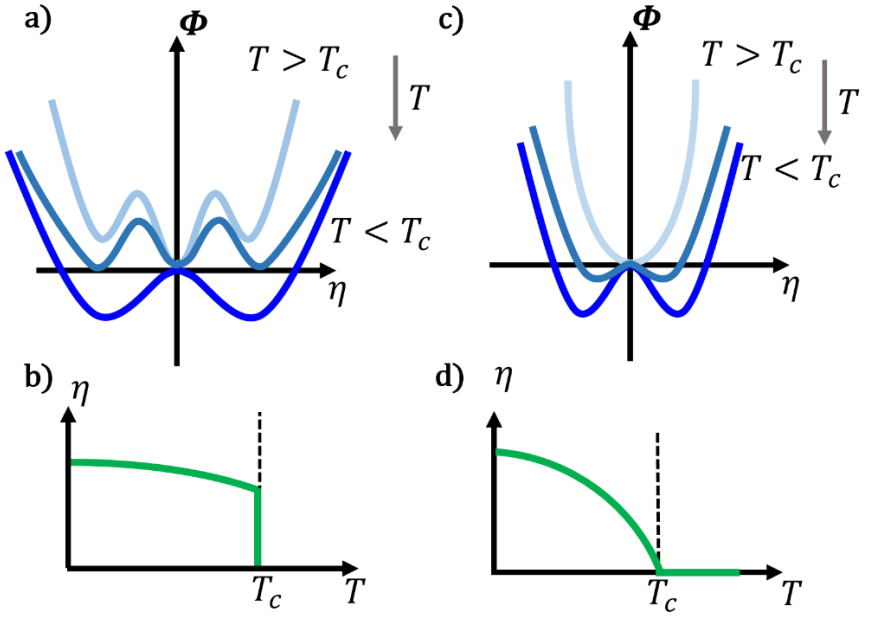

Fig.1.2. (a) Illustration of the alteration in the shape of thermodynamic potential with the change in temperature having only stable and metastable states; (b) shows the behaviour of the order parameter η curve as a function of temperature having a jump-like behaviour across a 1st order phase transition. (c) Illustration of the continuous change in the shape of thermodynamic potential via a set of stable states and (d) the smooth changes in the order parameter η curve across a 2nd order phase transition.

1st - order transitions: characterised by an abrupt jump of the order parameter with the change of temperature (see Fig.1b). 1st-order transitions in the Landau framework occur when the free energy curve as a function of the order parameter exhibits two distinct minima (see Fig.1a). These minima correspond to different thermodynamic phases – stable and metastable, which are separated by an energy barrier. In terms of the coefficients, cubic terms should be included; a negative *B* in the expansion can lead to a situation where the free energy curve has a bimodal form.

2nd - order transitions: in second-order transitions, the change of the free energy curve as a function of the order parameter is continuous (Fig.1c). They are characterised by vanishing cubic terms (C = 0). The further requirement that $\eta = 0$ above T_c, but $\eta \neq 0$ for $T < T_c$ (Fig.1d), leads to the requirement that the first nonzero term $A\eta^2$ in the expansion for Φ should obey the conditions: $A > 0$ for $T > T_c$ and $A < 0$ for $T < T_c$.

1.5.2. Antiferromagnets: the case of rare-earth orthoferrites

Landau theory could be extended to describe the features of the magnetic phase transitions occurring in antiferromagnets. In a theoretical description of antiferromagnets it is convenient to use two sublattice approximation ($\vec{M}_1$ and $\vec{M}_2$). In this regard, it is convenient to choose a Néel vector $\vec{G}$ as an order parameter which could be represented as normalised difference between two sublattices $\vec{G} = \frac{\vec{M}_1 - \vec{M}_2}{2M_0}$ (which is nonzero in the ordered phase, aligns oppositely on the two sublattices), often together with the net magnetisation vector $\vec{F} = \frac{\vec{M}_1 - \vec{M}_2}{2M_0}$, where M_0 is the value of magnetic moment at $T = 0$.

In Landau theory one can treat the set of sublattice magnetisations as a "state vector" $\vec{M}$ entering the free energy expansion Φ. The free energy is then expanded in components of $\vec{M}$, including all symmetries of the paramagnetic phase (like time-reversal, lattice point-group symmetry, etc.) [83]. For a collinear antiferromagnet in zero field, the free energy will even be a function of $\left|\vec{G}\right|^2$ (and higher even powers) because if all spins are flipped ($\vec{G} \to -\vec{G}$, which is equivalent to a 180° rotation or time reversal followed by sublattice exchange), the energy is unchanged. Thus, only even terms like $\left|\vec{G}\right|^2$, $\left|\vec{G}\right|^4$, etc., appear for a simple antiferromagnetic order parameter, analogous to the ferromagnetic case.

Rare-earth orthoferrites. $RFeO_3$ (where R represents a rare-earth ion or yttrium), crystallise in the distorted perovskite structure (P_{bnm}). They provide an important example of Landau theory applied to **antiferromagnetic systems with complex magnetic order**. These orthoferrites are predominantly antiferromagnetic in the Fe^{3+} sublattice (order sets in around 620–750 K for different R) with a slight canting of spins that produces a weak ferromagnetic moment (due to the Dzyaloshinskii–Moriya interaction). They exhibit spin-reorientation phase transitions at lower temperatures (typically in the range 50–100 K, depending on R) where the orientation of the Fe spins (and thus the weak ferromagnetic moment) rotates from one crystallographic axis to another as temperature changes. This is a change in the direction of the order parameter vector, driven by competing magnetic anisotropy terms and coupling between the Fe and R sublattices.

To describe correctly behaviour of iron spin during SRPT in frames of Landau theory it is convenient to introduce the angular order parameter in the following form $\vec{G} = (G_x, G_y, G_z)$ as $G_x = \sin[\theta], G_y = 0, G_z = \cos[\theta]$.

For the case of orthoferrites, the simple[1] form of the thermodynamic potential in the presence of an external magnetic field can be written as:

$$\Phi = \frac{1}{2} A\vec{F}^2 + d\left[\vec{F} \times \vec{G}\right] - \vec{F}\vec{H} + \Phi_A. \qquad (1.2)$$

Here, A is the exchange interaction constant, d is the antisymmetric exchange parameter (or Dzyaloshinskii-Moriya constant), $\vec{H}$ is the external magnetic field and Φ_A is anisotropy part determined by the magnetic symmetry group of the AFM under the study.

In this thesis, we will focus on analysing the features of the second-order spin-reorientation phase transition (SRPT) of iron spins in Thulium and Terbium orthoferrites, (Chapters 3 and 4). In orthoferrites, the 2nd order SRPT occurs in the *xz* (ac)[2] plane of a crystal. Now let`s focus on the anisotropy part of Φ_A the thermodynamic potential.

For magnetic crystals with orthorhombic symmetry, one could write the anisotropy part of the free energy expansion in terms of $\sin[\theta]$ or $\cos[\theta]$,

[1] This form of Φ does not take into account terms including exchange interaction with R-subsystems and others, we will extend it in Chapters III and IV providing more accurate and complete description

[2] In $RFeO_3$ the Cartesian coordinates (x-y-z) correspond to the a,b,c, crystallographic axes

corresponding to invariants of the rotation symmetry [83] up to fourth order [84] in the following form:

$$\Phi_A = K_1 \sin[\theta]^2 + K_2 \sin[\theta]^4, \tag{1.3}$$

Here, K_1 is also often denoted as K_{ac} (corresponding to an anisotropy occurring in *ac* plane), and K_2 are anisotropy coefficients that vary with temperature and contribute to the SRPT. In a simple case, K_1 is the first anisotropy constant that distinguishes two easy axes (say $\theta = 0°$, meaning that $\vec{G}$ is pointed along *a*(*x*) axis) or $\theta = 0°$, $\vec{G}$ is pointed along *c*(*z*) axis), and K_2 is a higher-order anisotropy that may prefer the spins to stay aligned along axes versus in between. The temperature dependence of these constants (often coming from the rare-earth sublattice or spin–orbit effects) governs the reorientation (in Chapter III we consider this in more detail). If K_1 changes sign as T passes through some region (meaning the preferred easy axis switches), the spins will reorient. Whether this reorientation is continuous (2nd order) or abrupt (1st order), depends on the relative value and sign of K_2 [83,84]. Empirically, rare-earth orthoferrites show both types of behaviour.

1) If $K_2 > 0$, the free energy as a function of θ, $\Phi(\theta)$, may have a single minimum that smoothly moves from one angle to another as T changes. In this case, the spin orientation changes **gradually** — this can be viewed as two consecutive second-order transitions at the endpoints of the rotation. One where spins start to tilt away from the original easy axis, and another where they lock into the new easy axis (like in $TmFeO_3$, $ErFeO_3$, $TbFeO_3$, $YbFeO_3$ etc.).

In this case, the SRPT consists of three phases during which a 90° reorientation of iron spins occurs, namely Γ_4-(*high-T*), Γ_{24}-(*intermediate*), Γ_2-(*low-T*), (see Fig.1.3).

$$\begin{cases} \Gamma_4 : \sin(\theta) = 0; \quad K_{\mathrm{ac}} \geq 0, \qquad T \geq T_1, \\ \Gamma_{24} : \sin(\theta) = \sqrt{-\dfrac{K_{\mathrm{ac}}}{2K2}}; \; K_{\mathrm{ac}} \leq 0, K_{\mathrm{ac}} + 2K_2 \leq 0, \qquad T_2 \leq T \leq T_1, \\ \Gamma_2 : \sin(\theta) = 1; \; K_{\mathrm{ac}} + 2K_2 \geq 0, \qquad T \leq T_2. \end{cases} \tag{1.4}$$

The temperatures T_1 and T_2, where $K_{\mathrm{ac}}(T) = 0$ and $K_{\mathrm{ac}}(T) + 2K_2 = 0$, are the transition points between phases $\Gamma_4 - \Gamma_{42}$, and $\Gamma_{24} - \Gamma_2$, respectively.

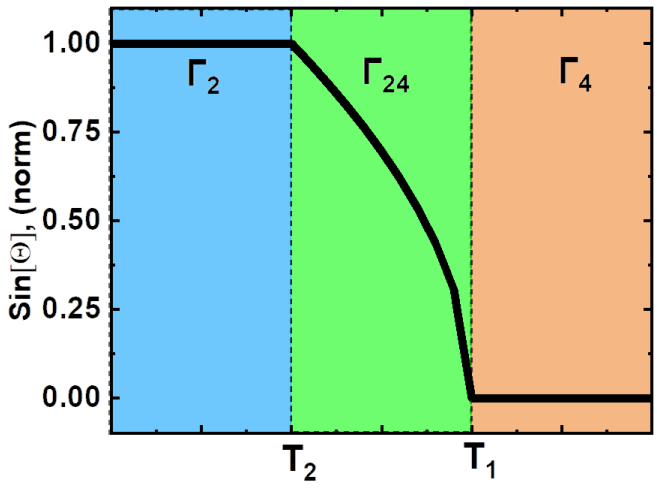

Fig. 1.3. Illustration of 2nd order SRPT in $Tm/TbFeO_3$

2) If $K_2 < 0$, or a large positive higher-order term creates a secondary minimum in Φ, the system can get a bistable potential. Then as K_1 approaches zero, the system might prefer to jump from one easy axis orientation to the other, because an intermediate tilted state is **unstable** (there is an energy barrier between orientations). In Landau terms, this means one needs to expand to higher orders and to find a term analogous to a negative quartic in $\sin[\theta]^2$ that yields a first-order transition (the angle θ jumps discontinuously at the transition temperature). In orthoferrites (like in $HoFeO_3$), such a jump is marked by a sudden spin flip at a certain temperature.

To summarize, the Landau theory offers a versatile and powerful method to describe and analyse phase transitions, providing insights into the behaviour of various magnetic materials under changing external conditions. By using this theoretical approach for the investigation of SRPT of the second order in Chapter 3 and Chapter 4 in rare-earth orthoferrites, we will extend the anisotropy part of thermodynamic potential, accounting for all relevant interactions between Fe and Tm/Tb subsystems in $TmFeO_3/TbFeO_3$.

1.6. Description of nonlinear dynamics in antiferromagnets

The exploration of magnetisation dynamics began with the development of the Landau-Lifshitz-Gilbert (LLG) equation in the mid-20th century. This equation, first introduced by Lev Landau and Evgeny Lifshitz, published back in 1935 [46], reprinted [47], and later modified by T. L. Gilbert, describes the precessional motion of magnetisation in ferromagnetic materials due to magnetic fields and damping:

$$\frac{d\vec{M}}{dt} = -\gamma \vec{M} \times \vec{H}_M + \vec{R}_M, \tag{1.5}$$

Here, $\vec{H}_M = -\frac{\partial \Phi}{\partial \vec{M}}$ represents the effective field exerted on the magnetic moments within the sample, Φ-is the TP function of ferromagnet, reflecting their interactions (it also includes the external field $\vec{H}_{\text{ext}}$). The relaxation term is defined as follows:

$$\vec{R}_M = \frac{\gamma\lambda}{|\vec{M}|}\vec{M} \times \left(\vec{M} \times \vec{H}_F\right) \cong \frac{\lambda}{|\vec{M}|}\left(\vec{M} \times \frac{d\vec{M}}{dt}\right), \tag{1.6}$$

Despite the presence of a dissipative term of the type (1.6), equation (1.5) possesses the integral of motion ($\Phi^2 = \text{const}$). By multiplying it by the scalar $\vec{M}$, we derive, that $\vec{M} \cdot \frac{d\vec{M}}{dt} = 0$, or equivalently $\frac{d}{dt}M^2 = 0$. The motion represents the precession of $\vec{M}$ around $\vec{H}_M$ with a gradual decrease in the transverse component F to zero at equilibrium.

In the context of a two-sublattice model of antiferromagnets (like orthoferrites) characterised by magnetisations $\vec{M}_1$ and $\vec{M}_2$, we can write an equation analogous to (1.1) for each sublattice. If we then transition to the resultant equations in terms of dimensionless vectors $\vec{F} = \frac{\vec{M}_1 + \vec{M}_2}{2}$ and $\vec{G} = \frac{\vec{M}_1 - \vec{M}_2}{2}$, we obtain:

$$\begin{cases} \dfrac{d\vec{F}}{dt} = -\gamma\left(\vec{F} \times \vec{H}_F + \vec{G} \times \vec{H}_G\right) + \vec{R}_F, \\ \dfrac{d\vec{G}}{dt} = -\gamma\left(\vec{F} \times \vec{H}_G + \vec{G} \times \vec{H}_F\right) + \vec{R}_G. \end{cases} \tag{1.7}$$

If we designate the dissipative terms as $\vec{R}_F$=$\vec{R}_G = 0$, then from (1.3) we obtain the conditions:

$$\vec{F}^2 + \vec{G}^2 = 4M_0^2, \qquad \vec{F}\vec{G} = 0. \tag{1.8}$$

Those are characteristic for the two-sublattice model of an antiferromagnet. Here, $\vec{H}_F = -\frac{\partial \Phi}{\partial \vec{F}}$ and $\vec{H}_G = -\frac{\partial \Phi}{\partial \vec{G}}$ are the corresponding effective fields and Φ is the TP function in the form from (1.2).

By solving system (1.7) in case of linear approximation (i.e. small deviations from equilibrium) one could derive two antiferromagnetic resonance (AFMR) frequency modes namely:

$$\omega_1 = \gamma\sqrt{H_{A1}H_{ex}},\ \ \omega_2 = \gamma\sqrt{H_{A2}H_{ex}}. \tag{1.9}$$

Here, ω_1, ω_2 are the AMFR frequencies, and $H_{A1} = K_1F_0, H_{A2} = K_2F_0$ denote anisotropy fields and $H_{\text{ex}} = \frac{1}{2}AF_0$ is the exchange field.

1.7. Magneto-optical effects

Magneto-optical effects, emerging at the intersection of magnetism and optics, showcase the profound influence of magnetic order on the behaviour of light. These phenomena are not only intriguing from a scientific standpoint but also have substantial technological implications. The primary effects discussed here include the Faraday effect, the Cotton-Mouton effect, and the magneto-optical Kerr effect (MOKE), each of which provides insights into the interaction between light and magnetised materials [85],[32].

1.7.1. Faraday Effect

The Faraday effect is a fundamental magneto-optical phenomenon observed in transmission geometry. It occurs when linearly polarised light passes through a magnetically active medium, causing the polarisation plane to rotate (Faraday rotation), see Fig. 1.4.

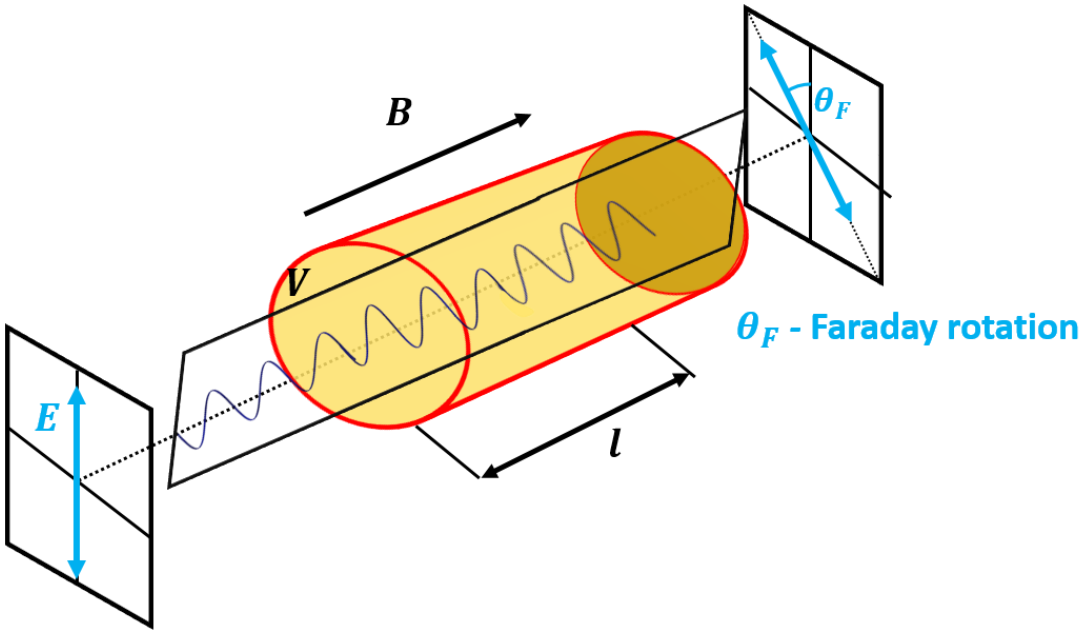

Fig.1.4. Illustration showing the manifestation of Faraday effect as the change of polarisation rotation passing through the magneto-optical medium.

The following equation describes the angle of rotation:

$$\theta_F = V \cdot B \cdot l. \tag{1.10}$$

Here, θ_F is the angle of rotation, V is the Verdet constant, B is the magnetic field strength, and l is the path length through the medium. This effect is a manifestation of the Zeeman effect, wherein a magnetic field causes a split in electronic energy levels, resulting in different refractive indices for right-handed and left-handed circularly polarised light components. As a result, the plane of polarisation for linearly polarised light traversing the medium alters accordingly. Therefore, the Faraday effect is also referred to as **magnetic circular birefringence (MCD)**.

The plane of polarisation of the linearly polarised light passing through the medium could be also expressed as:

$$\theta = \frac{\omega}{2c}(n_+ - n_-)L. \tag{1.11}$$

Here, ω is the angular frequency of light, c is the speed of light in vacuum, n_+ and n_- are the refractive indices for the circular polarisations, and L is the path length through the material.

1.7.2. Cotton-Mouton (Voigt) Effect

The Cotton-Mouton, also known as the Voigt effect, involves a magnetic field applied perpendicular to the light's path, leading to a different refractive index for polarisations parallel and perpendicular to the field and could be expressed as:

$$\Delta n = CB^2 d. \tag{1.12}$$

Here, Δn is the change in refractive index, C is the Cotton-Mouton constant, λ is the wavelength of incident light, and d is the material thickness.

The Cotton-Mouton or Voigt effect is also referred to as **magnetic linear birefringence (MLB)**. This linear birefringence is due to the alignment of anisotropic molecules, which alters the optical path differently for different polarisations (see Fig 1.5).

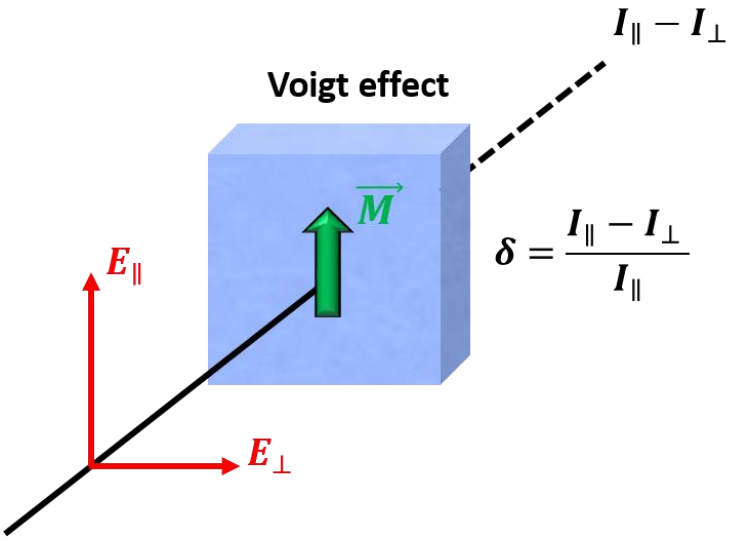

Fig.1.5. Illustration showing the Cotton-Mouton (Voigt) effect.

The relative change in intensity of the reflected light δ, upon re-magnetisation of the medium, used to identify the p-polarisation of the incident light. This effect, quadratic in magnetisation ($\sim M^2$) and proportional to $I_{\parallel} - I_{\perp}$, could be described by the following equation:

$$\delta = \frac{I_{\parallel} - I_{\perp}}{I_{\parallel}}. \tag{1.13}$$

Here, $I_{\perp(\parallel)}$ represents the intensity of light that is reflected or transmitted when the magnetisation is perpendicular (parallel) to the light's polarisation.

1.7.3. Magneto-optical Kerr Effect

The Kerr effect, also known as the quadratic electro-optic (QEO) effect, involves a change in the refractive index of a substance due to the application of an electric field. This effect is similar to the Faraday and Cotton-Mouton effects but is distinguished by its specific induction of polarisation rotation in light reflected from a magnetic surface. There are three distinct variants of the Magneto-optical Kerr effect—polar (PMOKE), longitudinal (LMOKE), and transverse (TMOKE)—are classified by the orientation of magnetisation relative to the sample plane and the angle of light incidence relative to the material's magnetisation, as illustrated in Fig. 1.6. In PMOKE and LMOKE, the polarisation of the reflected light turns elliptical, whereas in TMOKE, the polarisation remains unchanged; only its intensity varies.

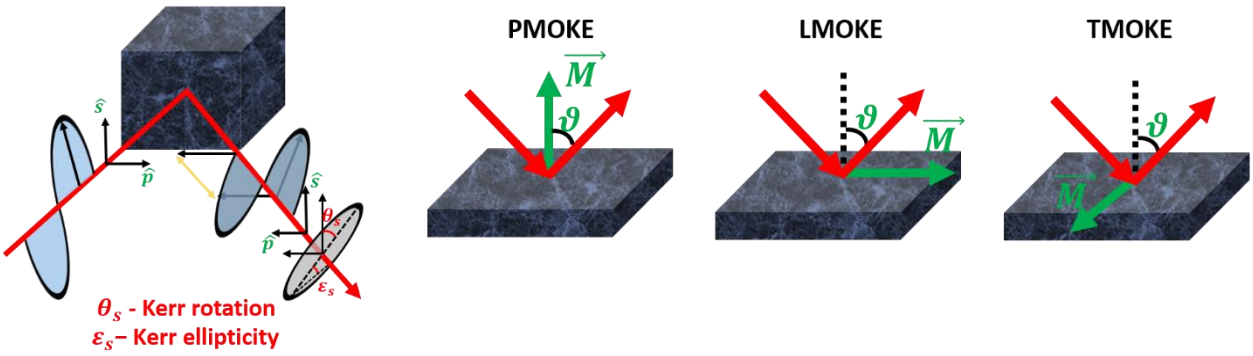

Fig.1.6. Kerr effect and its three configurations (PMOKE, LMOKE, and TMOKE).

1.7.4. Comparison and detection geometries

Each of these effects manifests distinctively depending on the material properties, light wavelength, magnetic field's strength and orientation.

1. **Faraday Effect**: Detected in transmission geometry with the magnetic field aligned parallel to the light's path, commonly used in devices such as optical isolators.
2. **Cotton-Mouton Effect**: Observed in transmission geometry but with the magnetic field applied perpendicularly, crucial for studying magnetic properties of liquids and gases.
3. **Kerr Effect**: Observed in reflection geometry, making it important tool for investigating surface and thin-film magnetism, pivotal in magneto-optical data storage technologies.

1.7.5. Application of magneto-optical effects in time-resolved studies

Magneto-optical effects are integral to time-resolved studies, especially in the areas of ultrafast magnetisation dynamics and spintronics. These effects facilitate the observation and manipulation of magnetisation on extremely short timescales, shedding light on the fundamental mechanisms at play within magnetic materials.

Here are several examples of such applications:

Ultrafast Magnetisation Dynamics

The Time-Resolved Magneto-Optical Kerr Effect (TRMOKE) is employed to investigate laser-induced magnetisation dynamics in metallic amorphous ribbons. This method exposes damped oscillations of the magnetisation vector, affected by

laser pulse fluence and external magnetic fields, pivotal for understanding the magnetoimpedance effect in the gigahertz frequency range. Such insights are invaluable for the development of broadband sensor devices [33].

Imaging of Magnetoelastic Waves. The Cotton-Mouton effect is applied in time-resolved magneto-optical imaging to visualize magnetoelastic waves. This method enables the direct observation of magnetisation dynamics, including excitation, propagation, and relaxation, in out-of-plane-magnetised films. Such imaging techniques broaden the scope of TRMO studies and provide crucial insights into laser-induced magnetisation dynamics relevant to spintronics [88].

Terahertz Radiation and Nonlinear Effects. Ultrafast light-driven magneto-optical nonlinearity in ferromagnetic heterostructures is explored using terahertz (THz) emission spectroscopy. This approach examines the picosecond-time-scale nonlinear magneto-optical effects, essential for understanding the roles of magnetisation-induced optical rectification and spin-to-charge current conversion in THz generation [89].

Chapter II. Experimental methods

In this chapter, we present an overview of the experimental techniques employed in the subsequent investigation as detailed within this thesis. First, we will elucidate the fundamental principles necessary for the understanding of the pump-probe spectroscopy technique. Then we will provide a detailed description of the experimental setup utilized for the detection Jahn-Teller like magnetic phase transition in $TbFeO_3$ (Chapter 4) and to investigate features of THz and optically driven spin dynamics in $Tb_3Ga_5O_{12}$ (Chapter 5).

2.1. Introduction

The terahertz (THz) frequency domain constitutes a region of the electromagnetic spectrum located between the microwave and infrared ranges. This domain is commonly referred to as the "THz gap" owing to the historical challenges associated with the generation and detection of THz waves. The THz frequency domain is typically delineated as encompassing frequencies from 0.1 THz to 10 THz. In a physical context, 1 THz corresponds to a wavelength of 300 microns in vacuum, to 33.3 cm^{-1} when expressed in wave numbers, to a photon energy of 4 meV, or to a temperature of 48 K (See Fig.2.1).

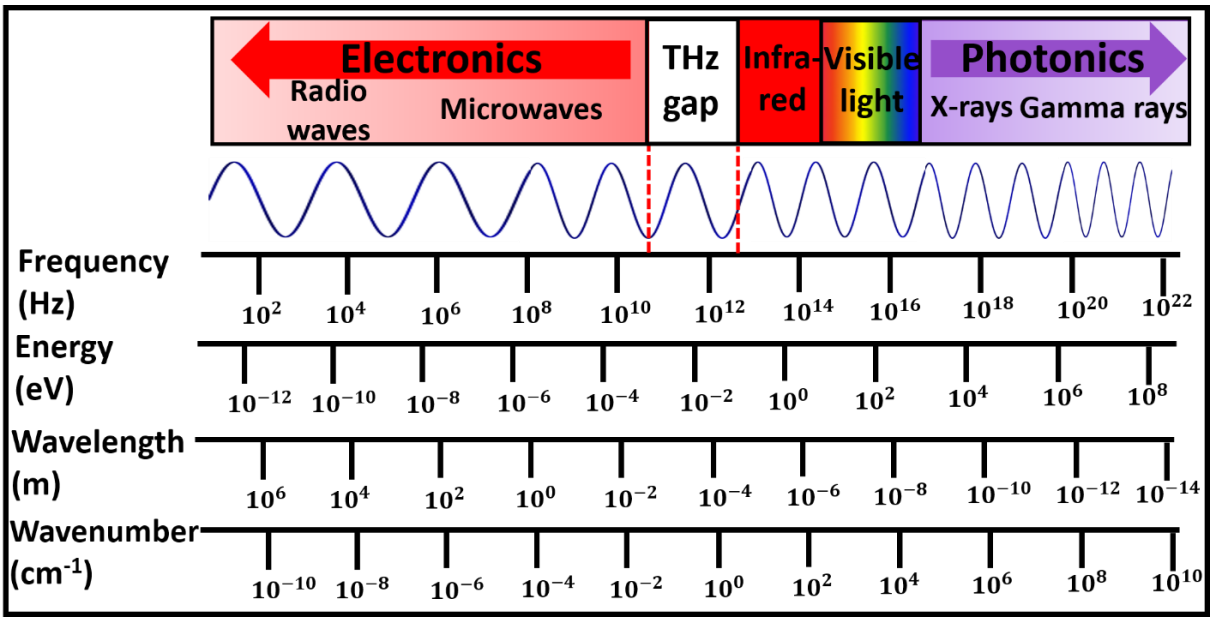

Fig. 2.1. Electromagnetic radiation spectrum illustrating the THz gap.

THz waves exhibit the property to penetrate non-destructively a variety of materials, including non-metallic substances (such as papers and plastics), organic materials, gases, and liquids, thereby establishing themselves as a powerful tool for spectroscopic sensing. The distinctive characteristics of THz radiation, particularly its capacity to interact with fundamental excitations (like phonons, magnons, excitons etc.) present in materials, render it an effective tool for investigating and manipulating their properties. This frequency domain proved itself very effective for the examination of ultrafast magnetisation dynamics and nonlinear phenomena, which are essential for the progression of both fundamental studies in condensed matter physics and practical technological applications [90,91]. The diverse applications of THz technology encompass a multitude of fields, including but not limited to material characterisation, which involves detailed analysis of material properties, biological imaging that enhances our understanding of biological systems, security scanning for safety measures, and wireless communications that promise faster and more efficient data transfer [92].

2.2. Pump-probe spectroscopy

Pump-probe spectroscopy is a powerful technique which is used to study non-equilibrium dynamical phenomena in different systems. This includes exploring magnetisation dynamics in magnetic materials, carrier dynamics in semiconductors, as well as cooper pairs and vortex dynamics in superconductors. The method employs a laser that emits ultrashort optical pulses, divided into two components by a beam splitter: pump and probe; delay control stage; detection bridge (Wollaston prism and photodetectors), see Fig 2.2:

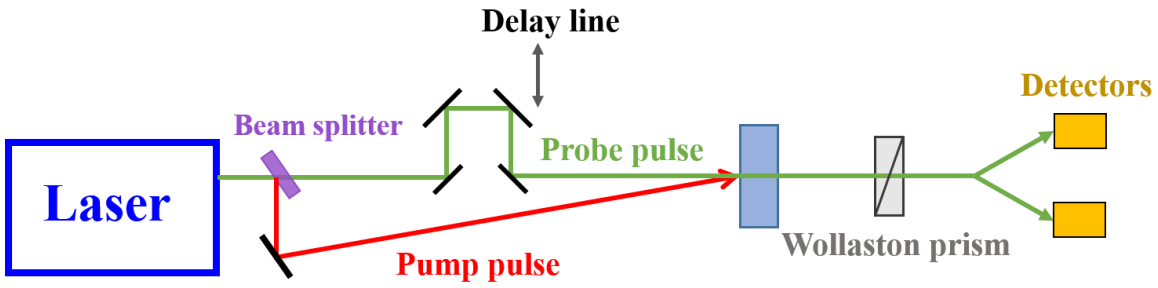

Fig. 2.2. A simplified representation of the standard pump-probe spectroscopy scheme.

Pump Pulse: This stronger pulse excites the sample, triggering dynamical processes like a spin precession, which alters the sample's magnetic properties.

Probe Pulse: Following the pump pulse, this weaker, delayed pulse measures the changes in the sample caused by the pump, providing information about these changes.

It has to be pointed out that depending on the research task pump and/or probe can be tuned to various spectral ranges, including far-infrared, optical, ultraviolet, or X-ray, each sensitive to specific electronic transitions. This tuning enables precise measurements of phenomena like polarisation rotation due to the Faraday or Kerr effects.

2.2.1. Temporal and spectral resolution

Temporal Control: By adjusting the delay time Δt between the pump and probe pulses $\Delta t = 2\Delta x/c$, where Δx is the path difference introduced by the delay line and c is the speed of light, femtosecond resolution can be achieved. This control is crucial for capturing transient processes within the material.

Spectral Sensitivity: Selecting the probe pulse's wavelength is important part as it determines the targeted electronic transition. Different wavelengths allow for the observation of various aspects of the phenomenon, providing a comprehensive understanding of the dynamic processes.

2.2.2. Experimental geometry

The typical pump-probe setup, as illustrated in Figure 2.3, includes a laser source, beam-splitter (BS) that divides the laser pulses into pump and probe beam lines. The probe beam is separated by a BS and delayed via delay stage with respect to the pump pulse. The detection component of the setup, known as polarisation bridge, consists of a Wollaston prism (WP) which splits the probe pulse into two orthogonal polarisation components. These components are captured by two balanced photodetectors (PDs) that measure the intensity and polarisation changes in the probe pulse, converting them in photocurrent. The differences in signals from these orthogonal components provide insights into polarisation rotation changes, which are detected using a lock-in amplifier. It is important to note that, before starting pump-probe measurements, photodetectors must be balanced by adjusting the half waveplate angle in the absence of a pump pulse to ensure zero voltage. This procedure is known as “balance detection scheme”. Once it is done the setup enables accurate, time-resolved measurements of subtle changes in the dynamical properties of the sample’s, like magnetisation.

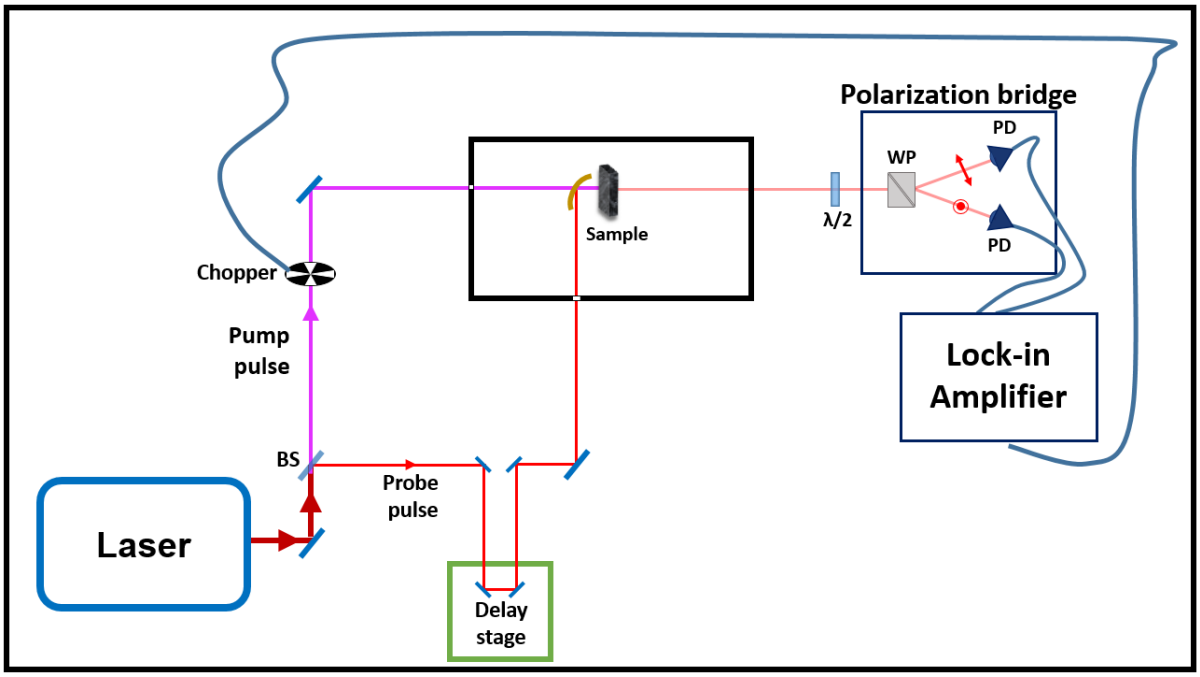

Fig.2.3. Illustration of a general pump probe scheme. Details of the setup are in the main text.

2.2.3. Practical applications and modifications

- **Magneto-Optical Effects**: Our measurements focus primarily on magnetic dynamics, that in optical measurements results in the changes of polarisation state (rotation or ellipticity) in transmission (Faraday) or reflection (Kerr) geometry. Therefore, through this thesis the Faraday effect in orthoferrites and TGG crystal will be studied. However, such experimental setup could be adjusted for measuring in reflection geometry as well.
- **Modifications**: This experimental setup can be further modified by introducing a nonlinear crystal, like $LiNbO_3$ to generate THz pump pulses to perform THz pump optical probe spectroscopy measurements (Chapter 4) or by adding a Beta Barium Borate crystal for converting an 800 nm optical pump into a 400 nm pump (Chapter 5), which adds flexibility to the pump-probe technique.

2.2.4. Lock-in-amplifier detection technique

Lock-in amplifiers play a critical role across various scientific and engineering fields, including quantum mechanics, optical research, and biomedical engineering. These sensitive devices are crucial in detecting and analysing the slightest variations in electrical signals, making them indispensable for identifying weak alternating current (AC) signals obscured by noise. Their ability to precisely extract and amplify

signals at a specific reference frequency greatly reduces the interference from extraneous noise, thus enhancing the clarity and reliability of the measurements.

Operational Principle. Lock-in amplifier primary function is **phase-sensitive detection (PSD)** – it amplifies only the components of the input signal at a given reference frequency and phase, decreasing the signal at other frequencies [93]. This is achieved by an internal architecture equivalent to a homodyne (synchronous) detector followed by a tuneable low-pass filter. In practical terms, if an experiment can imprint a unique modulation frequency on the signal of interest, a lock-in amplifier can **"lock in"** to that frequency and recover signals **orders of magnitude weaker** than the broadband noise (in some cases, signals 10^6 times smaller than the noise). This makes lock-in amplifiers indispensable in optical and electrical measurements where signal-to-noise ratios (SNR) are very low.

For our experiments, we chose a reference frequency of 500 Hz, modulated by an optical chopper operating at half of the laser frequency repetition rate (see Fig.2.3). The lock-in amplifies the input signal V_{in} and then multiplies it by reference V_{ref} using a phase-sensitive detector or multiplier. The output of the PSD could be represented simply as the product of two sine waves:

$$V_{\mathrm{out}} = V_{\mathrm{in}}V_{\mathrm{ref}} = V_{\mathrm{sig}}V_{\mathrm{L}}\sin\left(\omega_{\mathrm{L}}t + \theta_{\mathrm{sig}}\right)\sin(\omega_{\mathrm{ref}}t + \theta_{\mathrm{ref}}). \qquad (2.1)$$

Here, V_{sig} and V_{L} are signal and internal reference signal amplitudes; ω_{L} internal reference frequency; and θ_{sig} and θ_{ref} signal and reference signal phases.

This formula could be simplified using trigonometric identities to reveal a more manageable one that illustrates the interaction between the signals:

$$V_{\mathrm{out}} = \frac{1}{2}V_{\mathrm{sig}}V_{\mathrm{L}}\left[\cos((\omega_{\mathrm{r}} - \omega_{\mathrm{L}})\,t + \theta_{\mathrm{sig}} - \theta_{\mathrm{ref}}\right) + \cos((\omega_{\mathrm{r}} - \omega_{\mathrm{L}})\,t + \theta_{\mathrm{sig}} + \theta_{\mathrm{ref}})]. \qquad (2.2)$$

Here, ω_{r} is the frequency of the square wave used for sync with output function.

By filtering out high-frequency components (the sum frequency), the lock-in amplifier focuses on the difference frequency, which ideally is zero (DC component), when $\omega_{\mathrm{r}} = \omega_{\mathrm{L}}$ and $\theta_{\mathrm{sig}} = \theta_{\mathrm{ref}}$. The output from the phase-sensitive detector (PSD) is then:

$$V_{\mathrm{PSD}} = \frac{1}{2} V_{\mathrm{sig}} V_{\mathrm{L}} [\cos(\theta_{\mathrm{sig}} - \theta_{\mathrm{ref}})]. \quad (2.3)$$

The output from the PSD is straightforward, highlighting key signal characteristics and is proportional to the cosine of the phase difference. This value indicates how well the incoming signal aligns in-phase with the reference. To maximize signal amplitude, precise calibration of the phase shift between the reference and the input signal is essential, as minor discrepancies can significantly impact results.

To summarise, lock-in amplifiers significantly improve the signal-to-noise ratio by focusing on the signal portion in sync with the reference frequency. The remarkable specificity achieved by the narrow bandwidth of the low-pass filter applied after the PSD selectively amplifies frequencies close to the reference frequency. The narrow bandwidth ensures that only frequencies near the reference frequency contribute to the output, significantly reducing noise.

2.3. THz Generation: Techniques and mechanism

Terahertz time-domain spectroscopy (THz-TDS) relies on ultrafast THz pulses to probe low-energy excitations in materials. Generating these broadband, sub-picosecond THz pulses is challenging due to the so-called "THz gap" between electronic and optical frequencies. A variety of techniques have been established, utilizing nonlinear optics, ultrafast laser interactions, and plasmonic enhancements to generate high-quality THz radiation. This section outlines the methods employed in our experiments, specifically **optical rectification** and **phase matching condition**.

2.3.1. Optical Rectification

Optical rectification (OR) is a nonlinear optical process that allows to generate terahertz (THz) waves efficiently by leveraging the second-order nonlinear susceptibility $\chi^{(2)}$. In this process, an ultrafast infrared or visible laser pulse (typically from a femtosecond laser) passes through a nonlinear crystal and produces a transient polarisation at THz frequencies via second-order nonlinearity. Crucially, this process requires ***non-centrosymmetric*** crystals – only such materials have a nonzero second-order $\chi^{(2)}$ needed for OR [94]. In essence, when a high-intensity femtosecond laser pulse passes through a $\chi^{(2)}$ medium, the second-order polarisation $P^{(2)}(t)$ includes a **difference-frequency** or quasi-static component that oscillates at THz frequencies. Physically, the ultrafast pulse's broad spectrum ω_3 contains many

frequency components that can mix via the $\chi^{(2)}$ nonlinearity (see Fig.2.4). The beating of frequencies ω_1 and ω_2 generates new components at the frequency difference $\omega_3 = \omega_1 - \omega_2$, which falls into the THz range.

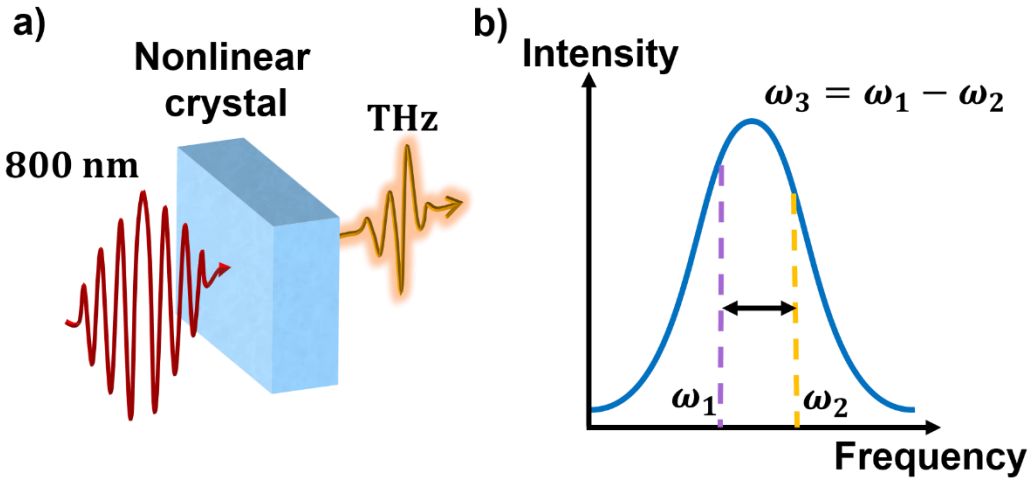

Fig. 2.4. a) Illustration of the optical rectification (OR) process. Optical pulses are converted by a nonlinear crystal, which subsequently generates THz pulses. b) Frequency spectral domain showing the optical rectification as a form of Difference Frequency Generation (DFG) that arises among all possible frequency combinations, from higher to lower, within the laser pulse bandwidth.

The governing equation for nonlinear polarisation $P^{(2)}(t)$ in this process is given by:

$$P^{(2)}(t) = \epsilon_0 \chi^{(2)} E(t)^2. \tag{2.4}$$

Here, $P^{(2)}(t)$ represents the second-order polarisation in the material, serving as the THz field source, ϵ_0 denotes the dielectric constant, $E(t)$ refers to the electric field of the incident laser pulse, and $\chi^{(2)}$ is the crystal's second-order nonlinear susceptibility tensor.

The emergence of a second harmonic in polarisation can be predicted using the following mathematical reasoning: Consider the electric field component, represented as: $E(t) = E_0 \cos(\omega t)$. Substituting this into the polarisation equation provides:

$$P_2 = \epsilon_0 \chi^{(2)} E_0^2 \cos^2(\omega t) = \frac{1}{2} \epsilon_0 \chi^{(2)} E_0^2 (1 + \cos(2\omega t)). \tag{2.5}$$

In this case, the transformation entails the use of the double-angle identity for cos square, which simplifies the overall expression. As can be seen in this equation, the first term represents a constant component, indicative of optical rectification. The second term corresponds to twice the frequency of the original optical field, associated with the dipole oscillations within the medium at that same frequency.

2.3.2. Phase Matching and Pulse Propagation

The effective generation of THz waves requires the phase velocity of the generated THz wave to match the group velocity of the incoming NIR pulses. This is described by the phase-matching condition [95]:

$$\Delta\vec{k} = \vec{k}_1 - \vec{k}_2 - \vec{k}_3 = 0. \quad (2.6)$$

Here, $\vec{k}_1, \vec{k}_2$ represent the wave vectors of the incoming (NIR) pulses with frequencies ω_1, ω_2 and $\vec{k}_3$ is the wave vector of the generated THz with frequency ω_3, (see Fig.2.4(b)). If this condition is not met, then it results in THz waves generated at various locations within the crystal interfering destructively, which diminishes overall efficiency. In many materials, perfect phase matching is challenging due to dispersive differences in the refractive indices for optical and THz waves. Therefore, selecting an appropriate nonlinear crystal is crucial for the effective generation of strong THz pulses.

2.4. Tilted pulse front technique

In traditional optical rectification methods, the THz generation efficiency is limited by the phase mismatch between the optical pulse and the THz wave. This issue is circumvented with the use of the **tilted pulse front technique**.

Tilted pulse front technique is an optimisation technique that enhances the efficiency of optical rectification and which optimises the phase matching condition by adjusting the temporal characteristics of the incident pump pulse. This method, first proposed by Hebling et al. [96], addresses the fundamental limitations of conventional phase-matching techniques, such as those used in periodically poled lithium niobate (PPLN) crystal, and offers a more efficient route for high-energy THz pulse generation. One of the significant advantages of the tilted pulse front technique is the ability to continuously tune the frequency of the generated THz radiation. By varying the tilt angle of the optical pulse front, the THz emission can be tuned across a broad spectral range. This tunability is particularly useful in applications such as THz spectroscopy, where precise control over the THz frequency is necessary for

probing material properties. Experimental demonstrations have shown that the tilt angle can be adjusted to cover the THz range from 0.1 to 4.4 THz, with the possibility of broader tunability depending on the material used [97].

2.4.1. Principle of the Tilted Pulse Front Technique

The core principle of this technique lies in modifying the group velocity of the optical pump pulse to match the phase velocity of the generated THz wave by introducing a tilting angle of the pulse front (Fig.2.5.).

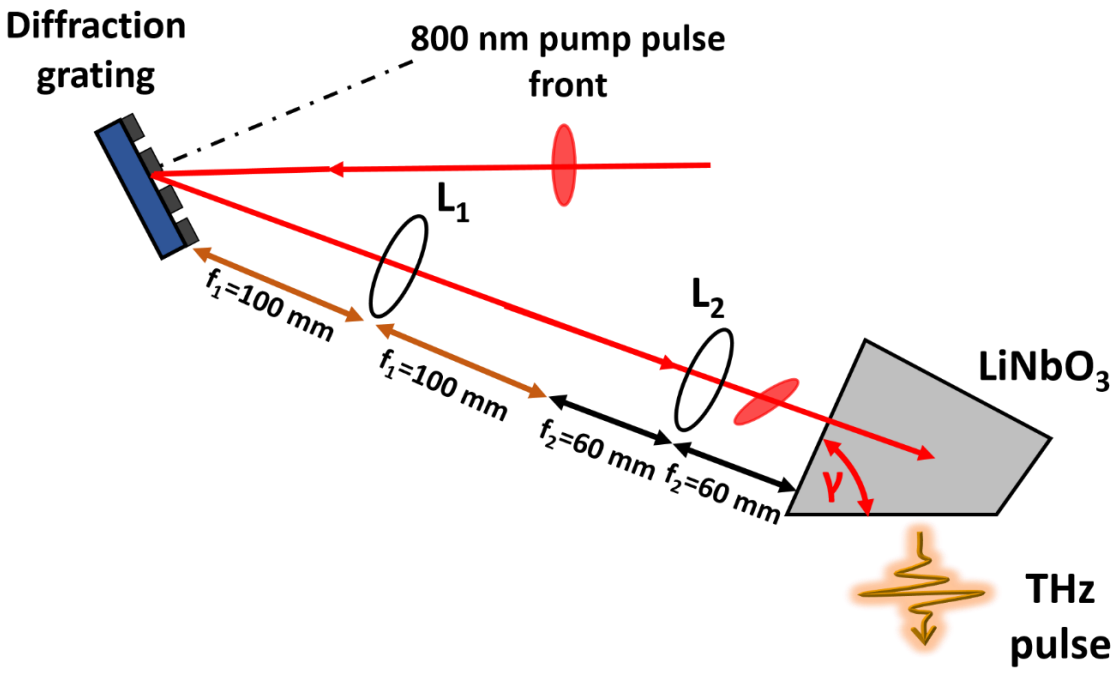

Fig. 2.5. Illustration of the application of the tilted wave front technique in generating intense THz pulses through optical rectification.

This tilt effectively compensates for the differences in the propagation velocities of the optical and THz waves inside the crystal, thus achieving velocity matching over the entire nonlinear interaction.

Mathematically, this velocity matching is expressed as:

$$v_{\mathrm{THz}}^{\mathrm{ph}} = \cos(\gamma)\, v_{\mathrm{NIR}}^{\mathrm{gr}}. \qquad (2.7)$$

Here, $v_{\mathrm{NIR}}^{\mathrm{gr}}$ is a NIR group velocity, $v_{\mathrm{THz}}^{\mathrm{ph}}$ is phase velocity of the generated THz pulse and γ is the angle by which the optical pulse front is tilted. By adjusting the tilt angle, the phase and group velocities of the pump and THz pulses are matching,

which is crucial for efficient THz generation. In our experiments the tilt angle is: 64^0, but our $LiNbO_3$ is cut at 62^0.

2.4.2. Experimental Configuration

The experimental setup for the tilted pulse front technique typically involves several key components: a diffraction grating, a beam-shaping optical system (often a telescope), and a nonlinear crystal such as lithium niobate ($LiNbO_3$), which facilitates the optical rectification process. The diffraction grating is used to introduce angular dispersion into the optical pulse, creating the desired tilt in its temporal front. This spatially tilted pulse which enters the nonlinear crystal, where the interaction between the optical pulse and the material generates THz radiation. To optimise the system's performance, the alignment and configuration of the optical components are crucial. The grating's dispersion must be carefully calibrated to achieve the correct tilt angle, and the beam-shaping lenses must ensure that the pulse remains collimated as it enters the nonlinear medium. Additionally, to reduce the impact of imaging errors—such as distortions in the beam profile due to lens aberrations—a telescopic optical setup, often involving achromatic lenses, is preferred. This setup has been shown to significantly minimize the divergence of the THz beam, ensuring a more stable and focused THz output [98].

2.5. Experimental Setup

In this section, we provide an overview of our intense THz pump-optical probe experimental setup. Firstly, we will point out that in our experiments we used delay line DL325 from Newport company with Bi-directional repeatability (distance error) $R = \pm 0.15\ \mu m$. Therefore, in our measurements the time error is very small: $t = \frac{R}{c} = \frac{15*10^{-8}}{3*10^{8}} = 5 * 10^{-16}$ s.

Fig. 2.6. illustrates our experimental setup containing a titanium sapphire (Ti: sapphire) laser, that emits pulses with a wavelength of 800 nm, a pulse energy of 7 mJ, a pulse width of 40 fs, and a repetition rate of 1 kHz. After the emitted radiation passes through a beam splitter, it separates into the much weaker part, namely probe (1%< of initial pulse power) and the part of the pulse which will be used for THz generation.

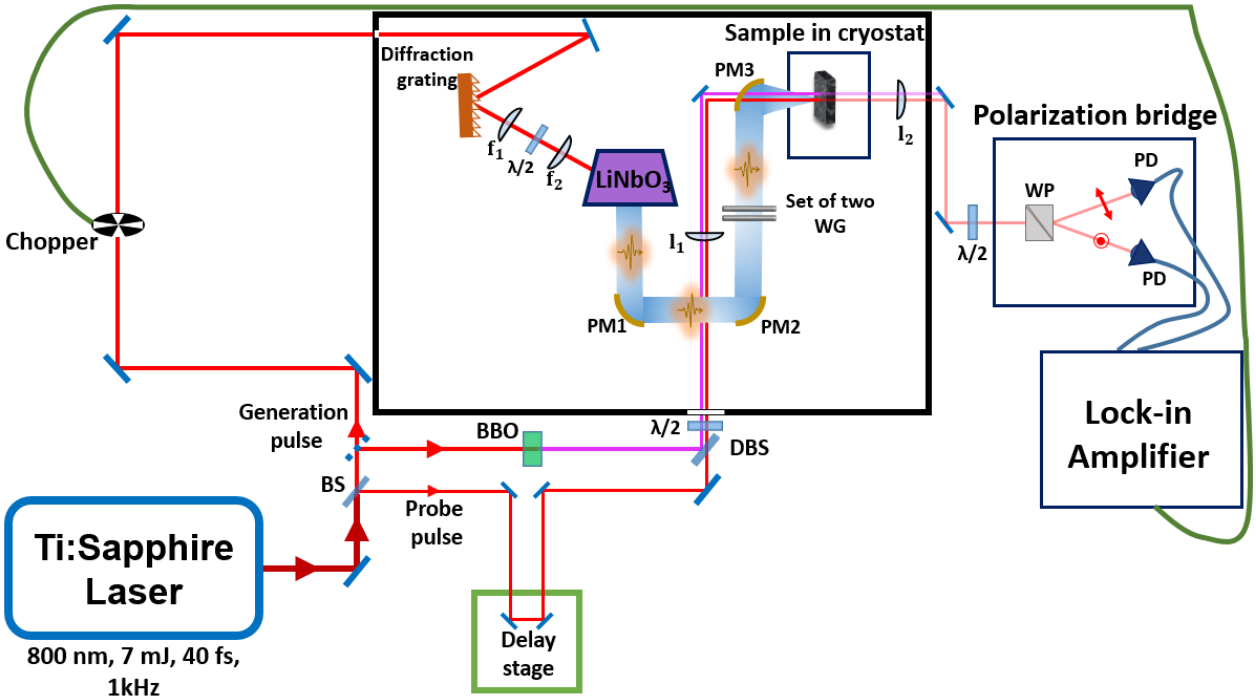

Fig. 2.6. Illustration of intense THz pump-optical probe setup used in our experiments.

THz Generation Pulse Path: The generation part of the laser beam then passes through a chopper, which reduces its repetition rate to 500 Hz (reference signal) which is necessary for the synchronising with lock-in-amplifier. After modulation by the chopper, the generation part of a pulse travels further and reflects from a diffraction grating, which is used to introduce angular dispersion into the optical pulse, creating the desired tilt (more details in section Tilted Pulse Front) in its temporal front. This spatially tilted pulse then enters the nonlinear crystal, where the interaction between the optical pulse and the material generates THz radiation. The residual 800 nm pump is filtered with a teflon plate and redirected using a set of two parabolic mirrors (PM1 and PM2) with focal lengths of 1 inch and 6 inches. Then it passes through the two wire grid polarisers which we use to control the polarisation the incoming THz pulses, after that it directed on the third parabolic mirror (PM3) with focal length of 2 inches which focuses the THz radiation on the sample placed inside a cryostat.

Probe Pulse Path: the probe pulse is delayed via a delay stage to detect pump-induced phenomena within the sample. This pulse travels through a half-wave plate (HWP) and 3rd parabolic mirror (PM3), to probe the sample after its excitation by the pump pulse. This leads to the changes in the probe polarisation state.

Detection Bridge: These changes are analysed by directing the transmitted radiation through another half-wave plate and Wollaston prism onto a polarisation bridge. This signal is then processed by a lock-in amplifier to extract the signal of interest, thereby enhancing the signal-to-noise ratio.

Optical pump: In Chapter 5, we studied THz and optically induced dynamics of Tb ions in Terbium Gallium Garnet ($Tb_3Ga_5O_{12}$) crystal. For this matter we modified our experimental setup by adding an additional mirror (dashed blue line) after beam splitter and installed beta Barium Borate (BBO) crystal (shown as light green rectangular) for the conversion of 800 nm laser pulses into 400 nm (shown in violet colour). Then we modified our setup by adding dichroic beam splitter (DBS) which reflects 400 nm and transmits 800 nm. After that we focused the 400 nm on the sample in the cryostat by using focused lens (l_1).

In the following sections of this chapter we provide more detailed information about the technique used to construct our setup.

2.6. Terahertz Wave Detection

2.6.1. THz detection by Electro-optical sampling

Electro-optic sampling (EOS) is an optoelectronic technique that uses the linear electro-optic (Pockels) effect [99]. This phenomenon is defined by an electric field (like the one from the incoming radiation) that induces birefringence (causes the changes in refractive index value) of a nonlinear crystal, leading to changes in the polarisation state of an optical probe beam. The key components for the EOS technique must include:

1) EO Crystals: Zinc telluride (ZnTe), gallium phosphide (GaP) or gallium arsenide (GaAs) are favoured due to their high electro-optic coefficient and broad detection bandwidth.
2) Balanced Detectors: The modulated probe beam splits into two orthogonal components by Wollaston prism and quarter-wave plate is used for monitoring changing in ellipticity and a Wollaston prism, which aids in reconstructing the field.

For our EOS experiments, a GaP nonlinear detection crystal with a thickness of 100 µm [100] was placed in the sample position of our setup as shown in Fig.2.7.

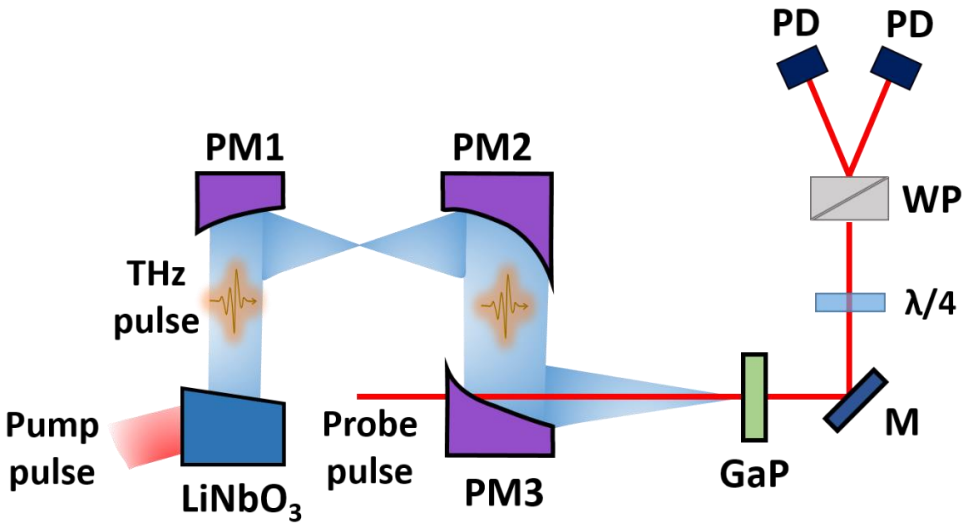

Fig. 2.7. Schematic of the EO sampling setup. The off-axis parabolic mirrors PM1, PM2, and PM3 have effective focal lengths of 25.4, 152.6, and 50.8 mm, respectively. Their respective diameters are 10, 50, and 50 mm. M: mirror, λ/4: quarter-wave plate, WP: Wollaston prism, PD: photodetector.

The THz wave's electric field induces temporary birefringence which is linearly proportional to the strength of the applied electric field in the detector crystal through the Pockels effect. This effect alters the properties of the probe pulse, changing its polarisation from linear to elliptical. The resultant change, proportional to the THz field strength, is detected by a balanced photodiode setup. Analysis of the photodiode's output, relative to the time delay between the THz and probe pulses, allows for accurate reconstruction of the THz field profile in the time domain.

To ensure that we obtain clear THz profiles independent of air humidity, we used a purge box with dry air. Figure 2.8 shows the THz profiles and the corresponding spectrum without the box and humid air and with the box and purge dry air.

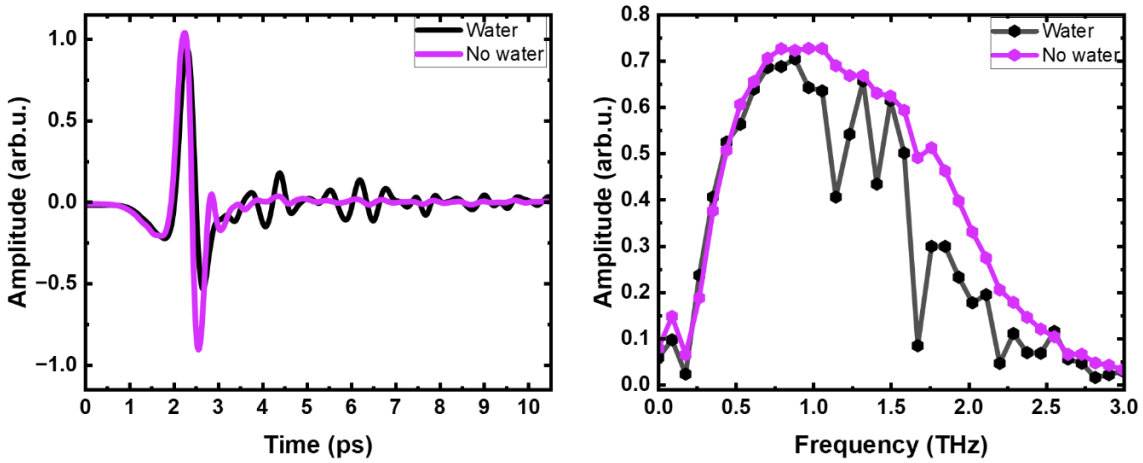

Fig. 2.8. a) THz wave profiles in humid air (black) and dry air (violet) and their spectra; b) obtained with the use of TTLP technique and measured with the use of EOS.

Chapter III. Theory of THz-driven magnetic switching in rare-earth orthoferrites: the case of $TmFeO_3$

"If it (your guess or theory) disagrees with experiment, it's wrong. In that simple statement is the key to science."

— Richard Feynman

This chapter reports a theoretical formalism that describes a dynamic magnetic response of rare-earth orthoferrites (REOs), particularly those with non-Kramers rare-earth (R) ions, when driven by strong THz fields. We derive a total thermodynamic potential for the exchange coupled R-Fe system by constructing an effective Hamiltonian and employing a mean-field theory approximation. We investigate static properties of the R and Fe subsystems across the spin reorientation phase transitions and obtain resonance frequencies for Fe and R magnetic sub-lattices as a function of temperature. Taking an example of the archetypical orthoferrite $TmFeO_3$, we perform numerical modelling to accurately describe the behaviour of its anisotropy functions vs temperature. Finally, we analyse switching dynamics of Fe spins and nonlinear effects in the R subsystem of $TmFeO_3$ driven by strong THz radiation.

3.1. Motivation

Rare-earth orthoferrites, with a chemical formula of $RFeO_3$, have been attracting significant attention since their discovery in the 1940s due to their unique magnetic properties [101–103]. The coexistence of two different magnetic ions (R^{3+} and Fe^{3+}) in this class of magnetic oxides results in a unique combination of various effects and phenomena such as spin reorientational phase transitions (SRPT) [104–110], strong magneto-optical effects [111–114], high-frequency spin dynamics [115–120], high-harmonic generation [121], strong magneto-elastic effects [122–125], multiferroicity [126–129] and as a new platform to simulate the quantum optics phenomena [130–133]. In this way orthoferrites proved to be a remarkable model system for several fields of physics. Beside this scientific importance, orthoferrites served as a prototypical platform for the bubble domain memory [30].

In the past two decades, the orthoferrites have gained renewed interest as a proof-of-concept platform for ultrafast magnetism with significant implications for spintronic applications. It has been experimentally demonstrated that circularly-polarised femtosecond (fs) laser pulses can induce ultrafast non-thermal control in $DyFeO_3$ [134] and that SRPT phenomena are highly sensitive to external optical excitation [135,136]. Very recently, the $RFeO_3$ class became a subject of extensive investigations in the field of nonlinear phononics [37–40] and magnonics [141,142]. Nova and colleagues [138] explored effects of optically driven phonons in $ErFeO_3$. They found that simultaneous excitation of multiple lattice modes can mimic the application of a magnetic field, breaking time-reversal symmetry and thereby driving coherent spin precession. Afanasiev, et al [139] focused on the resonant ultrafast excitation of IR-active phonons in $DyFeO_3$, leading to coherent manipulation of macroscopic magnetic states. By using intense mid-infrared electric field pulses, they induced long-lasting changes in the exchange interaction between Dy^{3+} and Fe^{3+} ions. The magnonics research on $RFeO_3$ materials underscores their potential for future spin wave-based computing. Studies made by Hortensius, et al. [141] regarding spin-wave transport in $DyFeO_3$, the recent work of Leenders, et al. [142], describing canted spin order as a platform for the ultrafast conversion of magnons, together with the theoretical studies [143] on this topic collectively highlight the transformative potential of $RFeO_3$ in enabling high-speed, low-dissipation information transfer through coherent spin waves. As research progresses, these materials will likely play a pivotal role in developing next-generation magnonic and spintronic technologies.

However, it should be pointed out that while optical and infrared pulses can induce changes in magnetism, they do so indirectly via electronic or phononic excitations. However, the development of THz time-domain spectroscopy (THz-TDS) techniques allowed the study of various types of excitations, including spin dynamics, by directly interacting with atomic spins using THz radiation. This method offers more precise and controlled manipulation of magnetisation dynamics in magnetic materials through the resonant excitation of spins by strong ultrashort THz magnetic field [144–149]. Another interesting idea was to use intense THz fields to achieve control over nonlinear spin reorientation transition and switch of iron spins in REOs due to the changing crystalline magnetic anisotropy via R subsystem, which is driven by laser pulses [150–152]. In [151] Baierl, et al. demonstrated that in $TmFeO_3$ the resonant THz pumping of electronic orbital transitions significantly alters the magnetic anisotropy of Fe^{3+} spins, leading to coherent spin oscillations with large amplitudes. This mechanism is inherently nonlinear and can be tailored by shaping the THz waveforms, offering a more efficient control scheme compared to

linear Zeeman coupling. In [152] Schlauderer, et al. expanded this approach by demonstrating ultrafast all-coherent spin switching by combining electric-field-induced anisotropy changes with the local near-field enhancement from metal antennas.

However, the complementary theoretical description of the ultrafast dynamics in the orthoferrites remains a challenge. Only the role of the Fe subsystem has been well understood, and the role of the R subsystem is still a blind spot. The first quantum-phenomenological approach for describing REOs was proposed and successfully verified in a series of works [108,115,116], with a more detailed explanation provided in [153]. The main idea of this approach is to consider the crystal field's influence on the properties of rare-earth ions by constructing microscopic Hamiltonians accounting for interactions with the crystal field, *d-f exchange* and internal *f-f* exchange. These Hamiltonians are not calculated from first principles but constructed using the general symmetry properties of the system and known data on the specific spectrum of the rare earth ion in the crystal. The parameters of these Hamiltonians are extracted from the experiment. Then by applying mean-field theory approach one should derive thermodynamic potential (Helmholtz free energy) to describe Fe and Re subsystems in a macrospin approximation.

However, it should be pointed out that these earlier theoretical works did not consider the strong optical and THz excitations of the orthoferrites at the ultrafast timescale and, therefore, can only provide a basis for further theoretical description of the current experiments. Recent studies have increasingly focused on the role of the rare-earth (R) subsystem in orthoferrites featuring Kramers ions, such as $SmFeO_3$, $DyFeO_3$, and $NdFeO_3$. For instance, the research reported in [154] investigated the contributions of the samarium (Sm) subsystem to the magnetism of $SmFeO_3$. Concurrently, work [155] revealed that interactions between iron and samarium spins result in pronounced spin-phonon coupling. In [156], the authors introduced a model for temperature-driven spin switching and exchange bias in $ErFeO_3$, while in [157], they proposed a model of nonequilibrium thermodynamics for the same compound. Additionally, reference [59] combined experimental results with theoretical analysis to elucidate the spin-reorientation phase transition and induced spin reversals in $NdFeO_3$. References [60] and [61] explored the implications of external radiation on $DyFeO_3$ using quantum theory. In this work, we aim to develop a theoretical model that can describe the nonlinear spin dynamics in REOs with non-Kramers ions driven by strong THz radiation. Our approach takes

into account the coupled nature of dynamics of Fe and R systems to correctly relate the effects of strong THz fields on REOs.

The chapter is organized as follows. In Section 3.2. we discuss the theoretical foundations necessary for the further theoretical investigations of static and dynamical properties $RFeO_3$ with non-Kramers ions, namely an effective microscopic Hamiltonian is constructed that accounts for the effects of crystal field interaction with R, *d-f exchange*, *f-f* exchange, interaction with external electro-magnetic fields caused by THz radiation. Then, by applying the mean-field approach to the Hamiltonian, the free energy function or a total thermodynamic potential for $RFeO_3$ with non-Kramers rare-earth ions is derived. Section 3.3 starts with the description of the static properties of REOs over a broad temperature range, with anisotropy temperature functions retrieved from the free energy function for archetypical orthoferrite $TmFeO_3$ as an example. Then it focuses on the dynamical properties of $TmFeO_3$. Firstly, resonance frequencies for the coupled Tm-Fe subsystems are derived. Secondly, numerical modelling is performed to investigate the spin response to the Zeeman torque caused by the magnetic field component of a THz pulse. Then, the influence of the anisotropy-driven torque caused by THz pumping of orbital states of Tm^{3+} ions, either through the Zeeman or Stark effects, is investigated. In Section 3.4, the results of the work are summarized. Appendix sections 3.5-3.8 provide supplementary information about the obtained theoretical results.

3.2. Theoretical formalism

REOs belong to a wide class of compounds of the ABO_3 type, which have a distorted perovskite structure (Fig.3.1). The crystal structure of orthoferrites is described by the rhombic space group $D_{2h}^{16} - P_{bnm}$ [161,162]. Their unit cell contains four $RFeO_3$ molecules (see Fig. 1). Since the crystal and magnetic cells in orthoferrites coincide, then to characterise the magnetic structures as a whole, one can use four magnetic sublattices of Fe^{3+} ions and four of R^{3+} ions.

However, to describe qualitatively and quantitatively the magnetic properties of $RFeO_3$, the two-sublattice approximation [153,163] is normally sufficient. Therefore, we employ it in this work. The relative strength of the various microscopic interactions determines the specific type of magnetic structure in REO crystals.

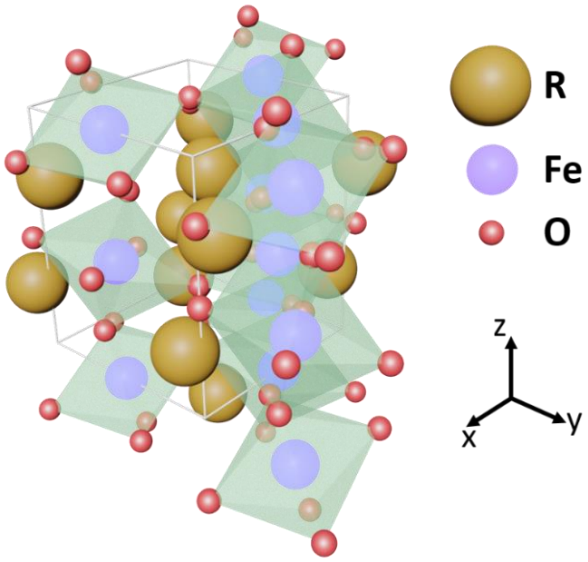

Fig.3.1. Distorted perovskite structure of the rare-earth orthoferrites[3].

The strongest one is the antiferromagnetic exchange Fe-Fe interaction, which leads to ordering of the Fe^{3+} spins according to the G-type (i.e. Néel or checkerboard structure where nearest-neighbour spins are aligned antiparallel). The corresponding Neel temperatures for the different orthoferrites are in a range 620-740 K [164,165]. Weaker (anisotropic) interactions cause the magnetic moments to deviate from the purely antiferromagnetic configuration and stabilize their orientation relative to the crystal axes. The most important between them is the antisymmetric Fe-Fe Dzyaloshinskii-Moriya exchange (DMI), which leads to spin canting and thereby to the appearance of a weak ferromagnetic moment. The same interaction, along with the single-ion anisotropy of the Fe subsystem and the spin-spin dipole interactions, contributes to the energy of the magneto-crystallographic anisotropy, which in turn defines the orientation of the magnetic order parameter of REOs [166,167].

It should be noted that for all the importance of these interactions of the Fe subsystem, considering these interactions alone is not sufficient to explain the wide variety of magnetic properties of orthoferrites. At room temperature, the effect of rare-earth ions on the magnetic properties of orthoferrites is insignificant. This is evidenced, in particular, by the fact that almost all orthoferrites (except $SmFeO_3$), at high temperatures have the same magnetic configuration Γ_4, for which the iron spins lie along *a*-axis of the crystal. This Γ_4 magnetic phase is stabilized by the anisotropy energy of the Fe subsystem [165]. However, upon decreasing of temperature the

[3] Picture is a courtesy of Dr. Oleksandr Kovalenko

properties of REO, are largely determined by the type of rare-earth ion, which manifests itself in various temperature dependences of the weakly ferromagnetic moment of the crystal, the presence of magnetisation compensation points and, mainly, the existence of various spin reorientational phase transitions (SRPT), both spontaneous and induced by an external magnetic field. It has been established [153] that such a variety of properties of orthoferrites is associated primarily with the individual features of the magnetism of the R-ion in the crystal and its interaction with the subsystem of Fe-ions via so-called *d-f* exchange anisotropic interaction. This is due to the fact that the isotropic R-Fe exchange of a pair of Fe^{3+}-R^{3+} ions is almost completely compensated in the crystal due to the antiferromagnetic ordering of the Fe subsystem. As for the weaker R-R interaction, it is important only at low temperatures ($T < 5$ K), leading in some cases to the antiferromagnetic ordering of the R subsystem.

In the existing theoretical description of rare-earth oxides, it is essential to note that the commonly used phenomenological approach is insufficient to describe the R subsystem's properties in contrast to the Fe subsystem. Instead, the microscopic one is more efficient [108,153]. In it, the R subsystem is described with the help of microscopic Hamiltonians including the crystal field, *d-f* exchange, *f-f* exchange and so on, which are obtained by using the symmetry properties of the system, as well as known experimental data on the actual spectrum of rare-earth ions. The parameters of these Hamiltonians should be ultimately determined from experiments. Moreover, such an approach is potentially more productive in investigating the dynamical properties of REOs for Fe and R subsystems, which are, strictly speaking, coupled. This allows applying two sublattice approximations and, as a result, solving two sets of equations of motion to get pair of two resonance modes for the Fe and R subsystems and to investigate their dynamical features in a broad temperature range.

Also one should take into account that when it comes to the theoretical description of $RFeO_3$ one should distinguish cases with Kramers (odd number of *4f* electrons) and non-Kramers ions (even number of *4f* electrons). According to Kramers' theorem, any ion with an odd electron count (half-integer total angular momentum $\vec{J}$) retains at least a double degeneracy (a *Kramers doublet*) under time-reversal symmetry, no matter how low the crystal-field symmetry. In contrast, an even-electron (integer $\vec{J}$) ion is not guaranteed any such protected degeneracy; a low-symmetry crystal field can fully split its ground multiplet into nondegenerate singlets (though sometimes two lowest singlets lie close in energy as a "quasi-doublet"). This distinction leads to very different magnetic behaviour. In zero field, both Kramers

and non-Kramers ions have no net moment (either due to exact doublet state cancellation for Kramers, or a nonmagnetic singlet wavefunction for non-Kramers). However, any small internal or external field will split a Kramers doublet and induce a magnetic moment (Curie-like paramagnetism). A non-Kramers singlet, on the other hand, is magnetically inert to first order – it only develops moment via excited-state mixing (Van Vleck susceptibility). In essence, Kramers ions behave as robust magnetic moments at low temperature, whereas non-Kramers ions often behave as "Ising" or easy-axis singlets that can be magnetised only by stronger fields or thermal population of higher levels. From a theoretical point of view, according to existing literature [124,125], the situation with Kramers ions is more complicated due to the larger number of terms in the thermodynamic potential responsible for *f-d* and *f-f* exchange interactions.

Therefore, in our theoretical model, the ultimate goal is to describe equilibrium and non-equilibrium properties for the case of non-Kramers REO by constructing the effective Hamiltonian and then to derive the total thermodynamic potential, which includes all interactions between Fe-R subsystems while taking into account effects caused by THz radiation. As an indicative material of interest, we choose $TmFeO_3$, due to its well-established magnetic properties, and since it has been employed in the recent ultrafast and THz experiments [135,151,152,168,169].

3.2.1. Thermodynamic potential for Fe-subsystem

To describe the Fe-subsystem, a phenomenological (macroscopic) approach [120,153,170] can be employed, which is based on the expansion of the thermodynamic potential for the Fe subsystem (Φ_{Fe}) in terms of the powers of the components of the basis vectors $\vec{F}$ and $\vec{G}$:

$$\begin{aligned}\Phi_{\mathrm{Fe}}(\vec{F},\vec{G}) &= \frac{1}{2}A\vec{F}^2 - d(F_xG_z - F_zG_x) - M_0\vec{F}\vec{H} + \\ &+ \frac{1}{2}(K_{\mathrm{ac}}G_z^2 + K_{\mathrm{ab}}G_y^2 + K_2''G_y^2G_z^2) + \frac{1}{4}(K_2G_z^4 + K_2'G_y^4).\end{aligned} \tag{3.1}$$

Here, the first term corresponds to the *d-d* exchange interaction, the second is the Dzyaloshinskii-Moriya exchange interaction, the third term is the Zeeman effect, and 4th and 5th correspond to the magneto-crystalline anisotropies. $\vec{F} = \frac{\vec{M}_1+\vec{M}_2}{M_0}$ and $\vec{G} = \frac{\vec{M}_1-\vec{M}_2}{M_0}$ are defined as dimensionless vectors of ferromagnetism and

antiferromagnetism, expressed as a half-sum and half-difference of two magnetisation sub lattices $\vec{M}_1$ and $\vec{M}_2$. These vectors comply with the conditions $\vec{G}^2 + \vec{F}^2 = 1$ and $(\vec{F}\vec{G}) = 0$. Here, $M_0 = 5\mu_B$ denotes the magnetisation of the Fe sublattices, with μ_B representing a Bohr magneton. *A* is defined as the isotropic *d-d* exchange constant and *d* is Dzyaloshinskii constant, $\vec{H}$ is identified as the external magnetic field, while K_{ac}, K_{ab}, K_2, K_2', K_2'' are the crystallographic anisotropy constants. Here, *x,y,z* coordinate frame is aligned with the *a,b,c* crystallographic axes respectively. One may introduce additional terms in (3.1), consistent with the symmetry of the crystal, but we present a minimal model that captures the essential dynamics of rare-earth orthoferrites without introducing excessive complexity.

At the same time, it should be noted that in rare earth orthoferrites, the anisotropy energy includes contributions from various interactions, such as those between iron and rare earth ions sublattices. Because of this, the anisotropy constants significantly depend on temperature and rare-earth subsystem, which can lead to spin reorientation phase transitions [107]. In this regard the rare-earth subsystem should be introduced.

3.2.2. Effective Spin-Hamiltonian for the R-subsystem

The central problem in the magnetism of orthoferrites is the description of the R-subsystem by considering the real spectrum of R^{3+} ion in a low-symmetry crystal field of C_s symmetry and its exchange interaction with the Fe subsystem. In this paper, we present the theory for the orthoferrites with non-Kramers R^{3+}-ions (with an even number of electrons and integer total angular momentum), taking archetypical $TmFeO_3$ as a model system. We assume that the largest contribution to the magnetic properties of Tm^{3+} arise from the two lowest-energy singlet levels of Tm^{3+} ion. Thus we consider it as two-level system with effective spin $S_{\text{eff}} = \frac{1}{2}$. This significantly simplifies the problem and allows one to described it by constructing effective spin Hamiltonian [120,153]. Moreover, one should bear in mind that in REOs THz radiation can excite not only resonant Zeeman type excitations of iron magnons, but electronic excitations of R^{3+} ions via the Zeeman and Stark effects.

Therefore, by taking all these interactions into account effective spin Hamiltonian for the REO with non-Kramers ions can be presented in the following form:

$$H_{\text{eff}} = -\sum_i \Big(\underbrace{\Delta_{\text{cf}}\sigma_\zeta^i}_{\substack{\text{crystal field}\\ \text{interaction}}} + \underbrace{\alpha E^2 \sigma_\zeta^i}_{\substack{\text{Stark}\\ \text{effect}}} + \underbrace{\vec{\mu}_0^i \vec{\mathrm{H}} \sigma_\xi^i}_{\substack{\text{interaction}\\ \text{with external}\\ \text{magnetic field}}} + \underbrace{(a\vec{\mathrm{F}}\vec{\mu}_0^i + bG_z)\sigma_\xi^i}_{\substack{\text{f-d exchange}\\ \text{interaction}}} \Big) -$$

$$-\frac{1}{2}\sum_{i,j} \underbrace{\lambda_{ij}\sigma_\xi^i \sigma_\xi^j}_{\substack{\text{f-f}\\ \text{exchange}\\ \text{interaction}}}. \qquad (3.2)$$

Here, ξ, η and ζ are indices for the axes to a local coordinate system of R sublattices. In this formula $\sigma_{\xi,\zeta} = \langle \sigma_{\xi,\zeta} \rangle$, representing the mean values of the Pauli matrices for the two-level system representing the R^{3+} ion. These matrices are crucial for determining the relative magnitude and the magnetic moment of a R. Δ_{cf} denotes the energy splitting in the crystal field, and α represents the polarisability coefficient. $\vec{H}$ and $\vec{E}$ symbolize the external electric and magnetic fields (i.e. those of the THz pulse), respectively and $\vec{\mu}_0 = \vec{\mu}_0^{\pm} = (\mu_x, \pm\mu_y, 0)$ is the magnetodipolar moment of the two-level transition. The *a* and *b* denote isotropic and anisotropic *d-f* exchange interaction constants, respectively, and λ_{ij} represent *f-f* exchange interaction constants. The first term under the first sum sign is the strongest interaction, i.e., the interaction of the R with the crystal field, the second term accounts for the Stark effect caused by an external electric field, the third for the linear interaction of R^{3+} ions with external magnetic radiation, and the fourth term for *d-f* exchange interaction. Lastly, the final sum term is responsible for considering the summation of the nearest R^{3+} ions for the low-temperature *f-f* exchange.

3.2.3. Thermodynamic potential for coupled Fe-R system

In order to qualitatively investigate the statistic and dynamic properties of the coupled Fe and R subsystems, one should derive thermodynamic potential which accounts for the all interactions within the system as well as interactions with external fields.

By following the approach outlined in [153] such thermodynamic potential can be represented as follows:

$$\Phi(\vec{F}_\alpha, \vec{G}_\alpha, \vec{\sigma}_{i\alpha}) = \Phi_d(\vec{F}_\alpha, \vec{G}_\alpha) + \left\langle H_{\text{eff}} \right\rangle - \frac{1}{4} T \sum_{i=1}^{4} S(\sigma). \qquad (3.3)$$

Here, $S(\sigma) = \ln 2 - \frac{1}{2}(1+\sigma_1)\ln(1+\sigma_1) - \frac{1}{2}(1-\sigma_2)\ln(1-\sigma_2)$ is the entropy function for the two-level system. In analogy to the $\vec{F}$ and $\vec{G}$ vectors, one can introduce the following symmetric combinations of R-vectors $\vec{f} = \frac{\vec{\sigma}_1 + \vec{\sigma}_2}{2}, \vec{c} = \frac{\vec{\sigma}_1 - \vec{\sigma}_2}{2}, \sigma_{1,2} = \left|\vec{f} \pm \vec{c}\right|$ [116,171] $\langle \widehat{H}_{\text{eff}} \rangle$ is the averaged value of the effective spin Hamiltonian per one rare-earth spin from equation (1).

Considering the expression for $\Phi_{\text{Fe}}(\vec{F}, \vec{G})$ from (1) the total thermodynamic potential for the R-Fe subsystem with non-Kramers R ions can be written in the explicit form:

$$\Phi(\vec{F},\vec{G},\vec{f},\vec{c}) = \Phi_{\text{Fe}}(\vec{F},\vec{G}) - \{ f_\xi[\mu_x(H_x + aF_x) + bG_z] + f_\zeta \Delta_{\text{cf}} + \alpha(E_x^2 + E_y^2) f_\zeta + \\ + c_\xi \mu_y (H_y + aF_y) + \frac{1}{2}\lambda_f f_\xi^2 + \frac{1}{2}\lambda_c c_\xi^2 \} - \frac{1}{2}T[S(\sigma_1) + S(\sigma_2)]. \quad (3.4)$$

In this formula, the $\Phi_{\text{Fe}}(\vec{F}, \vec{G})$ term includes all interactions for the Fe subsystem from (1), the first term in the brackets describes the anisotropic *d-f* exchange, the second is responsible for the interaction of the R-subsystem with a crystal field, the third for the linear interaction with external electromagnetic fields, the fourth – for the Stark effect, the fifth and sixth are for the *f-f* exchange, and seventh describes a thermal population effect.

3.3. Results

3.3.1. Static magnetic properties. Anisotropy parameters behaviour

In the investigation of the static magnetic properties of REOs one should take into account the magnetic phase diagram summarized in [172], which delineates special temperature regions, where spin reorientational phase transition (SRPT) phenomena occur. It is essential to note that SRPTs can be categorized as either first-order (Morin-type) or second-order phase transitions. However, in the present article we will concentrate on the most prevalent path of spin reorientation transitions Γ_2-Γ_{24}-Γ_4, in which $\vec{G}$ continuously rotates in *xz* plane as schematically shown in Fig.3.2. This path is observed for the $RFeO_3$, with R elements including Pr, Nd, Sm, Tb, Ho, Er, Tm and Yb.

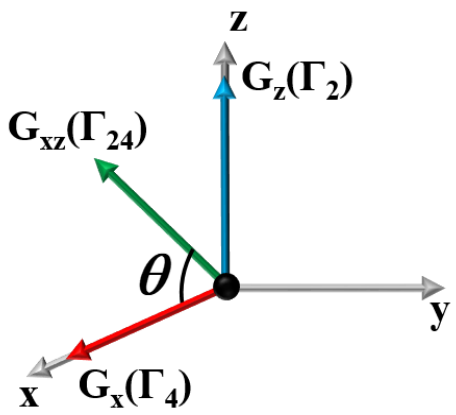

Fig.3.2. Illustration of the dynamics of the antiferromagnetic vector $\vec{G}$ across three temperature phases.

The mechanism of spin reorientation phase transitions (SRPT) Γ_2-Γ_{24}-Γ_4 in the Fe-R system is driven by two primary factors: anisotropy and *d-f* exchange interactions. At elevated temperatures, the Fe spins adopt the high-temperature Γ_4 phase, characterised by the presence of only G_x component. As the temperature is reduced to a critical value T_1, the anisotropy parameter K_{ac} is fully compensated by the *d-f* exchange interaction, thereby initiating the SRPT phenomenon. This induces a rotation of the $\vec{G}$ within the *xz* plane. Upon further cooling to temperature T_2, the SRPT culminates, resulting in the $\vec{G}$ vector aligning along the G_z vector component within the low-temperature Γ_2 phase. Therefore, the question arises about theoretical description of anisotropy functions as a function of temperature and the behaviour of the antiferromagnetic vector $\vec{G}$ along the SRPT temperature path Γ_4-Γ_{24}-Γ_2.

In this regard, let us apply our model to describe this behaviour. From now on all terms/their combinations in formula (3.4) will be expressed in Kelvin units (see Appendix D). To commence our analysis for $\vec{G}$ and anisotropy functions within the *xz* plane, one should calculate the equilibrium values of the subsystem parameters in magnetic phases $\Gamma_4, \Gamma_{24}, \Gamma_2$ and analysing their stability. For that matter by minimizing the thermodynamic potential (TP) from Eq. (3.4) with respect to $\vec{F}, \vec{f}$ and $\vec{c}$ under the conditions $(\vec{F}\vec{G}) = 0$, $\vec{F}^2 + \vec{G}^2 = 1$ and $(\vec{f}\vec{c}) = 0$, $\vec{f}^2 + \vec{c}^2 = f_0^2 = \tanh^2[\frac{\Delta_R}{k_B T}]$, one can obtain for the phases $\Gamma_4, \Gamma_{24}, \Gamma_2$: $F_y = 0, f_\eta = 0, \vec{c} = (c_\xi, c_\eta, c_\zeta) = 0$, (see Appendix A for more details):

$$\begin{cases} F_x = \dfrac{dG_z + af_\xi \mu_x}{A},\ F_y = 0,\ F_z = -\dfrac{dG_x}{A}, \\ f_\xi = f_0 \sin\psi = \dfrac{\Delta_{ex}^0 G_z}{(\tilde{T} - \tilde{\lambda}_f)},\ f_\eta = 0, f_\zeta = f_0 \cos\psi, \\ \vec{c} = (c_\xi, c_\eta, c_\zeta) = 0. \end{cases} \tag{3.5}$$

$$\begin{cases} \sin\psi = \dfrac{\Delta_{ex}}{\Delta_R},\ \cos\psi = \dfrac{\Delta_{cf}}{\Delta_R}, \\ f_0 = \tanh[\dfrac{\Delta_R}{k_B T}],\ \tilde{T} = \dfrac{\Delta_R}{\tanh[\dfrac{\Delta_R}{k_B T}]}. \end{cases} \tag{3.6}$$

$$\begin{cases} \Delta\lambda_f = \dfrac{(a\mu_x)^2}{A}, \Delta_{ex}^0 = b + \dfrac{ad\mu_x}{A}, \\ \tilde{\lambda}_f = \lambda_f + \Delta\lambda_f, \Delta_{ex} = G_z \Delta_{ex}^0 (1 + \dfrac{\tilde{\lambda}_f}{(1-\tilde{T})}). \end{cases} \tag{3.7}$$

$$\Delta_R(T) = \sqrt{\Delta_{ex}^2(T) + \Delta_{cf}^2}\,. \tag{3.8}$$

Here, $\Delta_R(T)$ is the total energy splitting parameter, expressed as the square root of the crystal field splitting Δ_{cf} and the contribution arising from the *d-f* exchange $\Delta_{ex}(T)$. By substituting equations (3.5) – (3.8) into (3.4) one can obtain a TP depending only on $\vec{G}$. In collinear phases $G_x = \pm 1, G_z = 0$ (Γ_4) and $G_z = \pm 1, G_x = 0$ (Γ_2).

The stability of the Γ_2 and Γ_4 phases is determined by the condition of positive sign of the increment $\Phi(\vec{G})$ in case of deviation of $\vec{G}$ from the equilibrium values:

$$\Delta\Phi_{\Gamma_4} = \frac{1}{2}(K_{ac}^{eff} \Delta G_z^2 + K_{ab}^{eff} \Delta G_y^2),\ \Delta\Phi_{\Gamma_2} = \frac{1}{2}(K_{ca}^{eff} \Delta G_x^2 + K_{cb}^{eff} \Delta G_y^2). \tag{3.9}$$

Therefore for the phases Γ_2, Γ_4, one can get the following expressions for the anisotropy functions:

$$K_{ac}^{eff}(T)=\left(K_{ac}^{0}-\frac{(\Delta_{ex}^{0})^{2}}{(\tilde{T}-\tilde{\lambda}_{f})^{2}}(\tilde{\lambda}_{f}-\frac{2}{(\tilde{T}-\tilde{\lambda}_{f})})\right), \quad (3.10)$$

$$K_{ab}^{eff}=\left(K_{ab}^{0}+\frac{d^{2}}{A}\right), \quad (3.11)$$

$$K_{ca}^{eff}(T)=\left(-K_{2}-K_{ac}^{0}+\frac{(\Delta_{ex}^{0})^{2}}{(\tilde{T}-\tilde{\lambda}_{f})^{2}}(\tilde{\lambda}_{f}+\frac{2}{(\tilde{T}-\tilde{\lambda}_{f})})\right), \quad (3.12)$$

$$K_{cb}^{eff}(T)=\left(K_{ab}^{eff}-K_{ac}^{0}+2K_{2}+K_{2}''+\frac{(\Delta_{ex}^{0})^{2}}{(\tilde{T}-\tilde{\lambda}_{f})^{2}}(\tilde{\lambda}_{f}+\frac{2}{(\tilde{T}-\tilde{\lambda}_{f})})\right), \quad (3.13)$$

The values of anisotropy functions $K_{ac}^{eff}(T), K_{ab}^{eff}, K_{ca}^{eff}(T), K_{cb}^{eff}(T)$ determine resonance frequencies (which we will derive in section B) for the Fe subsystem and characterise the rigidity of the system when deviating from the equilibrium orientations considering that vectors $\vec{F}, \vec{f}, \vec{c}$ follow order parameter $\vec{G}$ in equilibrium manner. At $k_B T \gg \Delta_R(T)$, when $\tilde{T} \to T$, the effective anisotropy functions approach to the normal anisotropy constants in the corresponding planes. The TP of the $TmFeO_3$ in this case can be represented as $\Phi(\vec{G}) = \Phi_A(\vec{G})$, in which one just need to replace $K_{ab,ac}^{eff}(T) \to K_{ab,ac}$:

$$\Phi_A(\vec{G})=\frac{1}{2}(K_{ac}G_z^2+K_{ab}G_y^2+K_2''G_y^2G_z^2)+\frac{1}{4}(K_2G_z^4+K_2'G_y^4) \quad (3.14)$$

Within the phase $\Gamma_{24,}$ the equilibrium values of the components of the vector $\vec{G}$ are given by the equations:

$$G_z=\sin\theta=\sqrt{-\frac{K_{ac}^{eff}(T)}{K_2}},\ G_x=\cos\theta=\sqrt{1+\frac{K_{ac}^{eff}(T)}{K_2}} \quad (3.15)$$

Using the derived formulas (3.10) and (3.12) for anisotropy functions $K_{ac}^{eff}(T), K_{ab}^{eff}(T)$ as well as formulas (3.8) and (3.15) for $\Delta_R(T)$ and G_z and by extracting relevant parameters for $TmFeO_3$ from [125], we performed numerical modelling in the temperature range corresponding to the spin reorientation path Γ_2-Γ_{24}-Γ_4 (see Fig.3 a,b,c).

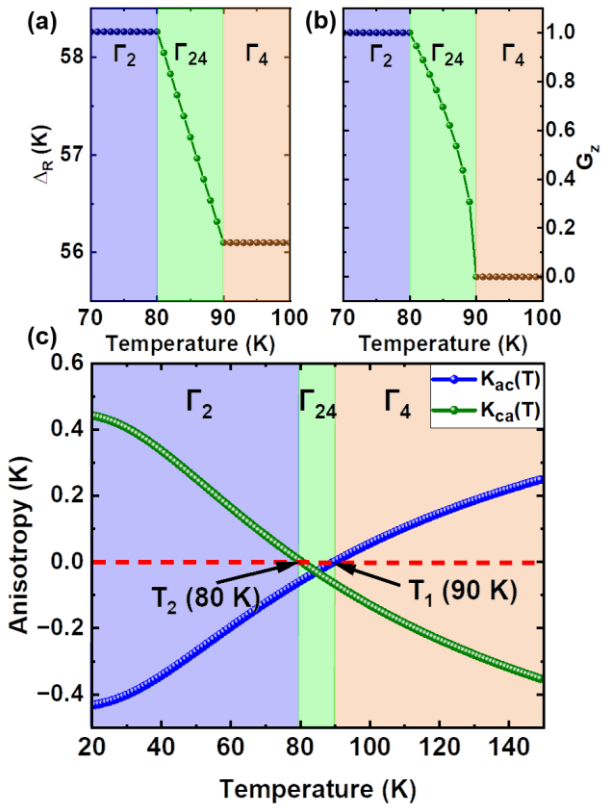

Fig.3.3. Temperature dependencies over the Γ_2-Γ_{24}-Γ_4 temperature interval for (a) energy splitting parameter $\Delta_R(T)$, (b) antiferromagnetic vector component G_z and (c) the effective anisotropy functions $K_{ac}^{eff}(T), K_{ca}^{eff}(T)$ for $TmFeO_3$.

As one can see (Fig.3.3. (a,b,c)), from the obtained formulas in our model, we were able to recreate the behaviour of all major temperature dependent functions namely energy splitting parameter $\Delta_R(T)$, antiferromagnetic vector component G_z and the effective anisotropy functions $K_{ac}^{eff}(T), K_{ca}^{eff}(T)$ considering the boundaries of SRPT (80-90 K) in the case of $TmFeO_3$.

Thus, let us comment on the significance of *d-f* exchange in the context of SRPT. Upon analysing the formula (3.8) governing $\Delta_R(T)$ (see Fig. 3.3(a)), it becomes apparent that in Γ_4 phase there is no *d-f* exchange ($\Delta_R(T) = \Delta_{cf}$) this corresponds to the situation when $G_x = 1$ and $G_z = 0$ (see Fig.3.3(b)). As the system transitions in Γ_{24} phase there appears contribution from the *d-f* exchange and SRPT transition starts with $G_x = \cos\theta$ and $G_z = \sin\theta$, as it follows from Eq. (3.15) during this transition the value of G_z changes from 0 to 1 and vice versa for G_x. By lowering

temperature further to Γ_2 phase when $\Delta_R(T)$ reaches maximum value with $G_z = 1$ and $G_x = 0$.

In the high-temperature orthogonal Γ_4 phase, the anisotropy functions, as shown in Fig.3.3(c), exhibit $K_{ac}^{eff}(T) > 0$ and $K_{ca}^{eff}(T) < 0$. This behaviour corresponds to the scenario where only G_x component is present, and there is no *d-f* exchange (i.e. $\Delta_R(T) = \Delta_{cf}$). As the temperature decreases, a critical temperature point T_1 emerges at which $K_{ac}^{eff}(T_1) = 0$ and $K_{ca}^{eff}(T_1) < 0$ signifying the onset of SRPT. This transition brings the iron spin system into the Γ_{24} intermediate phase with G_x and G_z components. By lowering temperature further to T_2 when $K_{ca}^{eff}(T_2) = 0$ and $K_{ac}^{eff}(T_2) < 0$, spin reorientation is completed and spins system reaches low-temperature Γ_2 phase (with maximum value of $\Delta_R(T)$).

3.3.2. Dynamical equations for the coupled R-Fe subsystems. Resonant frequencies for R^{3+} and Fe^{3+} sub-lattices

Previous theoretical studies [125,173] have identified that in order to investigate the dynamics of the coupled R-Fe subsystems in REOs, it is necessary to construct two sets of equations of motion within a two-sublattice approximation for each of the subsystems.

Utilizing the total thermodynamic potential from equation (3.4), the dynamical equations for the R subsystem take the following form [116,120]:

$$\begin{cases} \left(\frac{\mu_B}{\gamma}\right)\frac{d\vec{f}}{dt} = -\left(\left[\vec{f} \times \frac{\partial \Phi}{\partial \vec{f}}\right] + \left[\vec{c} \times \frac{\partial \Phi}{\partial \vec{c}}\right]\right) + R_{\vec{f}}, \\ \left(\frac{\mu_B}{\gamma}\right)\frac{d\vec{c}}{dt} = -\left(\left[\vec{f} \times \frac{\partial \Phi}{\partial \vec{c}}\right] + \left[\vec{c} \times \frac{\partial \Phi}{\partial \vec{f}}\right]\right) + R_{\vec{c}}. \end{cases} \quad (3.16)$$

In these equations, μ_B is the Bohr magneton and $\gamma = \frac{2\mu_B}{\hbar}$ is the gyromagnetic ratio, and $R_{\vec{f}}$, $R_{\vec{c}}$ are relaxation terms of the AFM [174,175].

For the Fe subsystem, dynamical equations are similar to (3.16) with changing sign for the dynamical part in the equations right-hand side and by changing μ_B to $M_0 = 5\mu_B$.

$$\begin{cases} (\frac{M_0}{\gamma})\frac{d\vec{F}}{dt} = ([\vec{F}\times\frac{\partial\Phi}{\partial\vec{F}}]+[\vec{G}\times\frac{\partial\Phi}{\partial\vec{G}}]) + R_{\vec{F}}, \\ (\frac{M_0}{\gamma})\frac{d\vec{G}}{dt} = ([\vec{F}\times\frac{\partial\Phi}{\partial\vec{G}}]+[\vec{G}\times\frac{\partial\Phi}{\partial\vec{F}}]) + R_{\vec{G}}. \end{cases} \quad (3.17)$$

Here, $R_{\vec{F}}$ and $R_{\vec{G}}$ are relaxation terms with the same meaning for the Fe-subsystem as $R_{\vec{f}}$ and $R_{\vec{c}}$ for the R-subsystem.

Each of these terms contains three dissipation parameters: one – relativistic and two of exchange nature (for details see Appendix B**).** When it comes to the description of antiferromagnetic dynamics there are two distinct dissipative channels: **relativistic** and **exchange** relaxation [176,177]. *Relativistic dissipation constants* are phenomenological parameters that quantify damping due to **spin–orbit** and **spin-lattice** interactions (e.g. **magnetic anisotropy**, **dipole-dipole coupling**). These "relativistic" processes can transfer angular momentum to the lattice, allowing the Néel vector or net magnetisation to lose energy (analogous to Gilbert damping in ferromagnets). In contrast, *exchange dissipation constants* characterise dissipation arising from exchange interactions within the spin system. Exchange-driven dissipation processes conserve total spin but damp the relative motion of sublattice magnetisations, stabilising their mutual orientation. Microscopically, exchange relaxation can be viewed as internal friction mediated by high-frequency exchange modes or two-magnon scattering within the antiferromagnet, whereas relativistic damping stems from weaker spin–orbit coupling (a relativistic effect) and spin-phonon interactions [178].

Rare-earth orthoferrites exemplify how these two dissipation channels lead to multi-stage spin dynamics. Owing to the very large exchange stiffness in iron sublattices, any perturbation triggers a rapid initial relaxation: the sublattice moments quickly realign antiparallel (restoring $\vec{G}$) due to exchange damping ("exchange relaxation") [176]. This fast stage (often on sub-nanosecond or THz time scales) effectively equalises the sublattices and minimises the induced net magnetisation. Subsequently, a slower relaxation stage follows in which the *overall* orientation of the magnetisation/Néel vector approaches equilibrium via relativistic processes (spin–lattice coupling and anisotropy).

3.3.3. Linearisation and fitting

It should be noted that previous studies typically used only $\Phi_{\mathrm{Fe}}(\vec{F},\vec{G})$ to describe frequency behaviour of Fe subsystem. Therefore, we will begin our analysis of the dynamic properties of both the R and Fe subsystems by examining the temperature dependencies of the resonance frequencies. To achieve this, we linearise the two sets of LLG equations (3.16) and (3.17). In the case of the R-subsystem, we got two modes corresponding to the two resonance frequencies ω_f and ω_c. Similarly, for the Fe subsystem, there are also two antiferromagnetic resonance (AFMR) modes known as quasi-ferromagnetic (q-FM) and quasi-antiferromagnetic (q-AFM) and they are well-established in the literature [179–181]. The quasi-FM features the precession of the weak magnetisation vector $\vec{F}$ where the relative angle between the two sublattices remains fixed. On the other hand, the quasi-AFM mode periodically modifies the canting angle, but the $\vec{F}$ remains pointing along its equilibrium orientation, with its amplitude oscillating in time. For the case of $TmFeO_3$ the q-FM mode is denoted as "soft" one, implying that its frequency approaches zero at the transition temperatures T_1 and T_2.

By linearising the system of equations (3.17) (for more details see Appendix C), we got two AFMR frequencies corresponding to q-FM and q-AFM modes, respectively:

$$\omega_{\mathrm{qFM}} = \frac{\gamma}{M_0}\sqrt{H_{\mathrm{ac}}H_{\mathrm{ex}}}, \quad \omega_{\mathrm{qAFM}} = \frac{\gamma}{M_0}\sqrt{H_{\mathrm{ab}}H_{\mathrm{ex}}}. \tag{3.18}$$

Here,

$$H_{ex} = A,\ H_{ac} = \begin{cases} K_{\mathrm{ac}}^{\mathrm{eff}}(T),\ \ T > T_1 \\ 2\,K_2\sqrt{-\frac{K_{\mathrm{ac}}^{\mathrm{eff}}(T)}{K_2}\left[1+\frac{K_{\mathrm{ac}}^{\mathrm{eff}}(T)}{K_2}\right]}, T_2 < T < T_1 \\ \left(-K_2 - K_{\mathrm{ac}}^{\mathrm{eff}}(T)\right), T_2 > T \end{cases}$$

and

$$H_{ab} = \begin{cases} K_{\mathrm{ab}}^{0},\ \ T > T_1 \\ \left(K_{\mathrm{ab}}^{0} + \left[1+\frac{K_{\mathrm{ac}}^{\mathrm{eff}}(T)}{K_2}\right](K_2'' + K_2)\right), T_2 < T < T_1 \\ K_{\mathrm{ab}}^{0} + K_2'' + K_2, T_2 > T \end{cases}$$

H_{ac}, H_{ab} are the anisotropy effective fields, and H_{ex} is the exchange field.

To derive R-frequencies, one has to linearise the system of equations (3.16) (procedure is provided in Appendix C) that yields:

$$\omega_f = \frac{1}{\pi\hbar}\sqrt{\Delta_{cf}^2\left(1-\tanh\left[\frac{\Delta_R}{k_B T}\right]\frac{\lambda_f}{\Delta_R}\right)+\left(bG_z + a\mu_x F_x + \tanh\left[\frac{\Delta_R}{k_B T}\right]\frac{\Delta_{ex}}{\Delta_R}\lambda_f\right)^2},$$
$$\omega_c = \frac{1}{\pi\hbar}\sqrt{\Delta_{cf}^2\left(1-\tanh\left[\frac{\Delta_R}{k_B T}\right]\frac{\lambda_c}{\Delta_R}\right)+\left(bG_z + a\mu_x F_x + \tanh\left[\frac{\Delta_R}{k_B T}\right]\frac{\Delta_{ex}}{\Delta_R}\lambda_f\right)^2}. \quad (3.19)$$

To begin our analysis, we first specify the energy value for the crystal field splitting of the effective two-level transition in Tm^{3+} ion within the multiplet $^3H_6$ (Fig.3.4(a)) as $\Delta_{cf} = 57.6$ K, (40 cm^{-1} or 1.2 THz), based on the data from the reference [182]. It should be noted, however, that reference [80] also indicates that the energy difference between the first and second singlets (depicted in green), which form the lowest transition, is 25.2 K (17.5 cm^{-1} or 0.52 THz). On the other hand, experimental data from reference [52] identifies that the electronic transition responsible for the THz-driven anisotropy torque is at 1.2 THz. Notably, this value corresponds to the transition between the first and third singlets as described in reference [80], both of which are highlighted in red (Fig.3.4(a)). Thus, we assume that this transition contributes to the anisotropy functions and plays the main role in the THz-induced dynamics, hence the chosen value for Δ_{cf}.

Using this value, we performed fitting for the expressions presented in formulas (3.18) and (3.19) to experimental results from [151] (Fig.3.4(b)), with the derived parameters summarized in Table II in Appendix D (we converted the units to SI system, while our original equations are in cgs system).

The fitting results indicate that the rare-earth resonance frequencies are significantly higher (1.17 and 1.22 THz at 85 K), compared to the antiferromagnetic resonance (AFMR) frequencies, which are lower (0.1 and 0.82 THz at 85 K). This substantial frequency separation justifies the use of the adiabatic approximation, suggesting that the resonance frequencies of the R and Fe subsystems do not interact or undergo mode hybridization. This finding aligns with the existing literature, as noted in reference [120].

As one can see for the case of $TmFeO_3$ we managed to precisely reproduce the behaviour of AFMR modes, where q-FM mode experienced softening during the transition from Γ_4 to Γ_{24} and from Γ_{24} to Γ_2 temperature phases. It also should be

pointed out that in $TmFeO_3$, the AFMR mode frequencies are well separated from the R modes, which essentially means that there is no dynamical interaction (which can manifest itself in avoided crossing behaviour like in $HoFeO_3$ or $TbFeO_3$ [120]) between these two types of modes. Finally, our formulas for AFMR modes agree well with previous studies [179–181], and numerical results are in excellent match with the experimental data from [151].

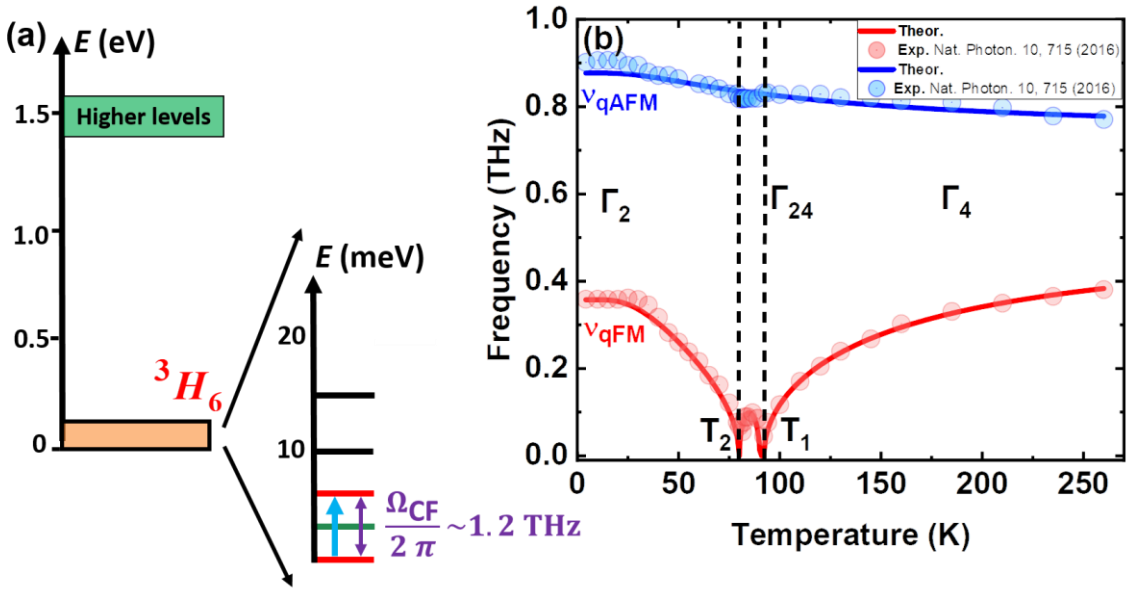

Fig.3.4. (a) Illustration of the energy levels of the Tm^{3+} ion [182] in $TmFeO_3$ along with photon energy of the THz pump pulse (blue arrow) used in experiment [52]. (b) Calculated temperature dependence of the Fe resonance frequencies in $TmFeO_3$ (ν_{qFM} and ν_{qAFM}) shown as solid lines in comparison to the experimental results from [151] shown as circles. The dashed lines indicate phase transitions temperatures.

3.3.4. Modelled dynamics of the R-Fe subsystems

Theoretical estimations in [151] and experimental results in [152] have shown that ultrafast switching of iron spins ($\vec{G}$ vector) by anisotropy-driven torque can be achieved by an external THz pulse in the middle of the temperature interval of Γ_{24} phase for $TmFeO_3$. The Zeeman torque was found to be too weak to induce the switching. Instead, the nonlinear anisotropy-driven torque arising from pumping the rare-earth subsystem was sufficient.

In our model, the anisotropy parameters are renormalised through the R-subsystem, resulting in the temperature-dependent functions (3.10) - (3.13). Additionally, the crystal symmetry group D_{2h}^{16} of REOs allows for a free energy term quadratic with respect to the terahertz electric field $\vec{E}$ and the antiferromagnetic vector $\vec{G}$, which microscopically is the Stark effect term in Eq. (3.2). Therefore, to verify the reliability of our model, we considered three cases. Firstly, we numerically estimated the threshold field required to exert Zeeman torque on the Fe subsystem strong enough to realize its switching. Then we investigated the minimum values of $\vec{H}_{\mathrm{THz}}$ and $\vec{E}_{\mathrm{THz}}$, (i.e. Zeeman and Stark mechanisms), respectively, required to pump the R-subsystem, which in its turn modifies the anisotropy-driven torque, required to achieve spin switching.

Below, we present numerical modelling results for $TmFeO_3$ in the middle of Γ_{24} magnetic phase with T=85 K (Fig.3.5). For the numerical modelling of the dynamical equations (Eq.3.17) for the iron subsystem, we took the thermodynamic potential from (Eq.3.4), and considered a real THz wave-form pulse (Fig.3.5(a)) for the magnetic (H_{THz}) and electric (E_{THz}) field components taken from [52], which we inserted in the components H_x,E_x, and E_y in Eq.3.4.

Our numerical modelling results indicate that the minimum magnetic threshold fields necessary for inducing spin switching via the Zeeman mechanism are 2.35 T for 90° switching and 2.6 T for 180° switching. These threshold values are significantly lower—by an order of magnitude—than those estimated in prior research [151]. For the subsequent scenarios, subjecting the R subsystem to a terahertz magnetic field of H_{THz}=2.7 and 3.1 T, along with E_{THz}=0.9 and 1.0 MV/cm which is equal in values of H_{THz} to 2.7 and 3.0 T, facilitates the alteration of the anisotropy. This, in turn, manifests as a torque on the Fe spins, effectively leading to their switching.

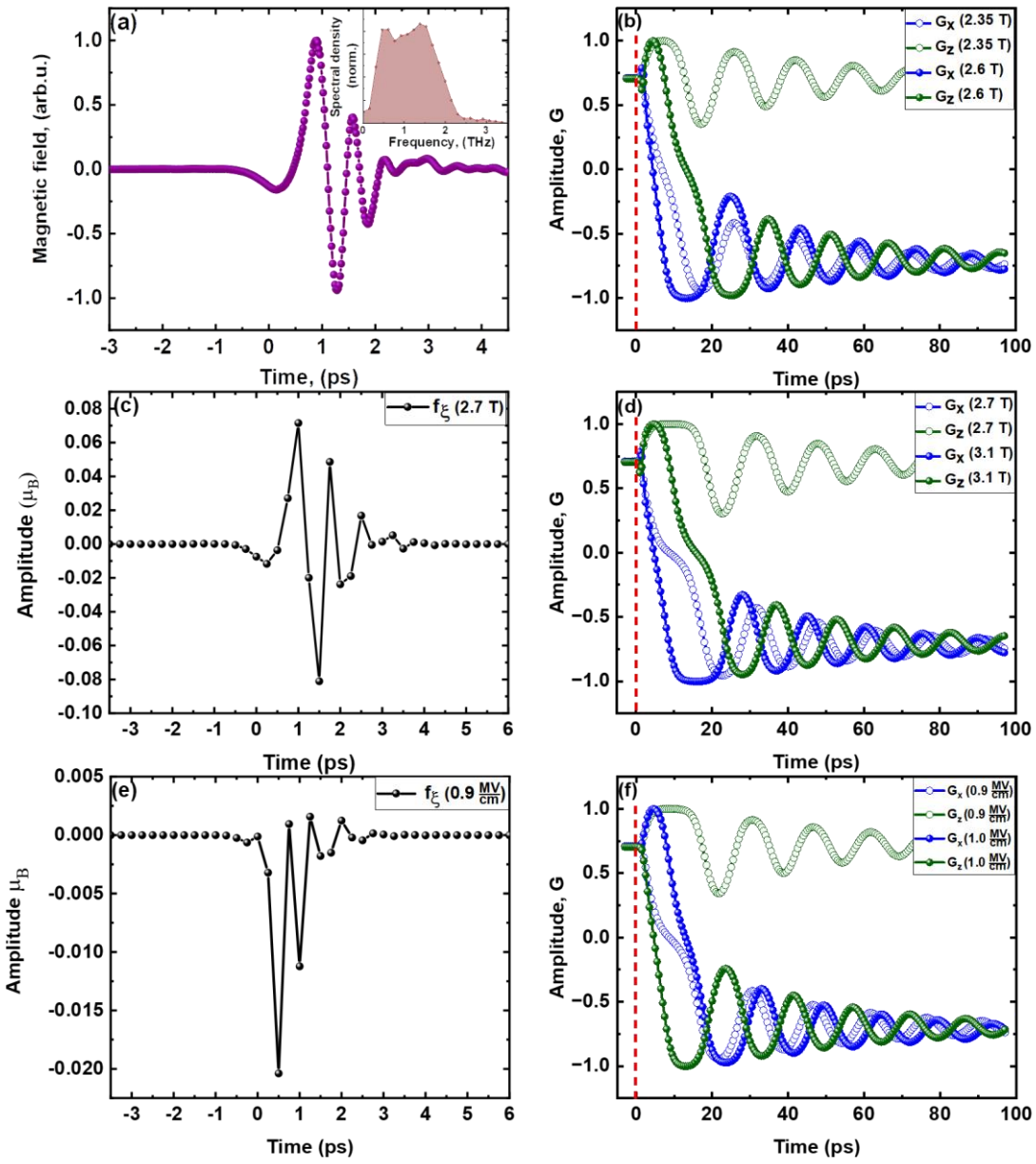

Fig. 3.5. (a) Magnetic field waveform of a THz pulse used in [151]. The corresponding Fourier spectrum is shown in the inset. (b) Illustrates the dynamics of the *G* vector components (G_x, G_z) of Fe spins at *T*=85 K. The red dashed lines mark the beginning of oscillations. Open circles indicate the switching of G vector in the *xz* plane by 90° at H_{THz}=2.35 T, followed by a 180° switching at H_{THz}=2.6 T. (c), (e) Depict the dynamics of f_ξ vector components of Tm^{3+} ions pumped by H_{THz}=2.7 T and E_{THz}=0.9 MV/cm. (d), (f) Show the dynamics of the *G* vector components (G_x, G_z) at *T*=85 K switched by rare-earth anisotropy torque (same curves style as in the case of Pic (b)) on 90° (2.7 T and 0.9 MV/cm) and 180° (3.1 T and 1.0 MV/cm) respectively.

3.3.5. Switching mechanism

In addressing iron spin-switching mechanism within the Γ_{24} magnetic phase, we consider the vector components G_x and G_z. By substituting these components into formula (3.4) and incorporating subsequent equations (3.5) through (3.8), we derive and plot the total thermodynamic potential energy as a function of the angle of iron spins orientation θ (see. Fig. 3.6). Analysis of Fig. 3.6 reveals four distinct minima corresponding to the four orientations of iron spins namely 90°, 180°, 270° and 360°.

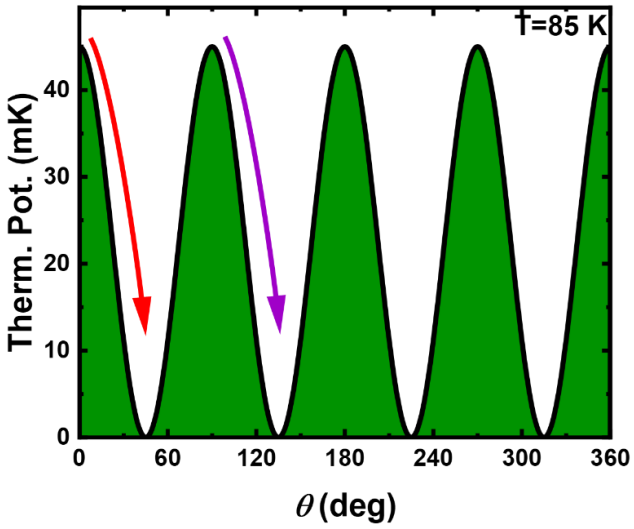

Fig.3.6. Illustration of the total free-energy thermodynamic potential as a function of angle θ(T) in the middle of Γ_{24} temperature phase. The four distinctive minima correspond to the switching of iron spins on 90°, 180°, 270° and 360°, respectively.

Furthermore, as depicted in Fig. 3.6, the application of a terahertz AC magnetic field H_{THz} equal to 2.35 T stimulates 90° rotation of the Fe spins, as indicated by the red solid line. To achieve 180° rotation, one needs to apply the H_{THz} = 2.6 T, which is indicated as a purple solid line. However, if we consider the influence of the rare-earth subsystems as an external driving force on iron spins, the situation becomes more interesting.

As illustrated in Figure 3.5(d), invoking the torque generated by the rare-earth anisotropy via the magnetic field component of the terahertz radiation demands an increased H_{THz} of 2.7 and 3.1 T for 90° and 180° switching of Fe spins, respectively. As can be seen in this case the threshold fields are even slightly higher than in the

case of direct Zeeman mechanism. However, if we consider the Stark effect, which scales quadratically, in this case, the retrieved threshold electric fields $E_{\mathrm{THz}} = 0.9\ \mathrm{MV\ cm^{-1}}$ and $E_{\mathrm{THz}} = 1.0\ \mathrm{MV\ cm^{-1}}$ are enough to pump the R subsystem and to achieve 90° and 180° iron spins switching.

Table 2 shows the indicative minimal threshold fields required for the iron spins switching on 90° in the case of Zeeman mechanism and rare-earth anisotropy-driven torques in all three magnetic phases of $TmFeO_3$. From a theoretical perspective, the Γ_{24} phase, being a phase of lower symmetry, is inherently more susceptible to external perturbations compared to the higher symmetry orthogonal phases, Γ_2 and Γ_4, where the threshold fields are an order of magnitude larger than in Γ_{24}. This differential sensitivity is crucial for understanding the dynamics of Fe spins reorientation under varying external conditions.

Table 2. Values of threshold spin switching fields

T	Zeeman mechanism (T)	Linear Anisotropy (T)	Nonlinear Anisotropy (Stark effect) (MV/cm)
50 K (Γ_2)	13.1	24.6	5.2
85 K(Γ_{24})	2.35	2.7	0.9
120 K (Γ_4)	14.5	27.2	5.6

Let us analyse the dependence between electromagnetic fields required for 90° switching of iron spins and dissipation parameters of iron subsystem. Figure 7 (a, b) shows the interplay between the dissipation parameters $\Lambda_0, \Lambda_\perp$ and $\Lambda_\parallel$ and the threshold fields, H_{THz} and E_{THz}, respectively.

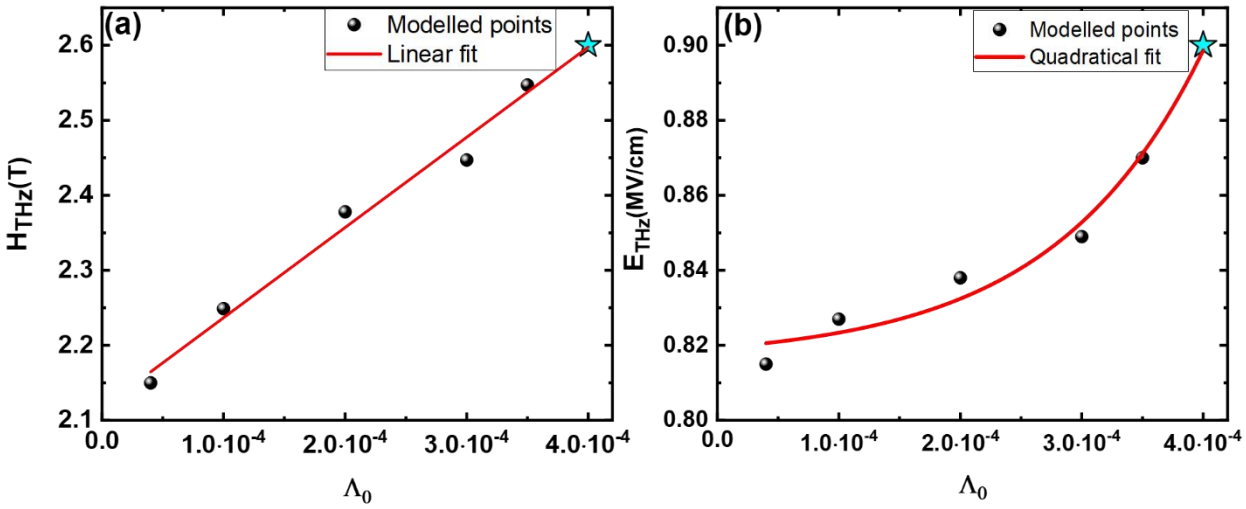

Fig.3.7. (a, b). The magnitude of the threshold AC THz electromagnetic fields required for 90° switching on the dissipation parameters $\Lambda_0, \Lambda_\perp, \Lambda_\parallel$. In the previously examined cases (Fig. 5, b, d, f), we assigned realistic values based on [116,125] to the dissipation parameters as $\Lambda_0 = 4 \times 10^{-4}, \Lambda_\perp = 9.0 \times 10^{-5}, \Lambda_\parallel = 7.0 \times 10^{-5}$ corresponding to the points illustrated as a star on the graphs (for simplicity only the Λ_0 parameter is used for horizontal axis).

One can see from Figure 7 that decreasing the values of dissipation parameters by 25, 50, 75 and 90% relative to the initial value indicated as a "star", leads the different behaviour for the dynamics driven by H_{THz} and E_{THz} components, respectively. This behaviour is due to the fact that in the case of H_{THz} we have the Zeeman effect which is linear in the excitation field and therefore, in the case of consequently decreasing decay parameter by a value of 25% decreases linearly. However, in the case of E_{THz}, we have the Stark effect, which is quadratic and therefore decreases quadratically.

3.3.6. Energy estimation

Let`s estimate the energy dissipation within in the iron spin system driven by Zeeman mechanism. By substituting the parameters delineated in equations (5) through (8) into equation (4) as well as numerical solutions obtained in the case of iron spin switching we calculate the time-evolution of the free energy shown in Fig. 8.

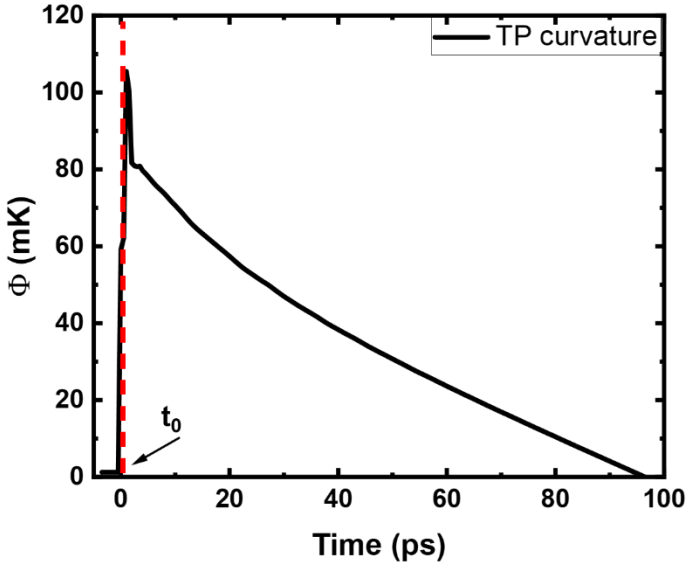

Fig.3.8. Dynamics of total thermodynamic potential curvature as a function of temperature modelled with dynamical solutions from equation (17) in the case of Zeeman switching mechanism (in the cases when rare-earth anisotropy torque is switching force, the corresponding graphs have similar shape), $t_0 = 0$ ps corresponds to the time when components of $\vec{G}$ start to oscillate due to the arrival of the pump pulse; red dashed curve is added to indicate the start of oscillations.

By calculating the difference between $t_0 = 0$ ps and $t_{\text{end}} = 100$ ps, we got that the dissipation of the iron spin system normalised by the number of spins in volume unit in the case of a) Zeeman switching $\Delta\Phi \approx 105$ mK or 9.0 μeV, b) R subsystem as an external torque driven by H_{THz} is 135 mK or 11.6 μeV, and c) in the case of Stark mechanism is 51 mK or 4.4 μeV. This is in a good agreement with the experimental result obtained in [152].

3.4. Conclusions

To summarize, we have formulated a theoretical model based on the microscopic approach to elucidate the magnetic switching of $RFeO_3$ subjected to strong THz excitation. $TmFeO_3$ was chosen as an indicative material due to its well-documented properties and the availability of the experimental data. Initially, to ascertain the model's validity in the equilibrium state, we have deduced the anisotropy functions across all magnetic temperature phases and established the criteria for the spin reorientation phase transitions. Subsequently, we derived and numerically modelled the resonance frequencies of the coupled R-Fe subsystems. Numerical results in the case of AFMR modes are a good match with the experimental data from [151]. Moreover, based on our theoretical model, we performed the numerical simulation of iron spin dynamics under the action of intense THz radiation. We identified the values of threshold fields necessary for inducing spin switching, whether through the Zeeman mechanism or an anisotropy-driven torque, which is modified via the R-subsystem. We estimated the energy dissipations involved in the switching process and found a good agreement with the experimental values from [151].

The present model applies to $RFeO_3$ with non-Kramers ions, in which there is no cross-over between the rare-earth and iron modes so that they can be considered in the adiabatic approximation (like in $TmFeO_3$). The R-Fe adiabatic coupling determines their frequencies behaviour vs temperature, but dynamical interaction between the modes does not play a role. The situation is different in $TbFeO_3$ and $HoFeO_3$, as there are temperatures at which the rare-earth frequencies cross over (i.e. are equal to) the frequencies of the antiferromagnetic resonances. In this case, the dynamical interaction is important and results in avoided crossing between the modes. Future work will, therefore, include extending our theoretical formalism to describe this more sophisticated case. Furthermore, our approach can also be expanded to include the case of Kramers ions, for instance the recently reported THz-driven switching in $SmErFeO_3$ [183], in which the *f-d* interaction leads to more cumbersome thermodynamic potential [124,125]. To conclude, our results are the first major milestone in theoretical understanding THz-driven nonlinear dynamics of coupled Fe spins and rare-earth ions in the orthoferrites with non-Kramers ions.

3.5. Appendix A: Derivation of the equilibrium components for the coupled R-Fe subsystems

Before proceeding to the derivation of equilibrium values F_x, F_z, f_ξ, f_ζ, let us introduce the auxiliary parameters:

$$\sin\psi = \frac{\Delta_{\rm ex}}{\Delta_{\rm R}},\ \cos\psi = \frac{\Delta_{\rm cf}}{\Delta_{\rm R}},\ \Delta_{\rm R} = \sqrt{\Delta_{\rm ex}^2 + \Delta_{\rm cf}^2}\ ,\ f_0 = \tanh[\frac{\Delta_{\rm R}}{k_{\rm B}T}],\ \tilde{T} = \frac{\Delta_{\rm R}}{\tanh[\frac{\Delta_{\rm R}}{k_{\rm B}T}]},$$

$$\Delta\lambda_{\rm f} = \frac{(a\mu_x)^2}{A},\ \Delta_{\rm ex}^0 = b + \frac{ad\mu_x}{A},\ \tilde{\lambda}_{\rm f} = \lambda_{\rm f} + \Delta\lambda_{\rm f},,$$

$$\sqrt{c_\zeta{}^2 + c_\eta{}^2 + c_\xi{}^2 + f_\zeta{}^2 + f_\eta{}^2 + f_\xi{}^2} = f_0 = \tanh[\frac{\Delta_{\rm R}}{k_{\rm B}T}].$$

Here, $\Delta_{\rm ex}$ is the *d-f exchange* interaction energy and all other parameters are the same as in the main text.

By minimizing the thermodynamic potential (3.4) with respect to F_x, F_z, f_ξ and f_ζ, one can derive the corresponding equilibrium values:

$$\frac{\partial\Phi}{\partial F_x} = AF_x - dG_z - af_\xi\mu_x = 0 \Rightarrow F_x = \frac{dG_z + af_\xi\mu_x}{A}, \tag{A.1}$$

$$\frac{\partial\Phi}{\partial F_z} = AF_z + dG_z = 0 \Rightarrow F_z = -\frac{dG_x}{A}, \tag{A.2}$$

$$\begin{aligned}&\frac{\partial\Phi}{\partial f_\zeta} = \frac{1}{4}T\left(\frac{2f_\zeta\ln[1+f_0]}{f_0} - \frac{2f_\zeta\ln[1-f_0]}{f_0}\right) - \Delta_{\rm cf} = 0 \Rightarrow \\ &\Rightarrow T\frac{f_\zeta}{f_0}\operatorname{arc}\tanh[f_0] - \Delta_{\rm cf} = 0 \Rightarrow f_\zeta = \frac{\Delta_{\rm cf}}{\Delta_{\rm R}}\tanh[\frac{\Delta_{\rm R}}{k_{\rm B}T}] = f_0\cos\psi,\end{aligned} \tag{A.3}$$

$$\frac{\partial\Phi}{\partial f_\xi}=\{\frac{1}{4}T\left(\frac{2f_\xi\ln[1+f_0]}{f_0}-\frac{2f_\xi\ln[1-f_0]}{f_0}\right)-bG_z-aF_x\mu_x-f_\xi\lambda_{\mathrm{f}}\}=0$$

$$\Rightarrow\{f_\xi\frac{\Delta_{\mathrm{R}}}{\tanh[\frac{\Delta_{\mathrm{R}}}{k_{\mathrm{B}}T}]}-bG_z-aF_x\mu_x-f_\xi\lambda_{\mathrm{f}}\}=0 \qquad \text{(A.4)}$$

$$\Rightarrow f_\xi=\frac{(-bG_z-aF_x\mu_x)}{\lambda_{\mathrm{f}}-\frac{\Delta_{\mathrm{R}}}{\tanh[\frac{\Delta_{\mathrm{R}}}{k_{\mathrm{B}}T}]}}=\frac{-bG_z-\frac{a\mu_x(dG_z+af_\xi\mu_x)}{A}}{\lambda_{\mathrm{f}}-\frac{\Delta_{\mathrm{R}}}{\tanh[\frac{\Delta_{\mathrm{R}}}{k_{\mathrm{B}}T}]}},$$

Solving equation (A.4) with respect to f_ξ yields:

$$\frac{-bG_z-\frac{a\mu_x(dG_z+af_\xi\mu_x)}{A}}{\lambda_{\mathrm{f}}-\frac{\Delta_{\mathrm{R}}}{\tanh[\frac{\Delta_{\mathrm{R}}}{k_{\mathrm{B}}T}]}}-f_\xi=0\Rightarrow f_\xi=-\frac{G_z(Ab+ad\mu_x)}{A\lambda_{\mathrm{f}}+a^2\mu_x^2-\frac{A\Delta_{\mathrm{R}}}{\tanh[\frac{\Delta_{\mathrm{R}}}{k_{\mathrm{B}}T}]}}\Rightarrow$$

$$\Rightarrow-\frac{G_z(b+\frac{ad\mu_x}{A})}{\lambda_{\mathrm{f}}+\frac{a^2\mu_x^2}{A}-\frac{\Delta_{\mathrm{R}}}{\tanh[\frac{\Delta_{\mathrm{R}}}{k_{\mathrm{B}}T}]}}=\left|\begin{array}{l}\frac{(a\mu_x)^2}{A}=\Delta\lambda_{\mathrm{f}};\ \ \frac{\Delta_{\mathrm{R}}}{\tanh[\frac{\Delta_{\mathrm{R}}}{k_{\mathrm{B}}T}]}=\tilde{T}\\ b+\frac{ad\mu_x}{A}=\Delta_{\mathrm{ex}}^0;\ \tilde{\lambda}_{\mathrm{f}}=\lambda_{\mathrm{f}}+\Delta\lambda_{\mathrm{f}}\end{array}\right|=\frac{G_z\Delta_{\mathrm{ex}}^0}{(\tilde{T}-\tilde{\lambda}_{\mathrm{f}})}.$$

(A.5)

However,

$$f_\xi=\sin\psi\, f_0=\frac{\Delta_{\mathrm{ex}}}{\Delta_{\mathrm{R}}}\tanh[\frac{\Delta_{\mathrm{R}}}{k_{\mathrm{B}}T}]=\frac{\Delta_{\mathrm{ex}}}{\tilde{T}}, \qquad \text{(A.6)}$$

Equating expressions (A.5) and (A.6) and expanding equation in a Taylor series with respect to the small parameter $\tilde{\lambda}_{\mathrm{f}}$, one obtains the following result:

$$\Delta_{\mathrm{ex}}=G_z\Delta_{\mathrm{ex}}^0(1+\frac{\tilde{\lambda}_{\mathrm{f}}}{(1-\tilde{T})}). \qquad \text{(A.7)}$$

3.6. Appendix B: Derivation of the decay functions for the coupled R-Fe subsystems

The non-equilibrium state of the R subsystem is ascribed to the mean values of the Pauli matrices of its *i*-th ion, which is denoted as $\langle\vec{\sigma}_i\rangle = \vec{\sigma}_i$ as for the sake of brevity, we shall omit the averaging symbol hereafter. The dynamical equations governing the behaviour of $\vec{\sigma}_i$ can be obtained by applying the nonequilibrium statistical operator method, as explained in [173] in the following form:

$$\frac{1}{2}\hbar\frac{\partial\vec{\sigma}_i}{\partial t} = -[\vec{\sigma}_i, \frac{\partial\Phi}{\partial\vec{\sigma}_i}] + \vec{R}_i. \tag{B.1}$$

In this context, the function $\Phi(\vec{F}, \vec{G}, \vec{\sigma}_i)$ serves as a thermodynamic potential that characterises the system's nonequilibrium state. As for the relaxation term $\vec{R}_i$ in equation (B.1), it can be described through the approach presented in [65]. Specifically, a simplified expansion of the thermodynamic potential can be employed, yielding the following expression:

$$\vec{R}_i = -\lambda_0(\frac{\partial\Phi}{\partial\vec{\sigma}_i}) - \lambda_\perp[(\vec{\sigma}_i)^2\frac{\partial\Phi}{\partial\vec{\sigma}_i} - \vec{\sigma}_i(\vec{\sigma}_i, \frac{\partial\Phi}{\partial\vec{\sigma}_i})] - \lambda_\parallel\vec{\sigma}_i(\vec{\sigma}_i, \frac{\partial\Phi}{\partial\vec{\sigma}_i}). \tag{B.2}$$

Here, $\lambda_0, \lambda_\perp, \lambda_\parallel$ are the dissipation constants for the R-subsystem. Noteworthy $\lambda_\perp$ has a relativistic nature, and $\lambda_0, \lambda_\parallel$ are exchange constants. At $\lambda_0, \lambda_\parallel = 0$, the equations (16) are similar to the usual Landau-Lifshitz-Gilbert equations.

For the two RE sub-lattices the dynamic part in the equation (B1) will take the next form:

$$-[\vec{\sigma}_i, \frac{\partial\Phi}{\partial\vec{\sigma}_i}]\Big|_{\vec{\sigma}_i=\vec{\sigma}_1,\vec{\sigma}_2} = -[\vec{\sigma}_1, \frac{\partial\Phi}{\partial\vec{\sigma}_1}] - [\vec{\sigma}_2, \frac{\partial\Phi}{\partial\vec{\sigma}_2}]. \tag{B.3}$$

In this regard equation (B.1) can be rewritten as:

$$\begin{cases} \vec{R}_1 = -\lambda_0\frac{\partial\Phi}{\partial\vec{\sigma}_1} - \lambda_\perp[\vec{\sigma}_1^2\frac{\partial\Phi}{\partial\vec{\sigma}_1} - \vec{\sigma}_1(\vec{\sigma}_1, \frac{\partial\Phi}{\partial\vec{\sigma}_1})] - \lambda_\parallel\vec{\sigma}_1(\vec{\sigma}_1, \frac{\partial\Phi}{\partial\vec{\sigma}_2}), \\ \vec{R}_2 = -\lambda_0\frac{\partial\Phi}{\partial\vec{\sigma}_2} - \lambda_\perp[\vec{\sigma}_2^2\frac{\partial\Phi}{\partial\vec{\sigma}_2} - \vec{\sigma}_2(\vec{\sigma}_2, \frac{\partial\Phi}{\partial\vec{\sigma}_2})] - \lambda_\parallel\vec{\sigma}_2(\vec{\sigma}_2, \frac{\partial\Phi}{\partial\vec{\sigma}_2}). \end{cases} \tag{B.4}$$

For a quantum two-level system with an effective spin of 1/2, as described in [171], the rare-earth vectors $\vec{f}$ and $\vec{c}$ can be expressed in terms of the mean values of the Pauli matrices as follows:

$$\begin{cases} \vec{f} = \dfrac{\vec{\sigma}_1 + \vec{\sigma}_2}{2} \\ \vec{c} = \dfrac{\vec{\sigma}_1 - \vec{\sigma}_2}{2} \end{cases} \Rightarrow \begin{cases} \vec{\sigma}_1 = \vec{f} + \vec{c} \\ \vec{\sigma}_2 = \vec{f} - \vec{c} \end{cases} \Rightarrow \begin{cases} \dfrac{\partial \Phi}{\partial \vec{f}} = \dfrac{\partial \Phi}{\partial \vec{\sigma}_1} + \dfrac{\partial \Phi}{\partial \vec{\sigma}_2} \\ \dfrac{\partial \Phi}{\partial \vec{c}} = \dfrac{\partial \Phi}{\partial \vec{\sigma}_1} - \dfrac{\partial \Phi}{\partial \vec{\sigma}_2} \end{cases}. \tag{B.5}$$

Therefore the dissipative terms $\vec{R}_f = \vec{R}_1 + \vec{R}_2$ can be expressed as:

$$\vec{R}_f = -\lambda_0 \left(\frac{\partial \Phi}{\partial \vec{\sigma}_1} + \frac{\partial \Phi}{\partial \vec{\sigma}_2}\right) - \lambda_\perp [(\vec{f} + \vec{c})^2 \frac{\partial \Phi}{\partial \vec{\sigma}_1} + (\vec{f} - \vec{c})^2 \frac{\partial \Phi}{\partial \vec{\sigma}_2} - \{(\vec{f} + \vec{c})((\vec{f} + \vec{c}), \frac{\partial \Phi}{\partial \vec{\sigma}_1})$$
$$+ (\vec{f} - \vec{c})((\vec{f} - \vec{c}) \frac{\partial \Phi}{\partial \vec{\sigma}_2}\}] - \lambda_{\|} [((\vec{f} + \vec{c})((\vec{f} + \vec{c}), \frac{\partial \Phi}{\partial \vec{\sigma}_1}) + (\vec{f} - \vec{c})((\vec{f} - \vec{c}), \frac{\partial \Phi}{\partial \vec{\sigma}_2})];$$

Finally, the resulting expression is:

$$\vec{R}_f = -\lambda_0 \frac{\partial \Phi}{\partial \vec{f}} - (\lambda_{\|} - \lambda_\perp)\{\vec{f}(\vec{f}, \frac{\partial \Phi}{\partial \vec{f}}) + \vec{f}(\vec{c}, \frac{\partial \Phi}{\partial \vec{c}}) + \vec{c}(\vec{f}, \frac{\partial \Phi}{\partial \vec{c}}) + \vec{c}(\vec{c}, \frac{\partial \Phi}{\partial \vec{f}})\} -$$
$$-\lambda_\perp \{(\vec{f}^2 + \vec{c}^2) \frac{\partial \Phi}{\partial \vec{f}} + 2(\vec{f}, \vec{c}) \frac{\partial \Phi}{\partial \vec{c}}\}. \tag{B.6}$$

Considering the conditions on the vectors $\vec{f}$ and $\vec{c}$: $(\vec{f}\vec{c}) = 0,\ \vec{f}^2 + \vec{c}^2 = f_0^2 = \tanh^2[\frac{\Delta_R}{k_B T}]$, it is possible to derive the following result:

$$\vec{R}_f = -\lambda_0 \frac{\partial \Phi}{\partial \vec{f}} - (\lambda_{\|} - \lambda_\perp)\{\vec{f}(\vec{f}, \frac{\partial \Phi}{\partial \vec{f}}) + \vec{f}(\vec{c}, \frac{\partial \Phi}{\partial \vec{c}}) + \vec{c}(\vec{f}, \frac{\partial \Phi}{\partial \vec{c}}) + \vec{c}(\vec{c}, \frac{\partial \Phi}{\partial \vec{f}})\} -$$
$$-\lambda_\perp \tanh^2[\frac{\Delta_R}{k_B T}] \frac{\partial \Phi}{\partial \vec{f}}. \tag{B.7}$$

The same approach as before can be used to obtain the term $\vec{R}_c = \vec{R}_1 - \vec{R}_2$. The final result can be expressed as:

$$\vec{R}_c = -\lambda_0 \frac{\partial \Phi}{\partial \vec{c}} - (\lambda_{\|} - \lambda_\perp)\{\vec{f}(\vec{f}, \frac{\partial \Phi}{\partial \vec{c}}) + \vec{f}(\vec{c}, \frac{\partial \Phi}{\partial \vec{f}}) + \vec{c}(\vec{f}, \frac{\partial \Phi}{\partial \vec{f}}) + \vec{c}(\vec{c}, \frac{\partial \Phi}{\partial \vec{c}})\} -$$
$$-\lambda_\perp \tanh^2[\frac{\Delta_R}{k_B T}] \frac{\partial \Phi}{\partial \vec{c}}. \tag{B.8}$$

The method used to derive equations of motion for the Fe subsystem is similar to that used for the R subsystem. However, instead of the Pauli matrices $\vec{\sigma}_i$, the sublattice magnetisation functions $\vec{m}_i$ must be employed.

$$\frac{1}{2}\hbar\frac{\partial\vec{m}_i}{\partial t}=[\vec{m}_i,\frac{\partial\Phi}{\partial\vec{m}_i}]+\vec{R}_i'. \tag{B.9}$$

Employing a two-sublattice approximation for the dynamic part in the equation (B9):

$$[\vec{m}_i,\frac{\partial\Phi}{\partial\vec{m}_i}]\Big|_{\vec{m}_i=\vec{m}_1,\vec{m}_2}=[\vec{m}_1,\frac{\partial\Phi}{\partial\vec{m}_1}]+[\vec{m}_2,\frac{\partial\Phi}{\partial\vec{m}_2}]. \tag{B.10}$$

With relaxation term as

$$\vec{R}_i'=-\Lambda_0\frac{\partial\Phi}{\partial\vec{m}_i}-\Lambda_\perp[(\vec{m}_i)^2\frac{\partial\Phi}{\partial\vec{m}_i}-\vec{m}_i(\vec{m}_i,\frac{\partial\Phi}{\partial\vec{m}_i})]-\Lambda_{||}\vec{m}_i(\vec{m}_i\frac{\partial\Phi}{\partial\vec{m}_i}). \tag{B.11}$$

Here, $\Lambda_0,\Lambda_\perp,\Lambda_\parallel$ are the dissipation constants with the same meaning for the Fe-subsystem as $\lambda_0,\lambda_\perp,\lambda_\parallel$ for the R-subsystem.

By following the same approach, the resulting expression for the term $\vec{R}_F$ and $\vec{R}_G$ can be expressed as follows:

$$\vec{R}_F=\frac{1}{2M_0}(-\Lambda_0\frac{\partial\Phi}{\partial\vec{F}}-\Lambda_\perp\frac{\partial\Phi}{\partial\vec{F}}-(\Lambda_{||}-\Lambda_\perp)[\vec{F}(\vec{F},\frac{\partial\Phi}{\partial\vec{F}})+\vec{F}(\vec{G},\frac{\partial\Phi}{\partial\vec{G}})+\vec{G}(\vec{F},\frac{\partial\Phi}{\partial\vec{G}})+\vec{G}(\vec{G},\frac{\partial\Phi}{\partial\vec{F}})]), \tag{B.12}$$

$$\vec{R}_G=\frac{1}{2M_0}(-\Lambda_0\frac{\partial\Phi}{\partial\vec{G}}-\Lambda_\perp\frac{\partial\Phi}{\partial\vec{G}}-(\Lambda_{||}-\Lambda_\perp)[\vec{F}(\vec{F},\frac{\partial\Phi}{\partial\vec{G}})+\vec{F}(\vec{G},\frac{\partial\Phi}{\partial\vec{F}})+\vec{G}(\vec{F},\frac{\partial\Phi}{\partial\vec{F}})+\vec{G}(\vec{G},\frac{\partial\Phi}{\partial\vec{G}})]). \tag{B.13}$$

3.7. Appendix C: Derivation of resonance frequencies for coupled R-Fe subsystems

In the Γ_{24} phase, the components of the vectors $\vec{F}$ and $\vec{G}$ can be expressed as the sum of their equilibrium and time-varying components as follows: $F_x(t)\rightarrow\frac{d}{A}G_{z0}+f_x(\mathrm{t}), F_y(t)\rightarrow f_y(\mathrm{t}), F_z(t)\rightarrow f_z(\mathrm{t}), G_x(t)\rightarrow G_{x0}+g_x(t),\ G_y(t)\rightarrow g_y(t),$ $G_z(t)\rightarrow G_{z0}+g_z(\mathrm{t})$.

Through such a transformation, a linearised system of equations can be derived that describes the quasi-ferromagnetic resonance, as shown in the systems of equations (C.1).

$$\begin{cases} \dfrac{df_y(t)}{dt} = \gamma g_x(t)\left(\dfrac{d^2}{A} - K_{ac}^{\text{eff}}\cos^2\theta - K_2\cos^4\theta\right), \\ \dfrac{df_z(t)}{dt} = \gamma df_y(t), \\ \dfrac{dg_x(t)}{dt} = \gamma f_y(t)\left(A - \dfrac{d^2}{A} + K_{ac}^{\text{eff}}\cos^2\theta + K_2\cos^4\theta\right). \end{cases} \quad \text{(C.1)}$$

This system indicates that the behaviour of $f_y(t)$ adheres to a harmonic oscillator model, detailed in equation (C.2):

$$\frac{d^2 f_y(t)}{dt^2} + f_y(t)\omega_{\text{qFM}}^2 = 0, \quad \text{(C.2)}$$

In this context, $\omega_{\text{qFM}} \approx \frac{\gamma}{M_0}\sqrt{H_{\text{ex}}H_{\text{ac}}}$ represents a quasi-ferromagnetic frequency mode, while $H_{\text{ex}} = \frac{1}{2}A$, and $H_{ac} = \begin{cases} K_{\text{ac}}^{\text{eff}}(T), & T > T_1 \\ 2K_2\sqrt{-\frac{K_{\text{ac}}^{\text{eff}}(T)}{K_2}\left[1 + \frac{K_{\text{ac}}^{\text{eff}}(T)}{K_2}\right]}, & T_2 < T < T_1 \\ \left(-K_2 - K_{\text{ac}}^{\text{eff}}(T)\right), & T_2 > T \end{cases}$ are anisotropy and exchange fields, respectively.

To analyse quasi-antiferromagnetic resonance, a similar procedure is applied, resulting in the system (C.3):

$$\begin{cases} \dfrac{df_x(t)}{dt} = \gamma g_y(t)(-K_{ab}^0 - \dfrac{d^2}{A} + \cos^2\theta(K_{ac}^0 + K_2 + K_2\cos^2\theta)), \\ \dfrac{dg_y(t)}{dt} = \gamma((\dfrac{d^3}{A^2} - \dfrac{d}{A}\cos^2\theta(K_{ac}^0 + K_2\cos^2\theta)) + g_z(t)(-d - \dfrac{d}{A}\cos^2\theta(K_{ac}^0 + 3K_2))) + \\ + f_x(t)(A + \dfrac{2d^2}{A} - \cos^2\theta(K_{ac}^0 + K_2\cos^2\theta)), \\ \dfrac{dg_z(t)}{dt} = \gamma g_y(t)\dfrac{d}{A}(K_{ab}^0 + K_2''\cos^2\theta). \end{cases} \tag{C.3}$$

This system provides the equation of motion for $g_y(t)$ as a harmonic oscillator, as expressed in equation (C.4):

$$\frac{d^2 g_y(t)}{dt^2} + g_y(t)\omega_{\text{qAFM}}^2 = 0, \tag{C.4}$$

Here, $\omega_{\text{qAFM}} \approx \frac{\gamma}{M_0}\sqrt{H_{\text{ex}}H_{\text{ab}}}$ denotes the quasi-antiferromagnetic frequency mode, $H_{\text{ex}} = A$ and

$$H_{ab} = \begin{cases} K_{\text{ab}}^0, \quad T > T_1 \\ (K_{\text{ab}}^0 + \left[1 + \dfrac{K_{\text{ac}}^{\text{eff}}(T)}{K_2}\right](K_2'' + K_2)), T_2 < T < T_1 \\ K_{\text{ab}}^0 + K_2'' + K_2, T_2 > T \end{cases}$$

represents the corresponding exchange and anisotropy fields.

The resonant frequencies for the rare-earth subsystem can be obtained using the same linearisation procedure, with adjustments made to account that:

$$f_\xi(t) \to f_{\xi 0} + \delta f_\xi(t), f_\eta(t) \to \delta f_\eta(t), f_\zeta(t) \to f_{\zeta 0} + \delta f_\zeta(t), c_\xi(t) \to \delta c_\xi(t),$$
$$c_\eta(t) \to \delta c_\eta(t), c_\zeta(t) \to \delta c_\zeta(t).$$

The resulting system of equations is (C.5):

$$\begin{cases} \dfrac{d(\delta f_\xi(t))}{dt} = \dfrac{2}{\hbar}\delta f_\eta(t)\Delta_{\mathrm{cf}}, \\ \dfrac{d(\delta f_\eta(t))}{dt} = \dfrac{2}{\hbar}(f_{\zeta 0} bG_z - f_{\xi 0}\Delta_{\mathrm{cf}} + f_{\xi 0} f_{\zeta 0}\lambda_{\mathrm{f}} + aF_x f_{\zeta 0}\mu_x \\ +\delta f_\zeta(t)(bG_z + f_{\xi 0}\lambda_{\mathrm{f}} + aF_x\mu_x) + \delta f_\xi(t)(-\Delta_{\mathrm{cf}} + f_{\zeta 0}\lambda_{\mathrm{f}})), \\ \dfrac{d(\delta f_\zeta(t))}{dt} = \dfrac{2}{\hbar}\delta f_\eta(t)(-bG_z - f_{\xi 0}\lambda_{\mathrm{f}} - aF_x\mu_x). \end{cases} \tag{C.5}$$

The equation of motion (C.6) for $\delta f_\eta(\mathrm{t})$ is derived from the system (C.5), taking on the structure of a harmonic oscillator equation:

$$\frac{d^2(\delta f_\eta(t))}{dt^2} + \delta f_\eta(t)\omega_{\mathrm{f}}^2 = 0, \tag{C.6}$$

Here,

$$\omega_{\mathrm{f}} = \frac{2}{\hbar}\sqrt{\Delta_{\mathrm{cf}}^2(1-\tanh[\frac{\Delta_{\mathrm{R}}}{k_{\mathrm{B}}T}]\frac{\lambda_{\mathrm{f}}}{\Delta_{\mathrm{R}}}) + (bG_z + aF_x\mu_x + \tanh[\frac{\Delta_{\mathrm{R}}}{k_{\mathrm{B}}T}]\frac{\Delta_{\mathrm{ex}}}{\Delta_{\mathrm{R}}}\lambda_{\mathrm{f}})^2}$$

ω_{f} is the 1st RE resonance mode.

Similarly, one could get the system (C.7):

$$\begin{cases} \dfrac{d(\delta c_\xi(t))}{dt} = \dfrac{2}{\hbar}(\delta c_\eta(t)\Delta_{\mathrm{cf}}), \\ \dfrac{d(\delta c_\eta(t))}{dt} = \dfrac{2}{\hbar}(\delta c_\zeta(t) bG_z - \delta c_\zeta(t) f_{\xi 0}\lambda_{\mathrm{f}} + \delta c_\zeta(t) aF_x\mu_x - \delta c_\zeta(t)\Delta_{\mathrm{cf}} + \delta c_\xi(t) f_{\zeta 0}\lambda_{\mathrm{c}}, \\ \dfrac{d(\delta c_\zeta(t))}{dt} = \dfrac{2}{\hbar}\delta c_\eta(t)(-b - f_{\xi 0}\lambda_{\mathrm{f}} - aF_x\mu_x). \end{cases} \tag{C.7}$$

System (C.7) results in an equation of motion for $\delta c_\eta(\mathrm{t})$ that adopts the form of a harmonic oscillator equation:

$$\frac{d^2(\delta c_\eta(t))}{dt^2} + \delta c_\eta(t)\omega_{\mathrm{c}}^2 = 0, \tag{C.8}$$

Here,

$$\omega_{\mathrm{c}} = \frac{2}{\hbar}\sqrt{\Delta_{\mathrm{cf}}^2(1-\tanh[\frac{\Delta_{\mathrm{R}}}{k_{\mathrm{B}}T}]\frac{\lambda_{\mathrm{c}}}{\Delta_{\mathrm{R}}}) + (bG_z + aF_x\mu_x + \tanh[\frac{\Delta_{\mathrm{R}}}{k_{\mathrm{B}}T}]\frac{\Delta_{\mathrm{ex}}}{\Delta_{\mathrm{R}}}\lambda_{\mathrm{f}})^2}$$

The frequency ω_{c} is recognized as the 2nd RE resonance mode.

3.8. Appendix D: Parameters of magnetic interactions in $TmFeO_3$

In this section, we provide the table with relevant parameters from the results of fitting and taken from the corresponding literature [182].

Table II Numerical values for the corresponding parameters in $TmFeO_3$

Param.	Values	Units	Param.	Values	Units	Param.	Values	Units
A	1947.22	K	K_2'	-0.12	K	μ_{y}	$7.2\mu_{\mathrm{B}}$	JT^{-1}
d	98.12	K	K_2''	-0.87	K	a	10.48	T
K_{ac}^0	0.90	K	Δ_{cf}	57.6	K	b	6.5	K
K_{ab}^0	1.05	K	α	$2.24\cdot10^{-8}$	$\frac{\mathrm{cm}^{-3}\mathrm{K}}{\mathrm{J}}$	λ_f	-13.14	K
K_2	0.03	K	μ_{x}	$2.61\mu_{\mathrm{B}}$	JT^{-1}	λ_c	-9.87	K

Chapter IV. THz spin dynamics of Fe and Tb subsystems in $TbFeO_3$

THz-frequency signatures of exchange interactions between iron magnons and electronic transitions in R ions during the spin-reorientation phase transition (SRPT) in the $RFeO_3$ orthoferrites have led to experimental observations of cooperative phenomena such as the ultrastrong coupling (USC) regime and Dicke cooperativity in orthoferrites containing Kramers ions, such as Erbium orthoferrite ($ErFeO_3$) [130–133]. However, some similar magnetic systems such as rare-earth zircons ($DyVO_4$, $TmVO_4$, $TbVO_4$) exhibit another fundamental phenomenon known as the cooperative Jahn-Teller effect [82,185]. In this chapter, we show that in Terbium orthoferrite ($TbFeO_3$), the magnetic analogue of the cooperative Jahn-Teller effect provides a valuable platform for understanding the characteristics of spin-reorientation phase transitions due to the strong coupling between the Fe and Tb subsystems.

4.1. Motivation

In 1937, Jahn and Teller, while studying polyatomic molecules, formulated a very important theorem [186]. They stated that "all nuclear configurations, except for linear ones, are unstable when the electronic state is degenerate with respect to orbital momentum". A direct consequence of the Jahn-Teller theorem is the absence of orbital degeneracy in the ground state of a non-linear molecule. This theorem is generally applicable only to non-Kramers ions in a crystal. Jahn and Teller also noted that molecules possessing an odd number of electrons consistently display a twofold spin degeneracy, that remains intact in any electric field and does not contribute to molecular configuration instability. Initially focused on molecules, Jahn and Teller's research is fully applicable to magnetic crystals as well.

In this chapter, we present our experimental studies on THz-induced spin dynamics in Terbium orthoferrite ($TbFeO_3$), which display characteristics of the magnetic phase transition of the Jahn-Teller type manifesting itself in SRPT of Fe spins influenced by Tb subsystem with a close frequency. We complement our experimental findings with theoretical model, which we developed to explain the features of SRPT in $TbFeO_3$. In the previous chapter, we used a two-level approximation to introduce the R subsystem, considering the lowest-energy quasi-doublet, which helped us to obtain a thermodynamic potential that takes into account all interactions between the Fe and Tb subsystems in the case of $TmFeO_3$. However, in that case the strong-coupling between Fe and Tm ions is absent due to the big gap

in their resonance frequencies which justified the use of adiabatic approximation. In the case of orthoferrites (like $TbFeO_3$), where the lowest-lying energy doublet is split due to a strong coupling between the Fe and Tb subsystems with similar frequencies, this approximation is no longer valid. From theoretical perspective, this actually means that to accurately describe the dynamic behaviour of AFMR and R modes upon solving equations of motion one needs to take into account strong dynamic coupling between Fe and Tb subsystems and to obtain general analytical solutions.

4.2. Magnetic properties of $TbFeO_3$

Let us revisit some of the magnetic properties of Terbium orthoferrite. Like in other orthoferrites, $TbFeO_3$ exhibits an orthorhombic perovskite structure and is categorized under the $D_{2h}^{16}(P_{bnm})$ space group, containing four $TbFeO_3$ molecules per unit cell. The interaction between Fe^{3+} ions leads to an antiferromagnetic (AFM) configuration within the Fe subsystem at a Neel transition temperature of $T_N \approx 650$ K [101]. This configuration, identified as $\Gamma_4(G_x, F_z)$, demonstrates *G*-type antiferromagnetic order along the a(x) axis due to negative symmetric super exchange interactions, and *F*-type ferromagnetic canting along the *c* axis resulting from antisymmetric Fe^{3+}-Fe^{3+} super-exchange (Dzyaloshinskii-Moriya) interactions.

Regarding the temperature-dependent behaviour of magnon antiferromagnetic resonance modes q-FM and q-AFM (AFMR) in $TbFeO_3$, at room temperature these modes display resonance frequencies of 0.32 and 0.53 THz, respectively [120]. As the temperature decreases, both modes gradually increase in frequency, with the q-FM mode reaching a plateau of approximately 0.5 THz at 40 K and the q-AFM mode continuing to rise to 0.66 THz at lower temperatures [187]. Moreover, in contrast to other orthoferrites like $TmFeO_3$ and $ErFeO_3$, where the q-FM mode is typically soft, $TbFeO_3$ exhibits a qualitatively different behaviour. This is attributed to the presence of a low-lying soft Tb mode that interacts with the q-FM mode, preventing its softening [120].

At $T > 4\ K$, the Tb subsystem remains paramagnetic, polarised along two Ising axes within the *ab* plane at an angle $\alpha = \pm 36°$ from *a* axis, influenced by the Fe-Tb interactions as the antiferromagnetic vector $\vec{G}$ of Fe spins exit the *ab* plane [108]. This condition initiates a two spin-reorientation phase transitions, 1st starting at $T_{SR1} \approx 9\ K$, where Fe spins begin a continuous rotation within the *ac* plane, transforming their configuration from Γ_4 to Γ_2 at $T_{SR2} \approx 5.5\ K$. At the same time, the Tb magnetic moments align within the *ab* plane as per the Γ_2 configuration [188]. With a further decrease in temperature, the interaction among Tb moments induces their antiferromagnetic ordering [189]. Studies [108,190] indicate this transition progresses through two phases: initially, at $T_N^{Tb} = 3.3$ K, Tb

moments form the intermediate $\Gamma_{82}(f_\xi c_\eta)$ rare-earth temperature phase. This leads to the occurrence of a 3rd SRPT for Fe spins at $T_{SR2} \approx 3.1$ K, transitioning them from Γ_2 to Γ_4, while Tb spins reorient into a strictly antiferromagnetic Γ_8 phase.

4.3. Selection rules for AFMR modes in $RFeO_3$

Before we proceed with the discussion of our experimental results on THz-induced spin dynamics in $TbFeO_3$ it is also important to mention the *selection rules* for the excitation of AFMR magnon modes (q-FM and q-AFM) in $RFeO_3$. These magnon modes can be selectively excited by THz radiation and respond linearly due to magneto-dipolar interaction. The activation of these modes is driven by a Zeeman torque mechanism. The selection rules for these excitations can be briefly described as follows: q-FM modes are excited when the magnetic field component of the THz radiation is perpendicular to the net magnetisation vector ($\vec{H}_{\mathrm{THz}} \perp \vec{F}$) and q-AFM modes is excited when it is parallel ($\vec{H}_{\mathrm{THz}} \parallel \vec{F}$).

The Fig 4.1. illustrates the AFMR magnon modes polarisation selection rules in $RFeO_3$. As can be seen these rules are influenced by the alignment of the THz field's polarisation with respect to the major crystallographic axes.

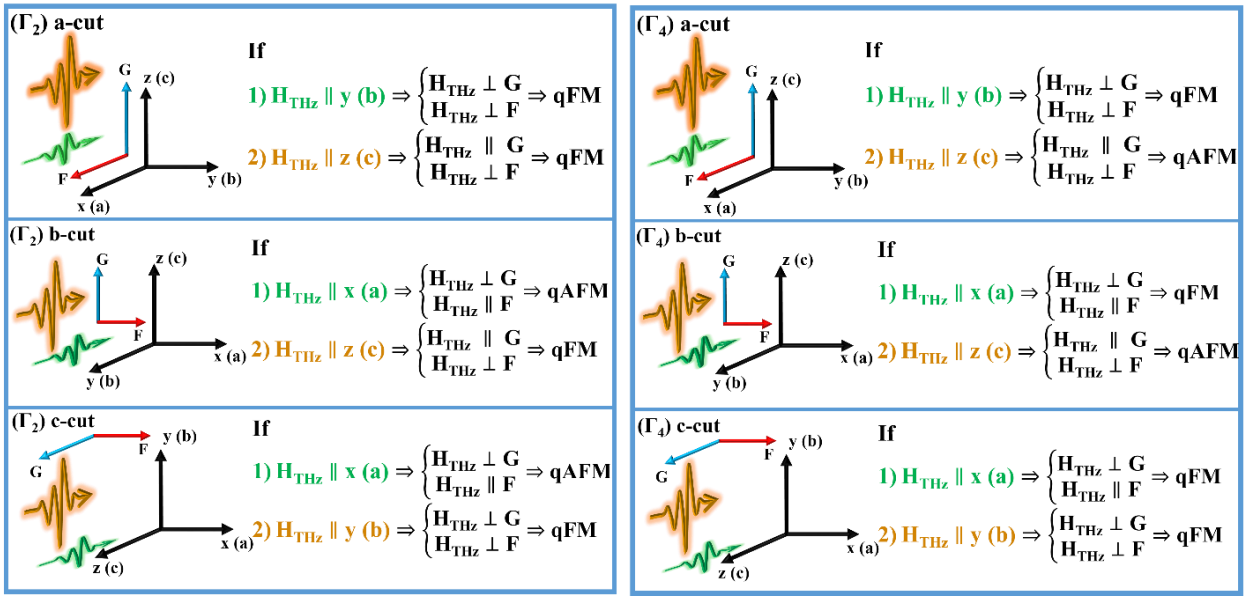

Fig. 4.1. Illustration of six possible configurations for F and G vectors in Γ_2 and Γ_4 temperature phases. The yellow (pointed vertically) and green (pointed horizontally) components of H_{THz} indicate the excitation of q-FM or q-AFM with respect to $\vec{F}$ and $\vec{G}$ vectors, according to the magnon polarisation selection rules.

4.4. Experimental setup

In our experiment (see the sketch in Fig. 4.2 (a)), we investigate the spin dynamics in $TbFeO_3$ by using intense THz pulses (electric field value up to 1 MV/cm see Fig. 4.2 (b)) generated by optical rectification in $LiNbO_3$ and focused onto the sample through a series of three parabolic mirrors. We detect the spin dynamics by measuring the Faraday rotation of time-delayed probe pulses, using a Wollaston prism and a pair of balanced photodetectors, as described in more detail in Chapter 2. The samples were placed in a closed-cycle helium cryostat, which allowed us to control the temperature of the samples and reach it down to 3.5 K, and an external magnetic bias field was applied.

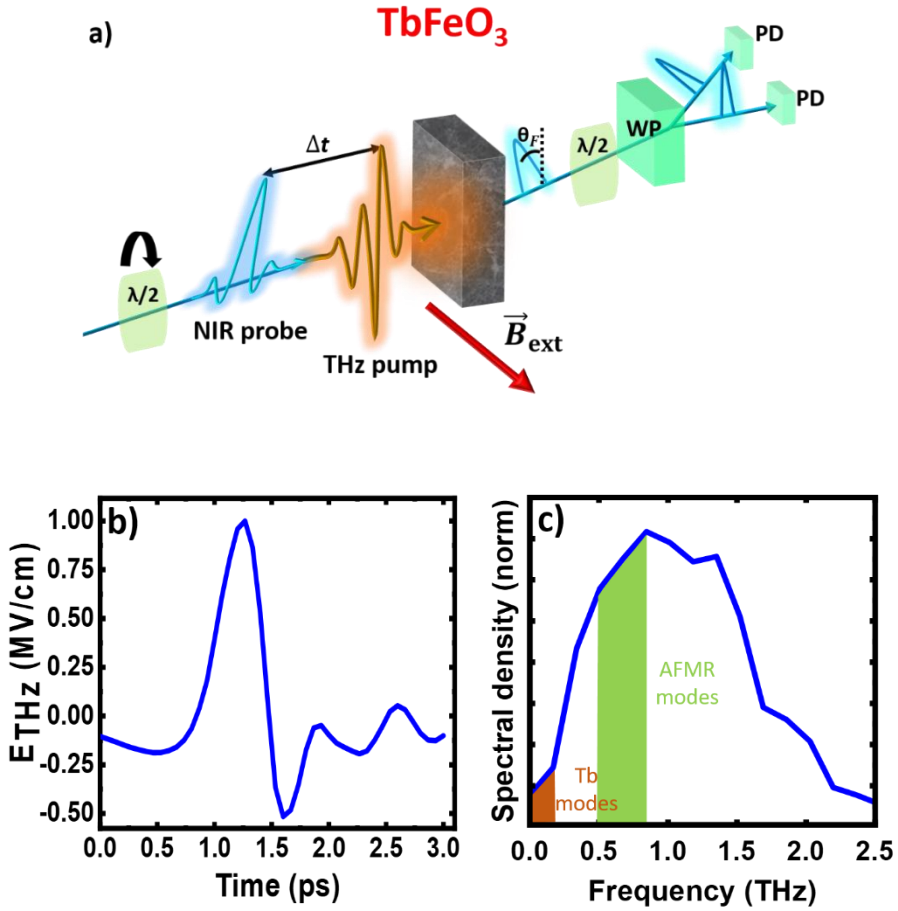

Fig.4.2. a) Schematic of the experiment. The THz pump (orange) and near-infrared probe (wavelength 800 nm) pulses (NIR, cyan) are collinearly focused onto the $TbFeO_3$ sample with a variable delay time *t*. Polarisation control of the NIR probe pulses has been done by using λ/2 plate. Wollaston prism (WP) and two balanced photodiodes (PDs), respectively. b) Time domain waveform of THz pump pulse with its spectrum c) covering frequency ranges of Tb and AFMR modes.

We used a pair of wire-grid polarisers to control the THz fluence, and such combination allows us to perform control over the polarisation of the THz pulses.

4.5. THz-induced spin dynamics in $TbFeO_3$

In this section, we present our experimental results from THz pump-optical probe measurements on Terbium orthoferrite ($TbFeO_3$) using *a*-cut and *b*-cut samples, each with a thickness of 61 micrometers. Our experimental setup includes a set of two wire grids, which direct the magnetic field component of the THz pulse along the *b* or *c* axis for the *a*-cut samples and along the *a* or *c* axis for the *b*-cut samples.

Figure 4.3 shows our findings on the *a*-cut sample, positioned in a closed-cycle cryostat. In this setup, the *c* axis is oriented vertically, with a static external magnetic field applied along the *b* axis ($H_{ext}||b$) and the THz field applied along the *c* axis ($H_{THz}||c$), with a probe pulse angled at 67.5° relative to the *c* axis. Temperature measurements spanned the temperature spin reorientational path from Γ_4 to Γ_2, with a spin reorientational phase transition (SRPT) occurring from 6.8 (Γ_4) to 5.5 (Γ_2) K. Figure 4.3(a) displays the temperature-dependent oscillations of Fe spins driven by THz radiation, with the highest amplitude of oscillations during the SRPT in the intermediate Γ_{24} phase. Figure 4.3(b) shows the corresponding Fourier spectra derived from Figure 4.3(a), identifying two distinct resonance frequencies corresponding to the q-AFM mode in Γ_4 and Γ_2, and the q-FM mode in Γ_{24} phase, consistent with the selection rules for AFMR modes. Figures 4.3 (c) and (d) present Fourier map plots extracted from data in (b). Figure 4.3(d) details the SRPT pathway occurring due to the increasing cumulative effects of *d-f* exchange, crystal field splitting and thermal population, which begin to compete with magnetocrystalline anisotropy, leading to the two SRPT (Γ_4 to Γ_{24} and Γ_{24} to Γ_2). This physical mechanism will be discussed in more detail in subsequent sections. Figure 4.3 (c) illustrates the occurrence of the 3rd SRPT for iron spins from Γ_2 to Γ_4 caused by the ordering of Tb^{3+} ions.

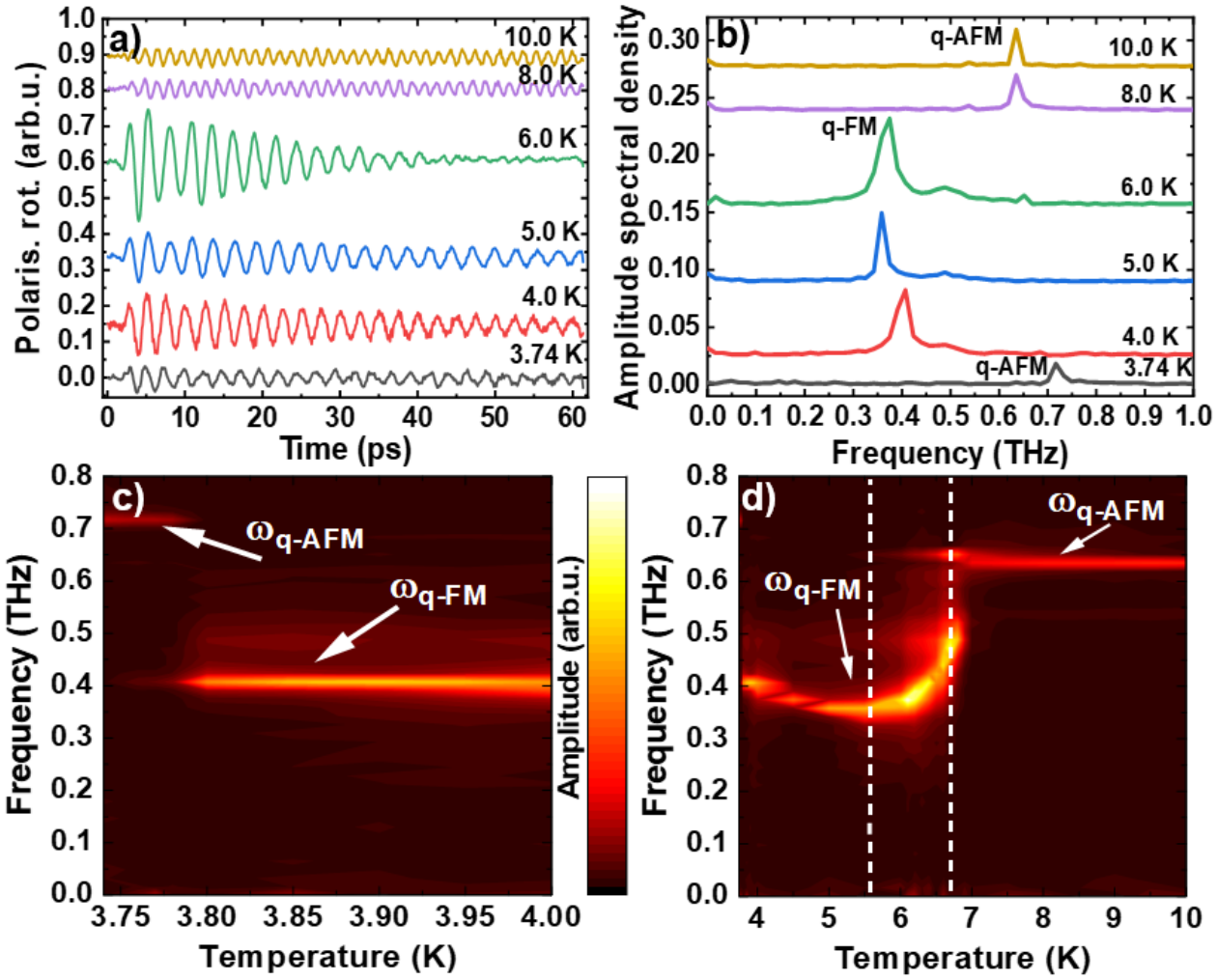

Fig.4.3. (a) shows the time-domain signal as a function of temperature for THz-driven spin dynamics in *a*-cut sample. (b) presents the corresponding Fourier spectrum of the time-domain data from (a)**.** (c, d) are Fourier map plots derived from data in (b)**;** (c) highlights the narrow temperature range (3.8-3.75 K) where ordering of Tb^{3+} ions is observed; (d) illustrates the temperature range (between dotted lines) where the two SRPTs from Γ_4 to Γ_2 occurs.

Figure 4.4. shows results of THz pump-optical probe polarisation measurements for the *b*-cut sample positioned in a cryostat. In this setup, the *c*-axis is horizontal, with a static external magnetic field applied along the *a*-axis ($H_{ext}||a$), while the THz field is directed along the *c*-axis ($H_{THz}||c$), and the probe pulse polarisation is aligned along the *a*-axis.

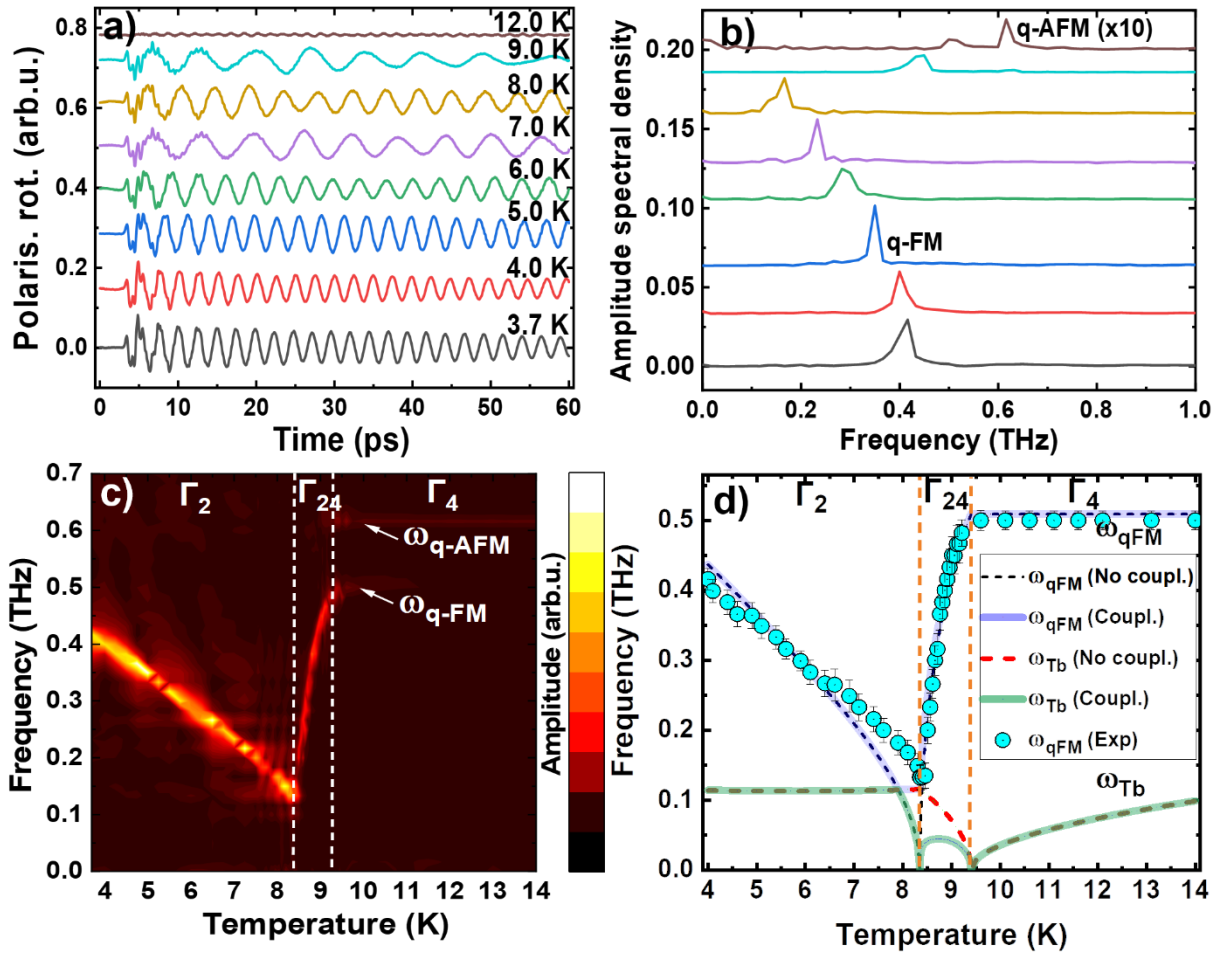

Fig.4.4. (a) shows the time-domain signal as a function of temperature for THz-driven spin dynamics in the *b*-cut of $TbFeO_3$. (b) presents the corresponding Fourier spectrum of the time-domain data in (a). (c) is a Fourier map plot derived from data in (b), showing the transition path from Γ_4 to Γ_2. (d) Data comparison between the experiment and the model.

Figure 4.4 (a), shows the temperature-dependent measurements of THz pump-induced iron spin dynamics across the temperature reorientation path from Γ_4 to Γ_2, with the two SRPTs occurring from 9.4 (Γ_4) to 8.35 K (Γ_2). Interestingly, alongside the magnetic oscillations corresponding to the q-FM frequency mode, some short-lived, fast oscillations occur between 5 to 10 picoseconds, whose nature remains uncertain as they do not correspond to any recognized magnetic or phononic oscillations. Fig 4.4(b) shows the corresponding Fourier spectra taken from (a) revealing two distinct resonance frequencies corresponding to the q-AFM mode in Γ_4 and q-FM mode in Γ_{24} phase, which is consistent with the selection rules. Figure

4.4(c) shows the Fourier map plot derived from data in (b) and Figure 4.4. (d) illustrates a very good match between experimental results from (c) and numerical modelling obtained from our quantum-phenomenological theory, which we will details in the next section of this chapter.

To summarize, our findings indicate that the overall trend in SRPT behaviour for the q-FM mode is consistent across both sample cuts. In their corresponding geometries in Γ_4 phase, the q-AFM mode is initially observed. Upon cooling temperature to T_1, 1st SRPT begins, and q-FM modes emerge as shown in Figures 4.3. (a) and 4.4. (a). As the temperature further decreases to T_2, reaching the Γ_2 phase (2nd SRPT), only the q-FM mode is observed, which is in complete agreement with the selection rules for AFMR modes.

However, unlike in the *b*-cut (Fig. 4.4. (c)) the *a*-cut (Fig. 4.3. (d)) does not exhibit a significant frequency decrease in the q-FM mode during SRPT, which we attribute to the interaction between magnon q-FM and impurity mode upon intersection or it might be due to the domain size of the sample which are not uniform and can be quite small up to a 10-20 μm while the probe size is around 60 μm. After reaching the Γ_2 phase at T_2, the q-FM frequency begins to increase again, reaching up to 0.4 THz in both cuts. However, unlike the *b*-cut, where no ordering of Tb^{3+} ions below 3.8 K was observed, the *a*-cut exhibits such ordering, which induces an additional 3rd SRPT, as shown in (Fig. 4.3 (c))**,** which leads to the reorientation of iron spins from Γ_2 to Γ_4 and as a result the emergence of the q-AFM mode is observed in the experiment. This behaviour is consistent with previous reports [108,190].

It should be noted that in both sample cuts, we did not directly observe oscillations of the Tb mode. On one hand, this may be due to the fact that our THz pump pulse does not excites this mode effectively, as its spectrum is well tuned to the AFMR modes frequency range (see Fig. 4.2(c)) or/and the wavelength of the probe pulse is insensitive. On the other hand, we observe the Tb mode indirectly through its interaction with the q-FM mode at T_2, where the softening of the q-FM mode stops due to strong dynamical repulsion with the Tb mode. This observation is consistent with previous reports [191,192].

Finally, in the *b*-cut sample (Fig.4.4. (d)) we achieved a very good agreement between experimental results and our quantum-phenomenological theoretical model, which will be discussed in detail in the following section.

4.6. Theoretical model for the coupled dynamics between Fe and Tb subsystems in $TbFeO_3$

4.6.1. Physical mechanism

The splitting of energy levels of a rare-earth ion in magnetic crystals like orthoferrites is influenced by the interplay of various effects, including crystal field, exchange interactions, and external magnetic fields [153]. These factors collectively shape the energy levels, depending on their relative orientations and alignment with the crystal axes. While the crystal field primarily establishes the energy level structure, exchange interactions and external fields introduce additional splitting mechanisms. In this section, we develop a phenomenological theoretical model based on qualitative considerations, assuming that in orthoferrites, with magnetic structure, in which the ground state of Tb^{3+} ions is degenerate or nearly degenerate becomes unstable at sufficiently low temperatures [193]. This instability represents a ***magnetic analogue*** of the cooperative Jahn-Teller effect. In cases where the magnetic crystal hosts ions with a degenerate ground state, coupled to the crystal through exchange (or dipole) interactions, such degeneracy can be lifted through the deformation of the magnetic structure. This deformation leads to a reduction in the magnetic symmetry of the ion's environment. If this deformation is cooperative, it could involve the entire magnetic configuration.

4.6.2. Thermodynamic potential

Based on the framework of the model developed in Chapter 3, let us now explore a version that accounts for magnetic Jahn-Teller-type phase transitions. As previously noted, to accurately describe the dynamics features of AFMR and R modes, it is essential to construct a thermodynamic potential that accounts for all relevant interactions within the two magnetic systems along the SRPT path. It has to be point out that, in rare earth orthoferrites (REOs), AFMR and R modes are interconnected, a factor that becomes particularly significant when the magnetic systems are closely aligned on the energy scale, as observed in $TbFeO_3$, but their analytical description is somewhat complex. However, in the case of rare-earth ions with non-Kramers ions, it is feasible to isolate pairs of frequency modes ($\omega_{qFM} - \omega_f$ and $\omega_{qAFM} - \omega_c$) that interact with each other, while neglecting interactions with other modes [125,153]. Moreover, based on the findings from the THz pump-optical probe experiment, our primary interest lies in describing the coupled behaviour of $\omega_{qFM} - \omega_{Tb}$.

For this matter, we consider thermodynamic potential for the coupled Fe and Tb subsystems accounting only for $\vec{G}$ and $\vec{f}$ vectors in the following form:

$$\Phi(\vec{G},\vec{f}) = \frac{1}{2}(K_{ac}G_z^2 + K_2G_z^4) - 9\mu_B f_\xi b G_z - f_\zeta \Delta_{\text{cf}} - \\ -\frac{1}{2}k_{\text{B}}T\left[\left(1+\sqrt{f_0^2}\right)\ln\left[1+\sqrt{f_0^2}\right] - \left(1-\sqrt{f_0^2}\right)\ln\left[1-\sqrt{f_0^2}\right]\right] \quad (4.1)$$

However, for more in-depth investigation of the mutual dynamics between the two magnetic subsystems, one needs to express the Neel vector $\vec{G}$ as a function of angle θ as expressed below:

$$\Phi(\theta,\vec{f}) = \frac{1}{2}\left(K_{ac}\sin[\theta]^2 + K_2\sin[\theta]^4\right) - 9\mu_B f_\xi b\sin[\theta] - f_\zeta \Delta_{\text{cf}} - \\ -\frac{1}{2}k_{\text{B}}T\left[\left(1+\sqrt{f_0^2}\right)\ln\left[1+\sqrt{f_0^2}\right] - \left(1-\sqrt{f_0^2}\right)\ln\left[1-\sqrt{f_0^2}\right]\right] \quad (4.2)$$

Here, the first two terms in the brackets account for the magnetocrystalline anisotropy, the third term describes the *d-f* exchange interaction, the fourth term is associated with the interaction with the crystal field, and the fifth term addresses the thermal population effect within the lowest-lying Tb quasi-doublet. The presence of the linear term in θ in the third term in the thermodynamic potential equation leads to the system`s instability; the quadratic term in θ limits the development of instability and stabilises the symmetric phase at relatively high temperatures.

By using the TP in the form of (4.2) we have been able to explore both static and dynamic properties (for more details see Appendix E) of the coupled Fe and Tb subsystems across the temperature path Γ_4-Γ_2 as well as to define the conditions for SRPT.

Fig. 4.5 below illustrates the results of modelling for the rare-earth (Tb) vector components and the deviation angle ψ of the rare-earth vector in Hilbert space as functions of θ across the temperature interval Γ_4-Γ_2.

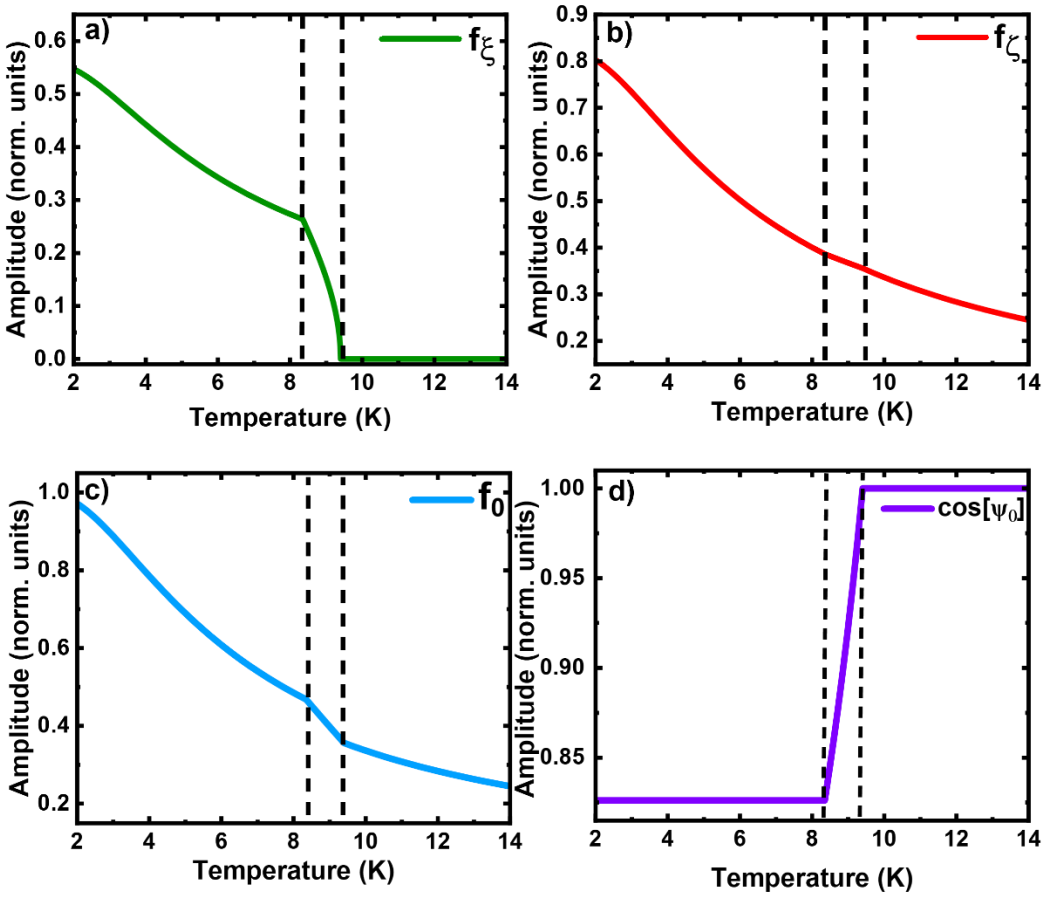

Fig.4.5. The rare-earth (Tb) $\vec{f}$ vector components (a,b,c) and deviation angle ψ (more details are in the Appendix E); (d) in Hilbert space as a functions of θ across the temperature interval Γ_4-Γ_2. Dashed lines indicate SRPT transition region.

4.6.3. Dynamical equations for the coupled Fe-Tb subsystems

We use a ***coupled oscillators*** model to describe the coupled dynamics of Fe and Tb subsystems in $TbFeO_3$ across the temperature transition path from Γ_4 to Γ_2. In this regard, one needs to construct a set of the dynamical equations of motion for both subsystems. For that reason, we use the Euler-Lagrange equation for the Fe and Landau-Lifshitz-Gilbert equation for Tb subsystem, as follows:

$$\begin{cases} \dfrac{d}{dt}\left(\dfrac{\partial \mathcal{L}}{\partial \dot{\theta}}\right) - \dfrac{\partial \mathcal{L}}{\partial \theta} = 0, \\ \dfrac{\mu_B}{\gamma}\dfrac{d\vec{f}}{dt} = \left[\vec{f} \times \dfrac{\partial \Phi}{\partial \vec{f}}\right]. \end{cases} \tag{4.3}$$

Here, $\mathcal{L} = \frac{M_{\mathrm{Fe}}}{2k_B\gamma H_{\mathrm{ex}}}\dot{\theta}^2 - \Phi(\theta, \vec{f})$- is Lagrangian function, M_{Fe} and H_{ex} are the magnetisation and the effective field of iron sublattice, k_{B} is a Boltzmann constant and γ is a gyromagnetic ratio.

By solving system (4.3) analytically (for more details see Appendix E), one could get the following solutions:

$$\begin{aligned}\tau_1 &= \frac{1}{2}\left(\omega_{\mathrm{qFM}}^2 + \omega_{\mathrm{Tb}}^2 - \sqrt{4\alpha\beta + \omega_{\mathrm{qFM}}^4 - 2\omega_{\mathrm{qFM}}^2\omega_{\mathrm{Tb}}^2 + \omega_{\mathrm{Tb}}^4}\right)\\ \tau_2 &= \frac{1}{2}\left(\omega_{\mathrm{qFM}}^2 + \omega_{\mathrm{Tb}}^2 + \sqrt{4\alpha\beta + \omega_{\mathrm{qFM}}^4 - 2\omega_{\mathrm{qFM}}^2\omega_{\mathrm{Tb}}^2 + \omega_{\mathrm{Tb}}^4}\right)\end{aligned} \tag{4.4}$$

Below, we present the results of numerical simulations across the temperature transition path from Γ_4 to Γ_2 based on these solutions:

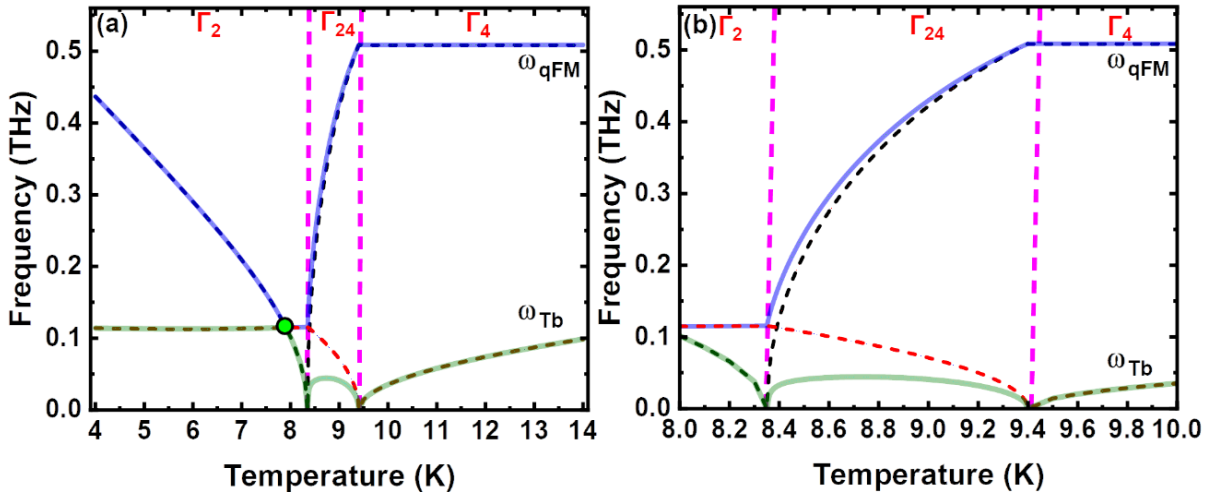

Fig.4.6. (a) Shows the numerical modelling of the solutions for the dynamical equation of the coupled Fe-Tb subsystems across the temperature path from Γ_4 to Γ_2. The dashed black and red lines illustrate the behaviour of ω_{qFM} and ω_{Tb} when coupling is neglected; the solid blue and light green lines take into account the coupling. The green circle at Γ_2 indicates the temperature point where hybridization between modes occurs. (b) A zoomed view of the temperature interval (Γ_{24} phase) where the spin-reorientation phase transition (SRPT) of iron spins occurs, also showing the avoided crossing behaviour due to the strong coupling between Fe and Tb subsystems. Dashed violet lines indicate SRPT transition region.

It is interesting to note that, as it follows from our model, during SRPT the q-FM mode experiences softening only at T_2, as a result of dynamic repulsion due to avoided crossing with the Tb frequency mode only in the intermediate region (Γ_{24}), and experiences hybridization (green circle) in the low-temperature region Γ_2. At the same time, the Tb mode softens at both temperatures T_1 and T_2 and approaches zero, which means that it experiences two phase transitions of the second kind.

4.7. Discussion of the results

Now, let us discuss in detail our results revealing signs of a cooperative magnetic Jahn-Teller effect during the course of SRPT in $TbFeO_3$.

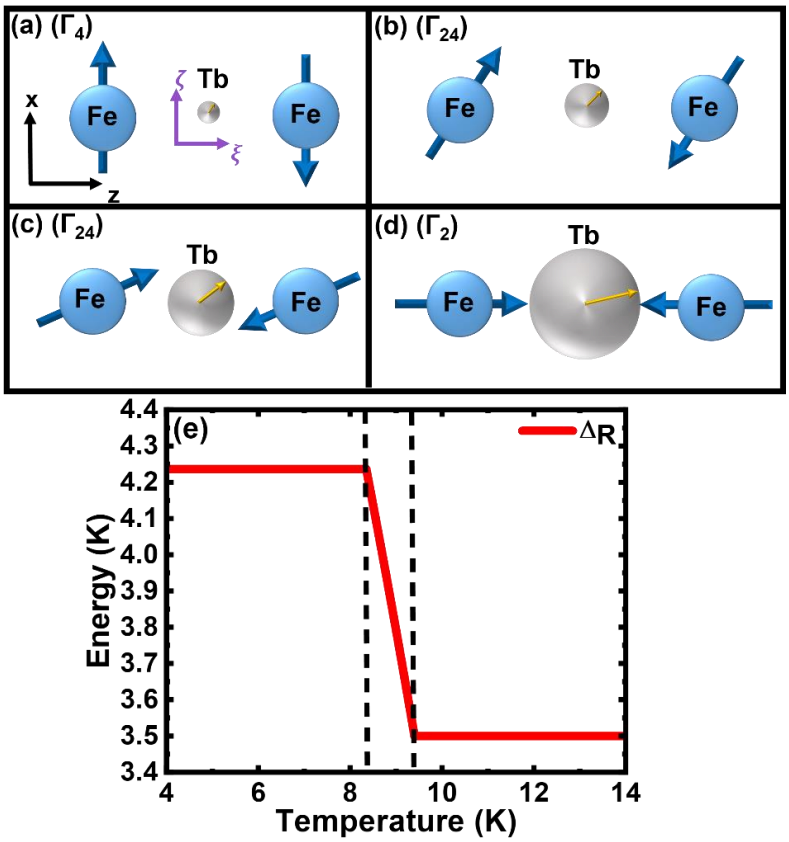

Fig.4.7. (a,b,c,d) Two antiferromagnetic iron spins coupled through the *d-f* exchange interaction to the Tb^{3+} ion, depicted as a Bloch sphere, the radius of which grows as temperature decreases; (e) Shows the results of the numerical modelling for the energy splitting function of the lowest quasi-doublet across the temperature path from Γ_4 to Γ_2 phase. Dashed black lines indicate the SRPT transition region.

Fig. 4.7(a) illustrates two antiferromagnetically aligned iron spins coupled to an unpolarised Tb^{3+} ion represented as a Bloch sphere of a two-level system in

Hilbert space, in the Γ_4 temperature phase. In this phase, the sphere has a small radius due to an equal population of electronic states within the lowest Tb quasi-doublet. As the temperature decreases to T_1, the 1st SRPT starts and the system enters the intermediate Γ_{24} temperature phase, during which the radius of the sphere begins to increase. This change reflects a shift in the electron population of the quasi-doublet states, enhancing the susceptibility of the Tb^{3+} ions to polarisation by the exchange field from the Fe subsystem.

From a theoretical perspective, as described in Eq. 4.2, this reorientation results from the common influence of *d–f* exchange, crystal field, and thermal population effects, which begin to compete with the magnetocrystalline anisotropy components upon entering the Γ_{24} phase at T_1. This competition drives the reorientation of the Fe spins into a more energetically favourable state, as illustrated in Fig. 4.7(a–d). As the temperature continues to drop and the SRPT progresses, the energy splitting Δ_R of the lowest quasi-doublet increases, as shown in Fig. 4.7(e). Upon reaching T_2 (the 2nd SRPT), the Fe spin system completes a 90° rotation, and Δ_R reaches its maximum. This transition ultimately lifts the degeneracy of the Tb^{3+} energy levels, providing clear evidence of the magnetic Jahn–Teller effect.

These results prove the reliability of our model, even when only one pair of AFMR and Tb frequency modes are considered. Moreover, this model enabled us to predict the behaviour of the Tb frequency mode, despite its absence in experimental observations, possibly due to the non-sensitivity of our 800 nm probe pulse to this mode. Additionally, within the framework of our model, we have successfully predicted the behaviour of this unobserved mode, identifying it as the soft one. This contrasts with the situation in $TmFeO_3$, considered in Chapter 3, where the q-FM mode is identified as a soft one. As stated in [54,98], the anisotropic parameters of the *d-f* exchange should be of the same order as the crystal field splitting, and according to our simulation results, these parameters are: Δ_{cf}=3.5 K, ($b\mu_B$)=2.39 K. Additionally, our model allowed us to calculate all functions of the Tb subsystem depending on θ and to numerically model their behaviour across the Γ_4 to Γ_2 temperature path.

Finally, it is of interest to estimate the ***coherence time*** parameter for $TbFeO_3$ within the framework of our model and to compare our results with existing quantum optics literature [194]. In quantum electrodynamics contexts (whether cavity QED or circuit QED), ***coherence*** refers to the ability of a coupled light–matter system to maintain well-defined phase relationships and undergo reversible (unitary) dynamics rather than merely decaying. In practical terms, a coherent light–matter interaction means the excitation can oscillate back-and-forth between a matter excitation (e.g.

an atom or qubit in an excited state) and a light excitation (a photon in a cavity) multiple times before dissipating. Achieving the strong coupling (SC) regime is essential for observing such coherent dynamics. Strong coupling is defined by the light–matter coupling strength g exceeding the relevant loss rates (the cavity field decay rate κ and the emitter's decay rate γ). When g is comparable to or larger than these decay rates, the system can undergo vacuum Rabi oscillations (repeated coherent energy exchange between light and matter) instead of decaying immediately. According to [194], strong coupling "is necessary to observe coherent quantum dynamics between light and matter," enabling fundamental single-photon/single-atom interactions and serving as a foundation for quantum information technologies. By contrast, if the coupling is weaker than losses, any excitation is lost to the environment before a coherent exchange can occur, resulting in incoherent (damped) dynamics.

While ***coherence*** describes the property of the quantum state (phase stability and reversible dynamics), the ***coherence time*** quantifies ***how long*** the system can maintain that coherence before environmental noise or dissipation destroys it. More specifically, a coherence time is the characteristic time over which a superposition state retains its phase information. In a two-level system (qubit), one often distinguishes between: (1) the energy relaxation time T_1 (the lifetime of an excitation before decaying) and (2) the dephasing time T_2 (the time over which phase coherence between, two states is lost). In high-quality circuit QED devices, for example, qubit excited-state lifetimes T_1 can be tens of microseconds and dephasing times T_2 of similar order, enabling many coherent Rabi oscillations to occur before the system decoheres. In coupled systems, the shorter of these timescales (qubit or cavity) usually limits the overall coherence of the joint dynamics. Measuring coherence times can be done in the time domain or in the frequency domain.

Therefore, we calculated the coherence time in our $TbFeO_3$ using the following empirical formula:

$$U = \sqrt{\left(\omega_{\mathrm{qFM}} - \omega_{\mathrm{Tb}}\right)^2 t_{\mathrm{qFM}} t_{\mathrm{Tb}}}, \tag{4.5}$$

Here, ω_{qFM}, ω_{Tb} represent the resonance frequencies, and t_{qFM}, t_{Tb} are the lifetimes of the Fe and Tb modes, respectively.

According to the results obtained from our model and by comparing it with [194], $TbFeO_3$ exhibits a strong coupling regime between Fe and Tb magnetic systems with the coherence parameter equal 7.3, as shown in Fig. 4.8.

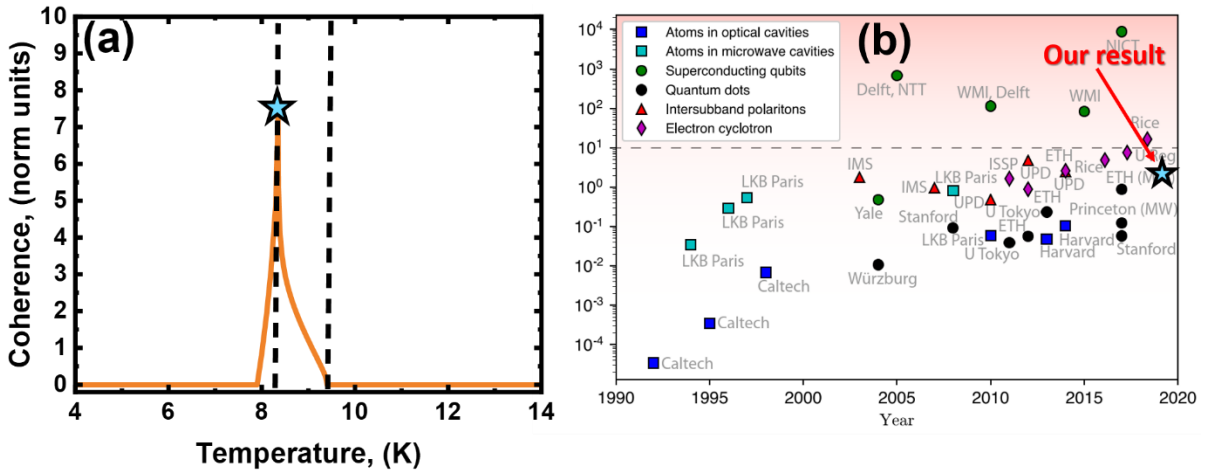

Fig.4.8. (a) Numerical modelling of the coherence parameter for the $TbFeO_3$ and its comparison (star sign) with the existing literature (b), reproduced with permission from [194]. Dashed black lines indicate the SRPT transition region.

4.8. Conclusions

To summarize, we performed THz pump-optical probe measurements in $TbFeO_3$ to reveal the signatures of the magnetic analogue of Jahn-Teller effect during spin-reorientation phase transitions of iron spins from Γ_4 to Γ_2 phase, leading to the changes in the magnetic symmetry of $TbFeO_3$. We achieved a very good match between our experimental results and quantum-phenomenological model, which we developed based on a two-level approximation for the R subsystem. This model elucidates the signatures of the magnetic Jahn-Teller effect by providing reliable values for the *d-f* exchange, crystal field splitting, and magneto-crystalline anisotropy parameters. We also successfully determined the removal of energy level degeneracy in Tb^{3+} ions, as well as the strong coupling between Fe and Tb ions, comparing it with other strongly coupled systems as documented in the existing literature [194]. Additionally, we observed the ordering of Tb^{3+} ions, below 3.8 K, leading to the induction of a third SRPT of iron spins in the *a*-cut sample, though these results require further theoretical development. Finally, we observed short-lived, fast oscillations of unknown nature, requiring further experimental and theoretical exploration. From a theoretical perspective, our model shows potential for extensions to describe other orthoferrites characterised by the avoided crossing behaviour of the q-FM mode during SRPT, and featuring an R mode with low-energy doublet states, such as in $HoFeO_3$ [195], $ErFeO_3$ [196], $YbFeO_3$ [197].

4.9. Appendix E. Theoretical model for the coupled Fe-Tb subsystems.

In this supplementary section, we present the results of analytical derivations made from the form of thermodynamics potential from Eq (4.2):

$$\Phi\left(\theta,\vec{f}\right)=\frac{1}{2}\left(K_{ac}\sin[\theta]^2+K_2\sin[\theta]^4\right)-9\mu_B f_\xi b\sin\left[\theta\right]-f_\zeta\Delta_{\mathrm{cf}}-$$
$$-\frac{1}{2}k_{\mathrm{B}}T\left[\begin{array}{l}\left(1+\sqrt{f_\xi^2+f_\eta^2+f_\zeta^2}\right)\ln\left[1+\sqrt{f_\xi^2+f_\eta^2+f_\zeta^2}\right]-\\-\left(1-\sqrt{f_\xi^2+f_\eta^2+f_\zeta^2}\right)\ln\left[1-\sqrt{f_\xi^2+f_\eta^2+f_\zeta^2}\right]\end{array}\right] \qquad \text{(E. 1)}$$

As the first step let`s define the equilibrium values for the $\vec{f}$ vector components. By repeating similar procedure as described in Supplementary Section A in Chapter III, one can get that:

$$\begin{cases}\sqrt{f_\xi^2+f_\eta^2+f_\zeta^2}=f_0\Longrightarrow f_0=\tanh\left[\dfrac{\Delta_{\mathrm{R}}}{k_BT}\right]\\ f_\xi=\dfrac{\Delta_{\mathrm{ex}}}{\Delta_{\mathrm{R}}}\tanh\left[\dfrac{\Delta_{\mathrm{R}}}{k_BT}\right],f_\eta=0,f_\zeta=\dfrac{\Delta_{\mathrm{cf}}}{\Delta_{\mathrm{R}}}\tanh\left[\dfrac{\Delta_{\mathrm{R}}}{k_BT}\right]\end{cases} \qquad \text{(E. 2)}$$

Then,

$$f_0^2-\left[\left(\frac{f_0 b\mu_B\sin[\theta]}{k_BT\,\mathrm{arctanh}[f_0]}\right)^2+\left(\frac{f_0\Delta_{\mathrm{cf}}}{k_BT\,\mathrm{arctanh}[f_0]}\right)^2\right]=0,$$

$$\tanh\left[\frac{\Delta_{\mathrm{R}}}{k_BT}\right]^2-\left[\left(\frac{\tanh\left[\frac{\Delta_{\mathrm{R}}}{k_BT}\right]b\mu_B\sin[\theta]}{\Delta_{\mathrm{R}}}\right)^2+\left(\frac{\tanh\left[\frac{\Delta_{\mathrm{R}}}{k_BT}\right]\Delta_{\mathrm{cf}}}{\Delta_{\mathrm{R}}}\right)^2\right]=0,$$

$$\tanh\left[\frac{\Delta_{\mathrm{R}}}{k_BT}\right]^2-\tanh\left[\frac{\Delta_{\mathrm{R}}}{k_BT}\right]^2\left[\left(\frac{b\mu_B\sin[\theta]}{\Delta_{\mathrm{R}}}\right)^2+\left(\frac{\Delta_{\mathrm{cf}}}{\Delta_{\mathrm{R}}}\right)^2\right]=0,$$

$$\left[\left(\frac{f_0 b\mu_B\sin[\theta]}{k_BT\,\mathrm{arctanh}[f_0]}\right)^2+\left(\frac{f_0\Delta_{\mathrm{cf}}}{k_BT\,\mathrm{arctanh}[f_0]}\right)^2\right]=1.$$

Finally, one can write the following one:

$$\begin{cases} \Delta_{\mathrm{R}} = \sqrt{\Delta_{\mathrm{ex}}^2 + \Delta_{\mathrm{cf}}^2}, \\ f_0 = \tanh\left[\dfrac{\Delta_{\mathrm{R}}}{k_B T}\right]. \end{cases} \qquad \text{(E. 3)}$$

Dynamics of any two-level system including atomic energy levels or qubit is convenient to describe by introducing a Bloch sphere in an abstract Hilbert space. Let`s have a look on a picture (see Fig.4.9) which represents a two-level system of the rare-earth (Tb^{3+}) ion as a Bloch sphere.

From this picture, one could see that:

$$\vec{f} = (f_0 \sin\psi\cos\chi, f_0 \sin\psi\sin\chi, f_0\cos\psi),$$
$$\frac{f_{\xi 0}}{f_0} = \cos\chi_0, \frac{f_{\zeta 0}}{f_0} = \cos\psi_0.$$

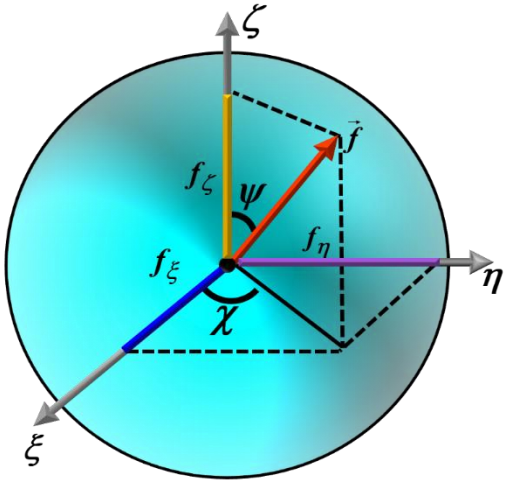

Fig.4.9. Illustration of a two-level system of Tb^{3+} ion as a Bloch sphere in a Hilbert space.

In this regard, the thermodynamic potential will become a function depending also on ψ and χ namely:

$$\Phi(\theta, \vec{f}) \longrightarrow \Phi(\theta, \psi, \chi)$$

All parameters for the Tb subsystem as a function of $\theta(T)$ have the following form:

$$\Delta_{\mathrm{R}} = \sqrt{\Delta_{\mathrm{cf}}^2 + (b\mu_{\mathrm{B}}\sin[\theta_0])^2} = \begin{cases} \Gamma_2 : \theta_0 = \frac{\pi}{2} \Longrightarrow \sqrt{\Delta_{\mathrm{cf}}^2 + (b\mu_{\mathrm{B}})^2}, \\ \Gamma_4 : \theta_0 = 0 \Longrightarrow \Delta_{\mathrm{cf}} \end{cases} \qquad \text{(E. 4)}$$

$$f_{\xi 0} = \frac{b\mu_{\mathrm{B}}\sin[\theta_0]}{\sqrt{\Delta_{\mathrm{cf}}^2 + (b\mu_{\mathrm{B}}\sin[\theta_0])^2}} \tanh\left[\frac{\sqrt{\Delta_{\mathrm{cf}}^2 + (b\mu_{\mathrm{B}}\sin[\theta_0])^2}}{T}\right] =$$

$$= \begin{cases} \Gamma_2 : \dfrac{b\mu_{\mathrm{B}}}{\sqrt{\Delta_{\mathrm{cf}}^2 + (b\mu_{\mathrm{B}})^2}} \tanh\left[\dfrac{\sqrt{\Delta_{\mathrm{cf}}^2 + (b\mu_{\mathrm{B}})^2}}{T}\right], \\ \Gamma_4 : 0 \end{cases} \qquad \text{(E. 5)}$$

$$f_{\zeta 0}=\frac{\Delta_{\mathrm{cf}}}{\sqrt{\Delta_{\mathrm{cf}}^2+(b\mu_{\mathrm{B}}\sin[\theta_0])^2}}\tanh[\frac{\sqrt{\Delta_{\mathrm{cf}}^2+(b\mu_{\mathrm{B}}\sin[\theta_0])^2}}{T}]=$$

$$=\begin{cases}\Gamma_2:\dfrac{\Delta_{\mathrm{cf}}}{\sqrt{\Delta_{\mathrm{cf}}^2+(b\mu_{\mathrm{B}})^2}}\tanh[\dfrac{\sqrt{\Delta_{\mathrm{cf}}^2+(b\mu_{\mathrm{B}})^2}}{T}] \\ \Gamma_4:\tanh[\dfrac{\Delta_{\mathrm{cf}}}{T}]\end{cases}, \qquad \text{(E. 6)}$$

$$f_0=\sqrt{f_{\xi 0}^2+f_{\zeta 0}^2}=\begin{cases}\Gamma_2:\tanh[\frac{\sqrt{\Delta_{\mathrm{cf}}^2+(b\mu_{\mathrm{B}})^2}}{T}], \\ \Gamma_4:\tanh[\frac{\Delta_{\mathrm{cf}}}{T}]\end{cases} \qquad \text{(E. 7)}$$

$$\cos[\psi_0]=\frac{f_{\zeta 0}}{f_0}=\begin{cases}\Gamma_2:\frac{\Delta_{\mathrm{cf}}}{\sqrt{\Delta_{\mathrm{cf}}^2+(b\mu_{\mathrm{B}})^2}}, \\ \Gamma_4:1\end{cases} \qquad \text{(E. 8)}$$

4.10. Dynamical equations for the coupled *f-d* subsystems

To describe the dynamical properties of the coupled f-d subsystems, one needs to construct the following set of dynamical equations:

$$\begin{cases}\dfrac{d}{dt}\left(\dfrac{\partial\mathcal{L}}{\partial\dot{\theta}}\right)-\dfrac{\partial\mathcal{L}}{\partial\theta}=0, \\ \dfrac{\mu_B}{\gamma}\dfrac{d\vec{f}}{dt}=\left[\vec{f}\times\dfrac{\partial\Phi}{\partial\vec{f}}\right].\end{cases} \qquad \text{(E. 9)}$$

Let`s start with the LLG equation in (E. 9). Considering the case that $\chi_0=0$ and $\psi_0\neq 0$, linearisation takes the following form:

$$\begin{cases}\sin\chi=\sin\chi_0+\delta\chi\cos\chi_0=\delta\chi, \\ \cos\chi=\cos\chi_0-\delta\chi\sin\chi_0=1, \\ \sin\psi=\sin\psi_0+\delta\psi\cos\psi_0, \\ \cos\psi=\cos\psi_0-\delta\psi\sin\psi_0.\end{cases}$$

In this regard, one could solve linearised LLG equation as:

$$\begin{cases} \dfrac{df_\xi}{dt} = -\dfrac{\gamma}{\mu_B}\Delta_{\text{cf}}\, f_\eta(t), \\ \dfrac{df_\eta}{dt} = \dfrac{\gamma}{\mu_B}\Delta_{\text{cf}}\, f_{\xi 0} + \dfrac{\gamma}{\mu_B}\Delta_{\text{cf}}\, f_\xi(t) - bf_{\zeta 0}\gamma\sin\theta_0 - b\gamma\sin\theta_0\, f_\zeta(t) - b\gamma\, f_{\zeta 0}\cos\theta_0\delta\theta(t), \\ \dfrac{df_\zeta}{dt} = \gamma b\sin\theta_0\, f_\eta(t). \end{cases}$$

$$\frac{d^2 f_\eta(t)}{dt^2} = \frac{\gamma}{\mu_B}\Delta_{\text{cf}}\,\frac{df_\xi}{dt} - \gamma b\,\text{Sin}\,\theta_0\,\frac{df_\zeta}{dt} - \gamma b f_{\zeta 0}\cos\theta_0\,\frac{d(\delta\theta)}{dt},$$

$$\frac{d^2 f_\eta(t)}{dt^2} + f_\eta(t)\omega_{\text{RE}} = -\gamma b f_{\zeta 0}\cos\theta_0\,\frac{d(\delta\theta)}{dt},$$

By introducing the new variable $x = \delta\dot{\theta}$, one could write the following oscillatory equation for the Tb subsystem:

$$\frac{d^2(\delta\chi)}{dt^2} + \delta\chi\omega_{\text{Tb}}^2 = \alpha x. \qquad \text{(E. 10)}$$

Here, $\omega_{\text{Tb}} = \sqrt{(\frac{\gamma}{\mu_B}\Delta_{\text{cf}})^2 + (\gamma b\sin\theta_0)^2}$ - is the resonance frequency of the Tb mode, and $\alpha = -\gamma b f_{\zeta 0}\cos\theta_0$ - is the coupling rate coefficient for Tb subsystem.

Let`s proceed to the Euler-Lagrange equation from (E.9).

$$\mathcal{L} = \frac{M_{\text{Fe}}}{2\gamma^2 H_{\text{ex}}}\delta\dot{\theta}^2 - \Phi(\theta,\psi,\chi),$$

$$\frac{d}{dt}\left(\frac{\partial\mathcal{L}}{\partial\dot{\theta}}\right) - \frac{\partial\mathcal{L}}{\partial\theta} = 0, \frac{d}{dt}\left(\frac{\partial\mathcal{L}}{\partial(\dot{\delta\theta})}\right) = \frac{M_{\text{Fe}}}{\gamma^2 H_{\text{ex}}}\delta\ddot{\theta}.$$

By applying the same linearisation procedure and considering that $\sin(\chi_0) = 0$, $\cos(\chi_0) = 1$ and $\psi_0 \neq 0$, one can write that linearised Euler-Lagrange equation has the following form:

$$\frac{\partial\mathcal{L}}{\partial(\delta\theta)} = -\frac{\partial\Phi(\theta,\psi,\chi)}{\partial\theta} = \delta\psi\,\frac{b^2\mu_{\text{B}}^2\sin 2\theta_0\cos\chi_0\cos\psi_0\tanh\frac{\Delta_{\text{R}}}{k_{\text{B}}T}}{\Delta_{\text{R}}} + \delta\theta(K_{\text{ac}}(\cos\theta_0)^2 -$$

$$K_{\text{ac}}(\sin\theta_0)^2 + 6K_2(\cos\theta_0\sin\theta_0)^2 - K_2(\sin\theta_0)^4 - 2\frac{b^2\mu_{\text{B}}^2\cos 2\theta_0\cos\chi_0\sin\psi_0\tanh\frac{\Delta_{\text{R}}}{k_{\text{B}}T}}{\Delta_{\text{R}}}),$$

$$\delta\ddot{\theta}\frac{M_{\mathrm{Fe}}}{\gamma^2 H_{\mathrm{ex}}}+\delta\theta(K_{\mathrm{ac}}(\cos 2\theta_0)^2+6K_2(\cos\theta_0\sin\theta_0)^2-K_2(\sin\theta_0)^4-2\frac{b^2\mu_{\mathrm{B}}^2\cos 2\theta_0\cos\chi_0\sin\psi_0\tanh\frac{\Delta_{\mathrm{R}}}{k_{\mathrm{B}}T}}{\Delta_{\mathrm{R}}})=-\delta\psi\frac{b^2\mu_{\mathrm{B}}^2\sin 2\theta_0\cos\chi_0\cos\psi_0\tanh\frac{\Delta_{\mathrm{R}}}{k_{\mathrm{B}}T}}{\Delta_{\mathrm{R}}}.$$

By differentiating it with respect to the time one could get:

$$\frac{d^3(\delta\theta)}{dt^3}+\frac{\gamma^2 H_{\mathrm{ex}}}{M_{\mathrm{Fe}}}\frac{d(\delta\theta)}{dt}(K_{\mathrm{ac}}(\cos 2\theta_0)^2+6K_2(\cos\theta_0\sin\theta_0)^2-K_2(\sin\theta_0)^4-2\frac{b^2\mu_{\mathrm{B}}^2\cos 2\theta_0\cos\chi_0\sin\psi_0\tanh\frac{\Delta_{\mathrm{R}}}{k_{\mathrm{B}}T}}{\Delta_{\mathrm{R}}})=$$

$$=-\frac{d(\delta\psi)}{dt}\frac{\gamma^2 H_{\mathrm{ex}}}{M_{\mathrm{Fe}}}\frac{b^2\mu_{\mathrm{B}}^2\sin 2\theta_0\cos\chi_0\cos\psi_0\tanh\frac{\Delta_{\mathrm{R}}}{k_{\mathrm{B}}T}}{\Delta_{\mathrm{R}}}.$$

By substituting the following formula for ψ angle $\frac{d(\delta\psi)}{dt}=-\gamma b sin(\theta_0)\delta\chi=\beta$, $\cos\chi_0=1$ and by substituting variables $\frac{d(\delta\theta)}{dt}=x$:

$$\frac{d^2x}{dt^2}+\omega_{\mathrm{Fe}}^2 x=\beta\delta\chi. \qquad (\mathrm{E}.11)$$

Here, $\omega_{\mathrm{Fe}}=\sqrt{\frac{\gamma^2 H_{\mathrm{ex}}}{M_{\mathrm{Fe}}}(K_{\mathrm{ac}}(\cos 2\theta_0)^2+6K_2(\cos\theta_0\sin\theta_0)^2-K_2(\sin\theta_0)^4-2\frac{b^2\mu_{\mathrm{B}}^2\cos 2\theta_0\sin\psi_0\tanh\frac{\Delta_{\mathrm{R}}}{k_{\mathrm{B}}T}}{\Delta_{\mathrm{R}}})}$ and $\beta=-\frac{\gamma^3 H_{\mathrm{ex}}}{M_{\mathrm{Fe}}}\frac{b^3\mu_{\mathrm{B}}^2\sin 2\theta_0\cos\psi_0\tanh\frac{\Delta_{\mathrm{R}}}{k_{\mathrm{B}}T}}{\Delta_{\mathrm{R}}}$ are the Fe mode's resonance frequency and the Fe subsystem's coupling rate coefficient.

At this point one, let`s construct the following set for the coupled oscillators, namely:

$$\begin{cases}\frac{d^2(\delta\chi)}{dt^2}+\omega_{\mathrm{Tb}}^2\delta\chi=\alpha x,\\ \frac{d^2x}{dt^2}+\omega_{\mathrm{Fe}}^2 x=\beta\delta\chi.\end{cases} \qquad (\mathrm{E}.12)$$

Solutions for this set could be obtained by using the following matrix approach:

$$\begin{vmatrix} (\lambda^2 + \omega_{\mathrm{qFM}}^2) & -\alpha \\ -\beta & (\lambda^2 + \omega_{\mathrm{Tb}}^2) \end{vmatrix} = 0, \qquad \text{(E. 13)}$$

$$\lambda^4 + \lambda^2\omega_{\mathrm{qFM}}^2 + \lambda^2\omega_{\mathrm{qFM}}^2 + \omega_{\mathrm{qFM}}^2\omega_{\mathrm{Tb}}^2 - \alpha\beta = 0, \qquad \text{(E. 14)}$$

By making the substitution: $\lambda^2 = \tau,\ \lambda^4 = \tau^2$, we derived the following solutions:

$$\begin{aligned} \tau_1 &= \frac{1}{2}\left(\omega_{\mathrm{qFM}}^2 + \omega_{\mathrm{Tb}}^2 - \sqrt{4\alpha\beta + \omega_{\mathrm{qFM}}^4 - 2\omega_{\mathrm{qFM}}^2\omega_{\mathrm{Tb}}^2 + \omega_{\mathrm{Tb}}^4}\right) \\ \tau_2 &= \frac{1}{2}\left(\omega_{\mathrm{qFM}}^2 + \omega_{\mathrm{Tb}}^2 + \sqrt{4\alpha\beta + \omega_{\mathrm{qFM}}^4 - 2\omega_{\mathrm{qFM}}^2\omega_{\mathrm{Tb}}^2 + \omega_{\mathrm{Tb}}^4}\right) \end{aligned} \qquad \text{(E. 15)}$$

Chapter V. Ultrafast dynamics of rare-earth low-energy states in $Tb_3Ga_5O_{12}$

5.1. Motivation

Terbium gallium garnet (TGG) $Tb_3Ga_5O_{12}$ belongs to the rare-earth garnet material class, known for its exceptional magneto-optical properties, high transparency across a broad spectral range, and robust thermal and mechanical stability. Its unique magnetic and optical properties have made it essential in various photonic and magneto-optical devices, including Faraday modulators and optical lasers. The complex sublattice arrangements of TGG provide a rich magnetic structure that enables a wide range of applications and positions it as a model system for studying fundamental magneto-optical effects. Despite its extensive practical applications, some gaps remain in understanding the low-temperature magnetism of Tb^{3+} ions. Unlike the situation in rare-earth orthoferrites, in garnets, there are no strong interactions between rare-earth ions and Ga. Therefore, the primary objective of this chapter is to investigate and compare the effects of THz and optical excitations on Tb^{3+} crystal field states in $Tb_3Ga_5O_{12}$.

5.2. Magnetic properties of $Tb_3Ga_5O_{12}$

5.2.1. Crystal structure and electronic configuration

TGG crystallizes in a cubic garnet structure characterised by a complex atomic arrangement. This structure is composed of a three-dimensional network of oxygen ions that create polyhedral sites occupied by terbium (Tb) and gallium (Ga) ions. The Tb^{3+} ions are located in dodecahedral sites with distorted cubic symmetry, which significantly impacts their electronic and magnetic properties. The electronic configuration of Tb^{3+} ions leads to a highly localized *4f* orbital, shielded by outer electrons, resulting in well-defined energy levels with minimal overlap with neighbouring ions. This configuration also results in strong spin-orbit coupling and crystal field effects, which split the ground multiplet $^7F_6$ into several sublevels. These energy levels are critical for the material's optical and magnetic properties, enabling transitions that contribute to its magneto-optical properties [198,199].

5.2.2. Optical and magnetic properties

At high temperatures, TGG is valued not only for its large Verdet constant and high transparency, which make it suitable for Faraday rotators and optical isolators [200], but also for exhibiting additional phenomena such as the acoustic Faraday effect [201,202], the Cotton-Mouton effect [203], and the thermal Hall effect [204,205], for which it is considered a prototypical system. These phenomena establish TGG as a model system for studying these effects, underscoring the crucial role of spin-lattice interactions within the material. The $Tb_3Ga_5O_{12}$ crystal demonstrates high transparency in the visible and near-infrared regions, enhancing its use as a component in optical isolators and modulator devices. Regarding its magnetic properties, TGG exhibits Ising-like behaviour of Tb ions and their placement within the garnet lattice. Above its Néel temperature of approximately 0.25 K [206], transitioning to complex magnetic ordering at lower temperatures. The six magnetic sublattices interact anisotropically, leading to unique spin dynamics observable under external magnetic fields.

5.2.3. Spectroscopic Studies

Advanced spectroscopic techniques have provided deeper insights into the behaviour of TGG under varying conditions of temperature, magnetic fields, and light polarisation and have proven it not only as a functional material but also as a platform for exploring fundamental opto-magnetic interactions. For instance, recent optical pump-probe studies have revealed ultrafast phenomena such as terahertz modulation of the Faraday rotation by laser pulses via the optical Kerr effect [207], and tuneable magneto-optical modulation [208].

However, the challenge in using the whole optical pump-probe technique in Terbium Gallium Garnet (TGG) arises from the influence of the optical pump on both the magnetic order and the magneto-optical coefficient, denoted as: $\Delta\theta \sim \chi_{\mathrm{magn-opt}}(M, L)$. Consequently, such experimental results yield not straightforward interpretations, leading to debates about the reliability of the signals obtained from optical pumping and how accurately they reflect the actual magnetisation dynamics.

For instance, in experiments conducted on a 1 mm thick sample in the optical pump-probe setup with a substantial applied magnetic field (up to 70 kG) [207], harmonic oscillations were observed with frequencies dependent on the magnetic field strength. Although these oscillations resembled the magnetic resonance, they were found not to possess a magnetic nature. Instead, their occurrence was identified

as a manifestation of the measurement peculiarities, where the polarisation plane of the pump/probe pulse in TGG induces such "spatial oscillations" with frequencies similar to the spin ones.

Therefore, it can thus be concluded that while experiments with optical pumping and probing may produce results resembling magnetic responses, these are, in fact, optical artefacts.

Consequently, investigations of TGG have turned to the THz spectroscopy [209]. This study has demonstrated the coupling of high-frequency magnetic excitations with the crystal's spin subsystem, revealing characteristics of an anisotropic g-tensor and providing insights that are crucial for understanding material properties such as magnetic susceptibility and thermal conductivity under diverse conditions.

In the work [210], the authors investigated the interaction between light and magnetism on femtosecond timescales using the related compound $Dy_3Al_5O_{12}$, particularly focusing on the validity of the inverse Faraday effect (IFE). Contrary to the predictions of the conventional thermodynamic IFE model, the experiments revealed unexpected results. Instead of inducing quasi-static magnetisation, the laser pulse generated a coherent oscillation at 2.17 THz. This frequency significantly exceeds what is typically expected for conventional magnetisation precession, suggesting an alternative underlying mechanism. The observed oscillation coincided with the energy splitting between the crystal-field levels of the Dy^{3+} ions, indicating that the pump pulse induces a coherent superposition of magnetic sublevels, rather than directly magnetising the material.

In our pump-probe spectroscopy studies, we examined the magnetic dynamics of Tb^{3+} ions in $Tb_3Ga_5O_{12}$, which are not affected by the interaction with Ga ions. We used two types of pump pulses: a 400 nm pulse for stimulated Raman excitations and a THz pulse for resonant excitations, which effectively excites electron transitions between the lowest energy state formed by two closely located singlets and the next energy state of the Tb^{3+} ions within the ground-state multiplet $^7F_6$. We compared the effects of these resonant and Raman-stimulated excitations by analysing the temperature-dependent behaviour of the crystal field (CF) mode.

5.3. Experimental setup

In this section, we present time-resolved studies of ultrafast dynamics conducted on 10 mm × 5 mm × 1 mm $Tb_3Ga_5O_{12}$ single crystal cut such that the surface plane is the [111] plane. Measurements were performed in transmission

geometry using two types of excitations: Raman (400 nm) and resonant (THz), see Fig. 5.1.

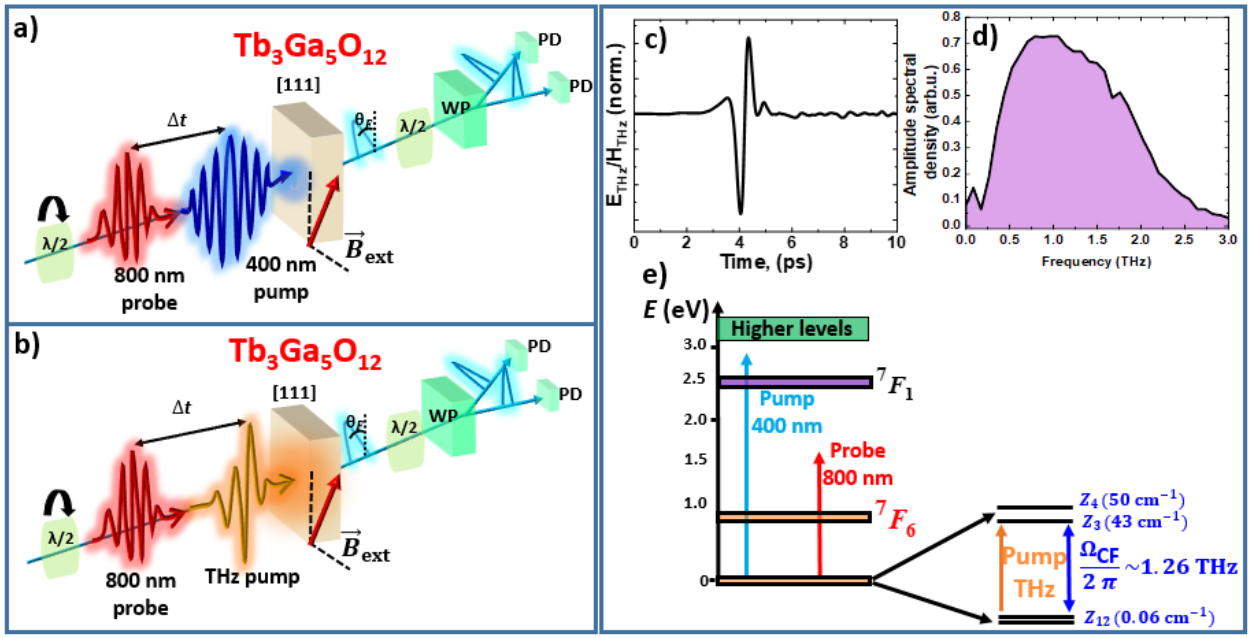

Fig.5.1. Sketch of the experimental geometries: (a) for the 400 nm pump-800 nm probe, (b) for the THz pump-800 nm probe, (c) Time-resolved THz pulse form obtained with the use of EOS and its spectrum (d), (e) Electronic structure of the Tb^{3+} ions in $Tb_3Ga_5O_{12}$ along with photon energies of the pump and probe pulses used in the experiment.

For Raman excitation, we used a 400 nm pump and an 800 nm probe setup (see Fig.5.1. (a)). For resonant excitation, we employed an intense THz pump with an 800 nm probe (shown in Fig.5.1. (b)). The sample was placed in a closed-cycle liquid helium cryostat, allowing temperature control down to 3.4 K (the lowest T which we could achieve), with an external magnetic bias field applied at 45° with respect to the [111] plane to obtain the best signal accuracy. More details about the pump-probe technique are discussed in Chapter 2. Fig.5.1. (c) shows the intense THz pulses (with electric field values up to 1 MV/cm) and the corresponding Fourier spectrum (Fig.5.1. (d)), which were generated using the optical rectification technique in $LiNbO_3$. Fig. 5.1. (e) illustrates the electronic structure of Tb^{3+} ions in the distorted cubic symmetry of $Tb_3Ga_5O_{12}$, emphasising the electronic transitions within the ground-state multiplet $^7F_6$ [199]. The first closely located singlet states $Z_{1,2}$ form the quasi-doublet. Our THz pump effectively excites the transition between this quasi-doublet and the next energy level Z_3.

5.4. THz and laser-induced dynamics of Tb^{3+} ions in $Tb_3Ga_5O_{12}$

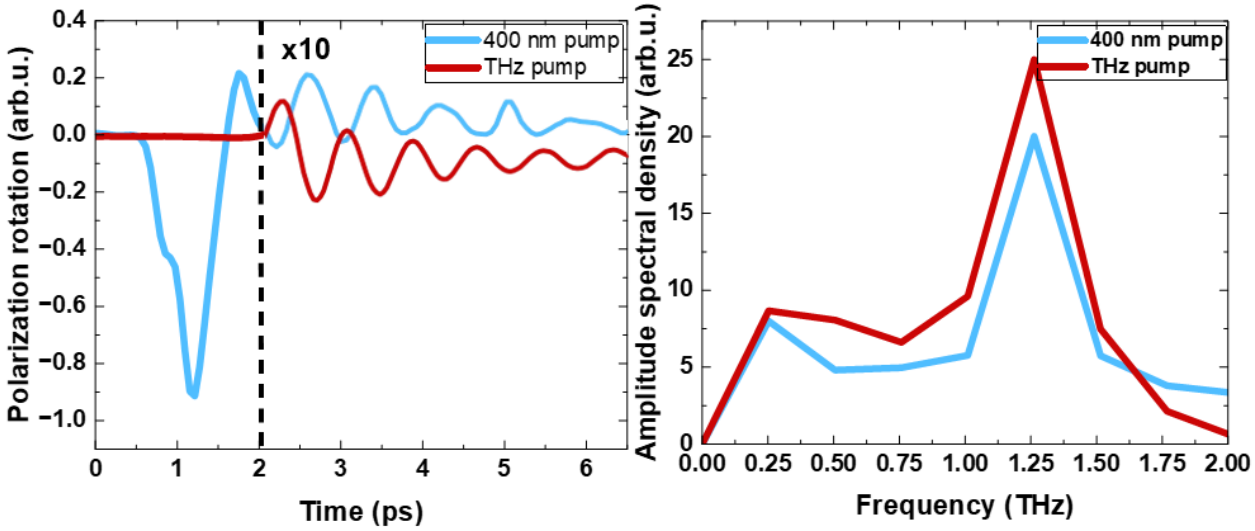

Fig.5.2: (a) Time-resolved measurements at 3.4 K of 400 nm (blue) and THz (red) pump pulses; (b) Fourier transforms of the time-domain data from (a).

Figure 5.2(a) displays time-resolved measurements for 400 nm and THz pump pulses at the lowest temperature of 3.4 K, where the highest signal amplitude was detected. Figure 5.2(b) presents the Fourier transforms calculated from the time-domain data in (a), in particular from the area magnified by a factor of 10 and indicated after the dotted line. Based on the calculated data from [211], we attribute this mode of Tb^{3+} ions to the crystal field (CF) mode between $Z_{1,2}$ and Z_3 energy levels within the $^7F_6$ multiplet (see Fig.5.1. (e)).

Fig.5.3.(a,b) shows probe (800 nm) and pump (400 nm) polarisation dependences both measured at 3.4 K. Here, the zero-angle reference for the probe and pump polarisations is oriented horizontally relative to the [111] surface of the sample and lies in the plane of the external magnetic field.

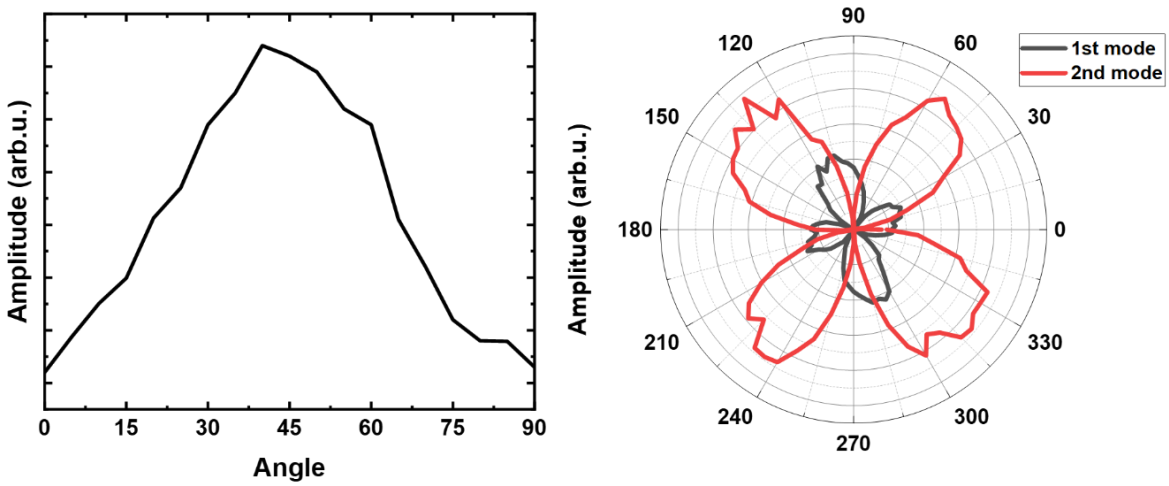

Fig.5.3. a) 800 nm probe and b) 400 nm pump polarisation dependencies at 3.4 K.

In the case of probe polarisation dependence, we observed a maximum at 45°, which is indicative of the Cotton-Mouton effect. Our pump polarisation measurements detected two oscillating Raman modes with the same frequency but with different excitation mechanisms (symmetry). These modes were revealed by analysing the Fourier spectra for all time-domain values of pump polarisation angles from 0 to 360 with a step in 5° at 3.4 K. Existing research [211,212] explains the occurrence of two Raman modes at the same frequency in a similar rare-earth garnet ($Tb_3Al_5O_{12}$) through both resonance and non-resonance Raman excitations.

To quantify their amplitudes, we fitted the time-domain data measured at different angles using the following formula:

$$\mathrm{Sig}_1 = (A_1 + B_1)\sin[\omega t + \phi_0] \cdot \exp\left[-\frac{t}{C}\right] \qquad (5.1)$$

Here, A_1 and B_1 represent the amplitude values for the first and second modes, respectively, ω denotes the angular frequency of the mode, ϕ_0 is the phase shift, t is the time, and C is the decay parameter.

Fig.5.4 (a,b) shows 800 nm probe and THz pump polarisation dependences at 3.4 K. Similar to the case of the optical pump, here the probe polarisation dependence, shows the similar signature of the Cotton-Mouton effect. In the case of the THz pump, the largest torque effect is observed when the external magnetic field is perpendicular to the magnetic component of the THz pulse.

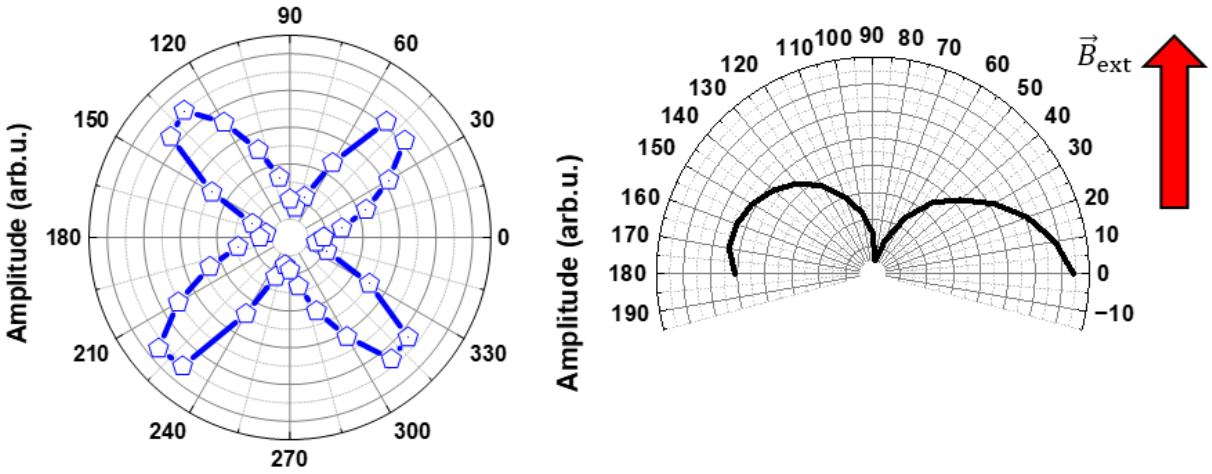

Fig.5.4. a) 800 nm probe and b) THz pump polarisation dependencies at 3.4 K.

Fig 5.5. shows the results of measurements of Tb^{3+} ions in $Tb_3Ga_5O_{12}$ using a 400 nm pump and 800 nm probe as a function of the sample temperature. In this configuration, the polarisation of the pump and probe pulses were oriented at an angle of 45° with respect to the horizontal orientation and the external magnetic field, which was applied at 45° with respect to the sample plane [111], to obtain the best signal.

Temperature-dependent measurements were performed from 3.4 to 60 K (Fig. 5.5(a)). As can be seen, the magnetic oscillations have lifetimes from 3.0 to 7.5 ps, and the amplitude of the oscillations decreases with increasing temperature. The Fourier transforms (Fig. 5.5(b)), calculated from the time-domain data in Fig. 5.5(a), show a mode with a resonant frequency of 1.26 THz. Fig. 5.5(c) shows the temperature dependence of the amplitude of this mode, taken from Fig. 5.5(b). As observed, the peak amplitude starts to decrease with increasing temperature. Fig. 5.5(d) shows the dynamic signals in the time domain for three orientations of the external magnetic field and one in the absence of the external magnetic field.

Given that the transition occurs between the lowest energy level formed by two closely spaced singlets and the first excited state in the $^7F_6$ multiplet, and neglecting other high-energy states, the Tb^{3+} ions can be considered as an ensemble of two-level systems (TLS). For a two-level system interacting with light [213], Boltzmann statistics predicts a nearly uniform population distribution of the eigenstates at low occupancy.

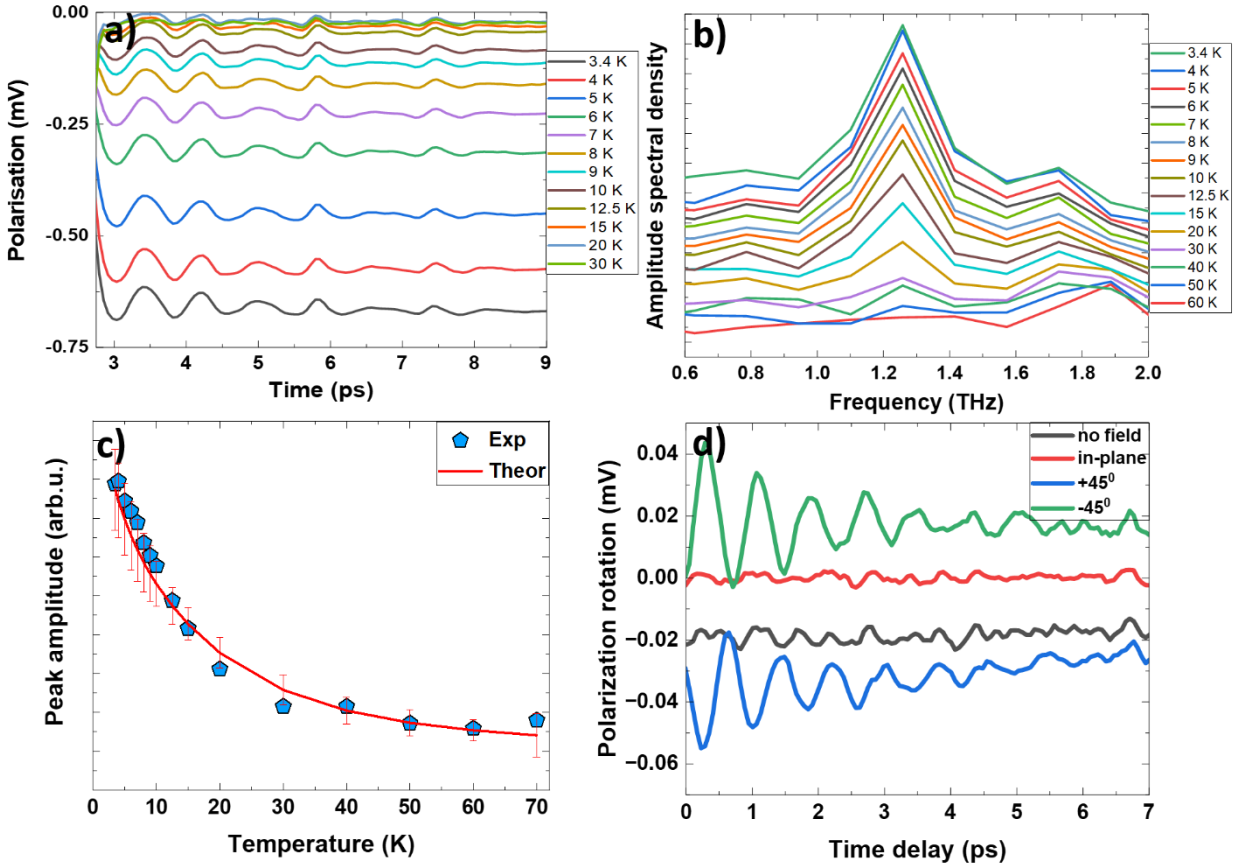

Fig.5.5. a) Temperature dependence of the 400 nm induced dynamics in $Tb_3Ga_5O_{12}$; b) Fourier transforms of the time domain data from a); c) Extracted amplitudes of the 1.26 THz mode from the spectra in b); d) dynamical signal for the different configurations of the external magnetic field (the measurements in a) were performed at the +45°).

Upon pulsed excitation, the population distribution is consistent with Boltzmann statistics. With increasing occupancy, the system transitions to quantum statistics, leading to an effective population of the ground state and saturation of the upper level, consistent with the predictions of statistical mechanics.

In this regard, the dynamics of the occupation difference $\Delta n(T)$ between the two levels could be described by using the Boltzmann distribution function in the following form:

$$\Delta n(T) = A \cdot \tanh\left[\frac{\Delta E}{k_B T}\right] \frac{1}{(T+8.2)} \qquad (5.2)$$

Here, A is a constant, ΔE is the energy gap of 5.2 meV (42 cm^{-1}) between the $Z_{1,2}$ and Z_3 levels within the $^7F_6$ multiplet according to [199], T is the temperature, and $\frac{1}{(T+8.2)}$ accounts for the detection part with θ_{CW}=-8.2 K is the Curie-Weiss parameter.

Fig 5.6. shows the results of THz-pump and 800 nm-optical probe measurements of Tb^{3+} ions in $Tb_3Ga_5O_{12}$, performed in a similar configuration to the previous case. For these measurements, the polarisation of the pump pulse was set at 90°, the probe polarisation was oriented at 45° relative to the horizontal plane, to optimise signal detection and the external magnetic field, which was applied at 45° with respect to the sample plane [111].

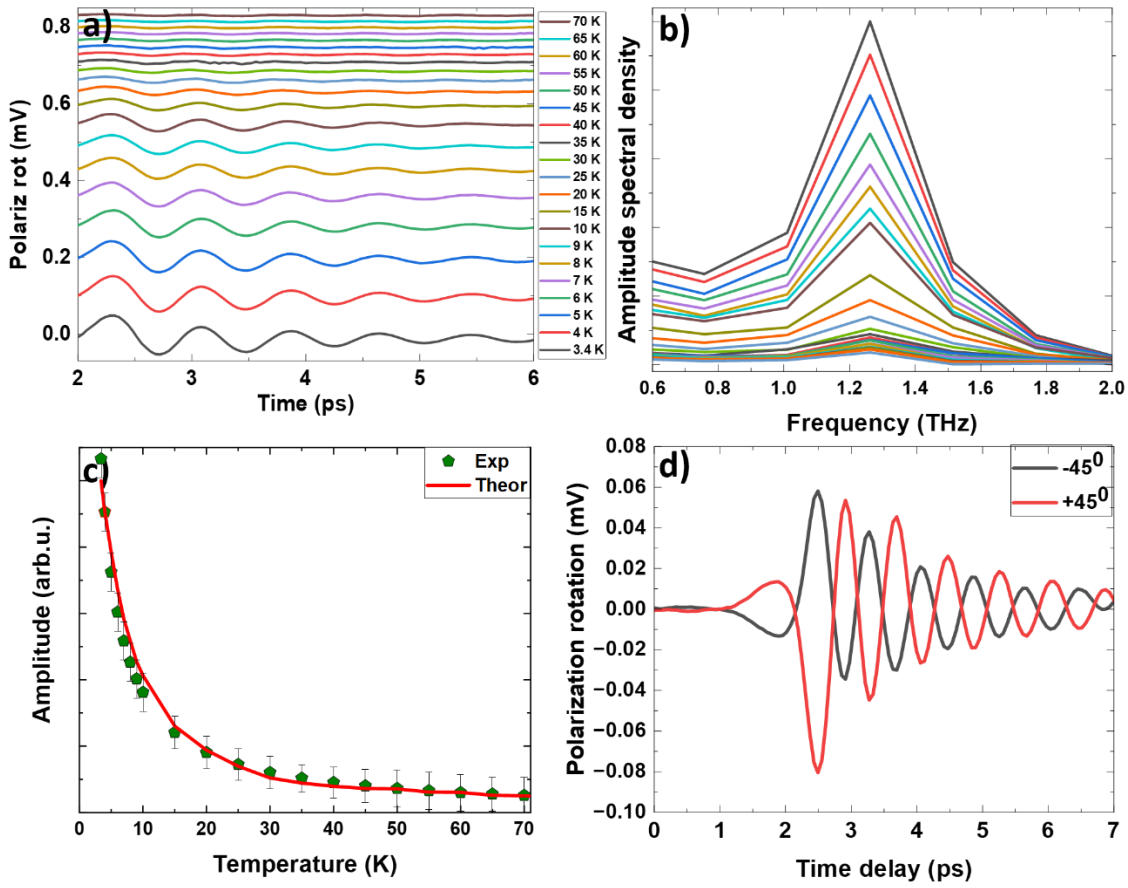

Fig.5.6. a) Temperature dependence of the THz-induced dynamics in $Tb_3Ga_5O_{12}$; b) Fourier transforms of the time-domain data from a); c) Extracted amplitudes of the 1.26 THz mode from the spectra in b); d) dynamical signal for the different configurations of the external magnetic field (the measurements in (a) were performed at the +45°).

Temperature-dependent measurements were performed across the temperature interval from 3.4 to 70 K (Fig. 5.6 (a)). As can be seen, similarly to the optical pump case, the magnetic oscillations have lifetimes from 2.0 to 6.0 ps, and the amplitude of the oscillations decreases with an increase in temperature. The corresponding Fourier transforms (Fig 5.6 (b)), calculated from the time-domain data in Fig. 5.6(a), revealed the same crystal field mode with an oscillation frequency of 1.26 THz. Fig 5.6 (c) displays the temperature dependence of the amplitude of this mode, and Fig 5.6 (d) shows the dynamic signals for the two opposite orientations of the external magnetic field, which have opposite behaviour.

As shown in Fig. 5.6(c), the curve depicting the temperature dependence of the amplitude of the crystal field (CF) mode has a larger curvature compared to the previous cases, which implies a different nature of the excitation. In this case, the use of the Boltzmann distribution function is no longer valid due to the impossibility to reach the necessary curvature. Instead, we managed to fit this curve by using the following phenomenological formula:

$$\mathrm{Sig}_2 = \left(\frac{A_2}{(T+8.2)} + \frac{B_2}{(T+8.2)^2}\right). \quad (5.3)$$

Here, A_2 (98) and B_2 (2057) are the amplitude constants, and T is the temperature. As can be seen from the formula the obtained dependence has the following behaviour: $M + M^2$, which indicates a more complex excitation mechanism, requiring a more sophisticated theoretical analysis.

5.5. Conclusions

We performed a systematic measurements of spin dynamics in $Tb_3Ga_5O_{12}$ as a function of temperature. For this we used pump-probe technique with two types of excitations: optical (400nm) and THz. The detection of spin dynamics has been done using transient polarisation of 800 nm probe, in a temperature range from 3.4 to 70 K. In both setups, we observed a 1.26 THz frequency of the crystal field mode which corresponds to the energy gap of 42 cm^{-1} or 5.2 meV between $Z_{1,2}$ and Z_3 energy levels according to [199]. However, in our optical pump (400 nm) experiment, we revealed two modes with the same frequency but different excitation mechanisms (symmetry), which we attributed to resonance and non-resonance Raman excitations according to the existing research [211,212] on a similar compound $Tb_3Al_5O_{12}$. By applying the Boltzmann distribution function, we achieved a good match between the temperature-dependent amplitudes of the observed modes and theoreticaly

predicted amplitude. Under THz pump excitation, although the same frequency was observed, a phenomenological formula had to be used to achieve good agreement with the experimental results. In this regard, a more sophisticated theoretical framework is needed to accurately explain the underlying excitation mechanisms.

Chapter VI. Summary and Outlook

6.1. Summary

This thesis work describes theoretical and experimental studies of the spin reorientation phase transition in orthoferrites with non-Kramers ions, namely $TmFeO_3$ and $TbFeO_3$ and the ultrafast spin dynamics in Terbium gallium garnet ($Tb_3Ga_5O_{12}$) crystal.

The exploration of rare-earth orthoferrites ($RFeO_3$) has unveiled a wealth of magnetic phenomena driven by the interplay of rare-earth (R) and iron (Fe) subsystems. In this thesis work we have made significant strides in understanding the nonlinear spin dynamics in $RFeO_3$ materials, particularly under the influence of strong terahertz (THz) fields. Through a combination of theoretical modelling and experimental investigation, we have characterised the mechanisms of spin-reorientation phase transitions (SRPT) in $TmFeO_3$ and $TbFeO_3$, resonances of AMFR modes, behaviour of anisotropy magnetic functions, defined the values of the threshold fields required for the iron spins switching, revealed signatures of cooperative phenomena such as the magnetic analogue of the Jahn-Teller effect across the SRPT in $TbFeO_3$, estimated the coupling rate between Fe and Tb subsystems and finally defined the coherence time parameter in frames of quantum optics. These findings provide a robust framework for further investigation and developments of orthoferrites in the course of antiferromagnetic spintronics.

In Chapter 5, we explored THz and light-induced spin dynamics of rare-earth low-energy states in Terbium gallium garnet ($Tb_3Ga_5O_{12}$). This crystal is representative of the family of magnetic garnet crystals, renowned for its applications in spintronics, magnonics, and optoelectronics. The objective of this chapter was to compare the effects of different excitation mechanisms on the dynamics of Tb^{3+} ions across a broad temperature range.

The work and results presented in this thesis are summarized as follows:

6.2. Theory: Results

6.2.1. THz-driven magnetic switching in rare-earth ortho-ferrites: the case of $TmFeO_3$

In Chapter 3, we developed a theoretical framework for analysing and modelling the dynamics of iron spins through the spin reorientation transition

pathway (Γ_2-Γ_{24}-Γ_4) in orthoferrites with non-Kramers ions, taking the case of $TmFeO_3$ due to the availability of experimental results. We constructed a microscopic Hamiltonian and used the mean field approximation to derive a thermodynamic potential that takes into account all relevant interactions. These interactions include *d-d* exchange, *d-f* exchange, *f-f* exchange, the interaction of the rare-earth subsystem with the crystal field, external electromagnetic fields, and thermal population effects.

For the static case, our model accurately describes the behaviour of anisotropy functions across the temperature phases Γ_2-Γ_{24}-Γ_4, aligning well with experimental observations. In the dynamic case, we were able to apply our model to fit experimental results from [151] for the AFMR modes with an excellent accuracy and to obtain the corresponding parameters for the interactions included in our model, which we then used in a numerical modelling of the iron spin switching behaviour using the LLG equations. Our numerical simulations predicted realistic values of the threshold fields required for terahertz-induced spin switching and identified different mechanisms that could lead to scenarios such as Zeeman torque and anisotropy modulation through the *R* subsystem, those are in excellent agreement with experiments from [152]. Moreover, we estimated the energy dissipation involved in the switching process and found good agreement with the experimental values from [151].

To summarise, the obtained results highlight the viability of our model for the description of the orthoferrites with non-Kramers ions in a non-equilibrium state subjected to the strong external radiation.

6.2.2. THz spin dynamics of Fe and Tb subsystems in $TbFeO_3$

Chapter 4 expands the scope of this thesis, focusing on $TbFeO_3$. Unlike $TmFeO_3$, $TbFeO_3$ has closely spaced Fe and Tb modes due to the lowest-energy quasidoublet of Tb ions, eliminating the need for the adiabatic approximation. Using a two-level approximation for the Tb subsystem, we achieved strong agreement between our experimental results from THz pump-optical probe spectroscopy measurements and our quantum-phenomenological model. We accurately aligned our experimental results for the q-FM resonant mode with theoretical predictions during the SRPT from Γ_4-Γ_{24}-Γ_2 phases. Our findings reveal that unlike in $TmFeO_3$, the q-FM mode in $TbFeO_3$ is not soft, due to repulsion from interactions with the low-frequency Tb mode. Moreover, our model successfully described the behaviour of this previously unobservable mode, identifying it as soft, and calculated all functions of the Tb subsystem depending on the order parameter of the iron spin

angle as a function of temperature $\theta(T)$. We also numerically modelled their behaviour across the Γ_4-Γ_{24}-Γ_2 phases.

In summary, our model explains the signatures of the magnetic Jahn-Teller effect by providing accurate values for the observed resonance frequencies of the magnetic modes. It effectively shows the removal of energy level degeneracy in Tb^{3+} ions and the strong coupling between Fe and Tb ions, comparing it with other strongly coupled systems as referenced in the literature [194]. Additionally, it provides a basis to estimate the coherence time parameter for $TbFeO_3$, marking it as a system with a strong coupling regime in the context of quantum optics.

6.2.3. Comparative analysis between $TmFeO_3$ and $TbFeO_3$

The obtained results for $TmFeO_3$ and $TbFeO_3$ underline an important distinction for the orthoferrites with different non-Kramers ions. In $TmFeO_3$, the dynamics between the Fe and Tm subsystems are less complex, permitting an adiabatic approach that simplifies the analysis of AFMR modes across all temperature phases. In contrast, $TbFeO_3$ requires a more complex analysis due to the strong dynamical coupling between the Fe and Tb ions, which results in changes to the magnetic symmetry of $TbFeO_3$. These differences underscore the diversity of SRPT phenomena in orthoferrites with non-Kramers ions. Despite belonging to the same subgroup (with non-Kramers ions) within the $RFeO_3$ class, they exhibit distinct properties within the same phenomenon, influenced by different non-Kramers ions.

6.3. Experimental Results

1. **Experimental setup modifications**: we have adapted the existing pump-probe experimental setup to accommodate both optical pump-optical probe and intense THz pump-optical probe spectroscopy. Additionally, our setup now supports double-pump measurements if needed. These modifications have enabled resonant excitation of magnetisation dynamics in orthoferrites and Terbium Gallium Garnet at cryogenic temperatures down to 3.4 K.
2. **THz pump-optical probe polarisation measurements**: Our THz pump-optical probe polarisation measurements of AFMR modes in $TbFeO_3$ revealed signatures of the magnetic analogue of the Jahn-Teller effect during spin-reorientation phase transitions. Our findings also include the induction of a second SRPT mediated by the ordering of Tb ions at temperatures below 3.75 K. Moreover, we observed transient high-frequency oscillations which do not correspond to any known phenomena, nor to phonon modes, requiring additional experimental and theoretical investigation.

3. **Spectroscopy Measurements in $Tb_3Ga_5O_{12}$**: We performed a THz pump-optical probe and optical pump-optical probe spectroscopy measurements on $Tb_3Ga_5O_{12}$ to study the induced magnetisation of Tb spins. Our findings show that, while the frequency associated with the crystal field mode was observable in both cases, the behaviour under the influence of a 400 nm pump pulse can be explained using the Boltzmann distribution function for a two-level system of the Tb^{3+} ions ensemble. In contrast, the results from THz impulsive excitation require a more sophisticated theoretical analysis.

6.4. Outlook

In this section of the thesis, we provide an outlook for the potential further extensions of the presented research, from theoretical and experimental perspectives.

Theoretical perspective.

Within the existing theoretical framework for non-Kramers ions:

1. The developed theoretical model shows potential for application to other orthoferrites with non-Kramers ions and available experimental data like $HoFeO_3$. It also aims to be extended to incorporate scenarios involving the 2nd SRPT mediated by the ordering of Tb ions in $TbFeO_3$.
2. It is of interest to model the behaviour of iron spin switching during the SRPT in $TbFeO_3$, estimate threshold fields, and compare them with those from $TmFeO_3$.
3. While our current model provides a robust foundation for the orthoferrites with non-Kramers ions, it also shows potential for extension to orthoferrites with Kramers ions like Erbium ($ErFeO_3$) and Ytterbium ($YbFeO_3$) to describe both static and dynamic properties across SRPT. As the $ErFeO_3$ shows similar features to $TmFeO_3$ in terms of the SRPT and $YbFeO_3$ might exhibit the magnetic analogue of the Jahn-Teller effect similarly to $TbFeO_3$. It is also interesting to estimate the spin-switching mechanisms in these orthoferrites.
4. In the case of $Tb_3Ga_5O_{12}$ a more sophisticated model is required to describe the crystal field mode as a function of temperature under the influence of intense THz excitation.

Experimental perspective.

Throughout our work, we managed to distinctly observe only AFMR modes but no signatures of Tb modes in $TbFeO_3$. This is likely due to the fact that the THz pump pulse does not excites this mode effectively, as its spectrum is well tuned to the AFMR modes frequency range or/and the wavelength of the probe pulse is

insensitive. It might be reasonable to perform additional series of THz pump, but with a varying probe wavelength measurements which could be done with the existing setup complemented by an optical parametric amplifier (OPA).

Furthermore, there is still uncertainty regarding fast and short-lived (3-5 ps) dynamic modes of unknown nature observed in $TbFeO_3$. They do not correspond to any known magnetic or phonon modes. Given this, it makes sense to apply pump pulse with a different wavelength, like 400 nm, as a first step. However, on the experimental side, advancements in ultrafast spectroscopy techniques are offering exciting opportunities. For example, combining THz pump-probe setups with ultrafast X-ray or neutron scattering could provide new insights into spin-lattice coupling.

References

[1] Y. Yang, *Magnetic Materials in China*, in *Proc. 3rd Int. Conf. on Physics of Magnetic Materials* (1986), pp. 4–14.

[2] J. Needham, *Science and Civilisation in China* (Cambridge University Press, 1974).

[3] Dress A.A., *Iron in Ancient India*, Nature **94**, 520 (1915).

[4] Aristotle, *De Anima* (n.d.).

[5] L. Carus, *De Rerum Natura VI* (Aris & Phillips Ltd, 1991).

[6] L. Shu-hua, *Origine de La Boussole 11. Aimant et Boussole*, Isis **45**, (1954).

[7] Al-Ashraf, *Nayz Al-Azyz* (1282).

[8] P. P., *Epistola de Magnete* (1269).

[9] W. . Gilbert, *De Magnete*. (London, 1600).

[10] Descartes Rene, *Principia Philosophiae* (1644).

[11] Aepinus Franz, *Tentamen Theoriae Electricitatis et Magnetismi* (St. Petersburg, 1759).

[12] C. A. Coulomb, *Premier Mémoire Sur l'électricité et Le Magnétisme*, in *Histoire de l'Académie Royale Des Sciences* (1785), pp. 569–577.

[13] Poisson S. D., *Mémoire Sur La Théorie Du Magnétisme*, in *Mémoires de l'Académie Royale Des Sciences* (1824).

[14] Ørsted H. C., *Selected Scientific Works of Hans Christian Ørsted* (Princeton University Press, Princeton, 2014).

[15] Faraday M, *Experimental Researches In Electricity* (Read Books Ltd, 2016).

[16] Maxwell J C, *A Treatise on Electricity and Magnetism* (Clarendon press, 1881).

[17] J. J. Thomson, *Cathode Rays*, Philos. Mag. **44**, 293 (1897).

[18] Lorentz H. A., *Zeeman Effect*, in *Versl. Kon. Akad.* (1896).

[19] P. Curie, *Propriétés Magnétiques Des Corps a Diverses Températures.*, Vol. 4 (Gauthier-Villars et fils, 1895).

[20] P. Langevin, *Magnetisme et Theorie Deselectrons*, Ann. Chim. Phys. **5**, 70 (1905).

[21] P. Weiss, *L'hypothèse Du Champ Moléculaire et La Propriété Ferromagnétique*, J. Phys. Theor. Appl. **6**, 661 (1907).

[22] O. Gerlach, W.; Stern, *Der Experimentelle Nachweis Der Richtungsquantelung Im Magnetfeld*, Zeitschrift Für Phys. **9**, 349 (1922).

[23] P. W., *Über Gasentartung Und Paramagnetismus*, Zeitschrift Für Phys. A Hadron. Nucl. 81 (1927).

[24] P. A. M. Dirac, *The Quantum Theory of the Electron*, Proc. R. Soc. A **117**, (1928).

[25] F.Bloch, *Zur Theorie Des Ferromagnetismus. II*, Zeitschrift Für Phys. **61**, 206 (1930).

[26] Louis NÉEL, *Propriétés Magnétiques Des Ferrites Ferrimagnétisme Et Antiferromagnétisme*, Ann. Phys. (Paris). **3**, 137 (1948).

[27] J. C. Slater, *The Theory of Ferromagnetism: Lowest Energy Levels*, Phys. Rev. **52**, (1937).

[28] H. Barkhausen, *Zwei Mit Hilfe Der Neuen Verstärker Entdeckte Erscheinungen*, Phys. Zeitschrift **20**, 401 (1919).

[29] A. A. Thiele, *The Theory of Cylindrical Magnetic Domains*, Bell Syst. Tech. J. **48**, 3287 (1969).

[30] A. H. Bobeck, *Properties and Device Applications of Magnetic Domains in Orthoferrites*, Bell Syst. Tech. J. **46**, 1901 (1967).

[31] J. Friedel, *On Some Electrical and Magnetic Properties of Metallic Solid Solutions*, Can. J. Phys. 1190 (1956).

[32] P. W. Anderson, *Localized Magnetic States in Metals*, Phys. Rev. **124**, (1961).

[33] J. Kondo, *Resistance Minimum in Dilute Magnetic Alloys Downloaded From*, Prog. Theor. Phys. **32**, 37 (1964).

[34] K. G. Wilson, *The Renormalization Group: Critical Phenomena and the Kondo Problem*, Rev. Mod. Phys. **47**, 773 (1975).

[35] N. Andrei, *Diagonalization of the Kondo Hamiltonian*, Phys. Rev. Lett. **45**, 379 (1980).

[36] N. D. Mermin and H. Wagner, *Absence of Ferromagnetism or Antiferromagnetism in One- or Two-Dimensional Isotropic Heisenberg*

Models, Phys. Rev. Lett. **17**, 1133 (1966).

[37] J. M. Kosterlitz and D. J. Thouless, *Ordering, Metastability and Phase Transitions in Two-Dimensional Systems*, J. Phys. C Solid State Phys. **6**, 1181 (1973).

[38] M. K. A. Bednorz J.G., *Possible High Tc Superconductivity in the Ba - La-Cu-0 System*, Z. Phys. B - Condens. Matte **64**, 189 (1986).

[39] J. R. S. J. Bardeen, L. N. Cooper, *Theory of Superconductivity*, Phys. Rev. **108**, 1 (1957).

[40] M. N. Baibich, J. M. Broto, A. Fert, F. N. Van Dau, F. Petroff, P. Eitenne, G. Creuzet, A. Friederich, and J. Chazelas, *Giant Magnetoresistance of (001)Fe/(001)Cr Magnetic Superlattices*, Phys. Rev. Lett. **61**, 2472 (1988).

[41] B. R. B. Frankel Dennis A., *Magnetosome Formation in Prokaryotes*, Nat. Rev. Microbiol. **2**, 217 (2004).

[42] D. H. Vine, F.J. and Matthews, *Magnetic Anomalies over Oceanic Ridges. Nature*, 947 (1963).

[43] Vincent G. Harris, *Modern Ferrites* (2022).

[44] X. Kang, Y. Gao, L. Liu, W. Chen, and X. Zhao, *Enhanced Magnetic Modulation in NiO-Based Memory Device through Ionic Liquid Pre-Treatment*, Appl. Phys. Lett. **115**, 1 (2019).

[45] Benedetta Flebus et al, *The 2024 Magnonics Roadmap*, J. Phys. Condens. Matter **36**, 41 (2024).

[46] L. Landau and E. Lifshitz, *"On the Theory of the Dispersion of Magnetic Permeability in Ferromagnetic Bodies,"* Phys. Z. Sowjetunion **8**, (1935).

[47] L. Landau and E. Lifshitz, *"On the Theory of the Dispersion of Magnetic Permeability in Ferromagnetic Bodies,"* in *Elsevier* (1992), pp. 51–65.

[48] D. Strickland and G. Morou, *Compression of Amplified Chirped Optical Pulses*, Opt. Commun. **55**, 447 (1985).

[49] E. Beaurepaire, J. C. Merle, A. Daunois, and J. Y. Bigot, *Ultrafast Spin Dynamics in Ferromagnetic Nickel*, Phys. Rev. Lett. **76**, 4250 (1996).

[50] A. Kirilyuk, A. V. Kimel, and T. Rasing, *Ultrafast Optical Manipulation of Magnetic Order*, Rev. Mod. Phys. **82**, 2731 (2010).

[51] Finja Tietjen, R. Matthias Geilhufe, *Ultrafast Entropy Production in Non-*

Equilibrium Magnets, ArXiv:2410.23205 (2024).

[52] M. Pankratova, I. P. Miranda, D. Thonig, M. Pereiro, E. Sjöqvist, A. Delin, O. Eriksson, and A. Bergman, *Heat-Conserving Three-Temperature Model for Ultrafast Demagnetization in Nickel*, Phys. Rev. B **106**, 1 (2022).

[53] C. B. Deeksha Gupta, Maryna Pankratova, Matthias Riepp, Manuel Pereiro, Biplab Sanyal, Soheil Ershadrad, Michel Hehn, Niko Pontius, Christian Schüßler-Langeheine, Radu Abrudan, Nicolas Bergeard, Anders Bergman, Olle Eriksson, *Tuning of the Ultrafast Demagnetization by Ultrashort Spin Polarized Currents in Multi-Sublattice Ferrimagnets*, ArXiv:2403.11739 (2024).

[54] A. Lentfert, A. De, L. Scheuer, B. Stadtmuller, G. von Freymann, M. Aeschlimann, and P. Pirro, *Phase Shift of Coherent Magnetization Dynamics after Ultrafast Demagnetization in Strongly Quenched Nickel Thin Films*, J. Phys. Condens. Matter **36**, (2024).

[55] A. V. Kimel and M. Li, *Writing Magnetic Memory with Ultrashort Light Pulses*, Nat. Rev. Mater. **4**, 189 (2019).

[56] J. W. M. Kohlmann, L. Vollroth, K. Jäckel, K. Hovorakova, E. Schmoranzerova, K. Carva, D. Hinzke, U. Nowak, M. Münzenberg, *Exploring the Impact of the Inverse Faraday Effect on All-Optical Helicity-Dependent Magnetization Switching*, ArXiv:2401.18010 (2024).

[57] B. Assouline and A. Capua, *Helicity-Dependent Optical Control of the Magnetization State Emerging from the Landau-Lifshitz-Gilbert Equation*, Phys. Rev. Res. **6**, (2024).

[58] H. W. Ryunosuke Takahashi, Yann Le Guen, Suguru Nakata, Junta Igarashi, Julius Hohlfeld, Grégory Malinowski, Xie Lingling, Kan Daisuke, Yuichi Shimakawa, Stéphane Mangin, *All-Optical Helicity-Dependent Switching in NiCo2O4 Thin Films*, ArXiv:2409.01615 (2024).

[59] F. Steinbach et al., *Exploring the Fundamental Spatial Limits of Magnetic All-Optical Switching*, Nano Lett. **24**, 6865 (2024).

[60] W. Hübner, G. Lefkidis, and G. P. Zhang, *All-Optical Spin Switching on an Ultrafast Time Scale*, J. Phys. Condens. Matter **36**, (2024).

[61] Y. Xu, M. Deb, G. Malinowski, M. Hehn, W. Zhao, and S. Mangin, *Ultrafast Magnetization Manipulation Using Single Femtosecond Light and Hot-Electron Pulses*, Adv. Mater. **29**, 1 (2017).

[62] S. Bhattacharjee and S. C. Lee, *Magnetization Dynamics in Skyrmions Due to High-Speed Carrier Injections from Dirac Half-Metals*, J. Phys. Condens. Matter **36**, (2024).

[63] M. Ma, Z. Li, X. Ruan, J. Wu, R. Wang, T. Liu, J. Du, X. Lu, and Y. Xu, *Manipulation of Magnetization Switching by Ultrafast Spin-Polarized Hot-Electron Transport in Synthetic Antiferromagnet*, Adv. Electron. Mater. **9**, (2023).

[64] A. Stupakiewicz, K. Szerenos, D. Afanasiev, A. Kirilyuk, and A. V. Kimel, *Ultrafast Nonthermal Photo-Magnetic Recording in a Transparent Medium*, Nature **542**, 71 (2017).

[65] A. De La Torre, D. M. Kennes, M. Claassen, S. Gerber, J. W. McIver, and M. A. Sentef, *Colloquium: Nonthermal Pathways to Ultrafast Control in Quantum Materials*, Rev. Mod. Phys. **93**, 41002 (2021).

[66] J. Shi et al., *Nonthermal Ultrafast Optical Control of Magnetization Dynamics by Linearly Polarized Light in Metallic Ferromagnet*, Adv. Sci. **10**, 1 (2023).

[67] H. Jang et al., *4D Visualization of a Nonthermal Coherent Magnon in a Laser Heated Lattice by an X-Ray Free Electron Laser*, Adv. Mater. **35**, (2023).

[68] H. Hedayat, C. J. Sayers, A. Ceraso, J. van Wezel, S. R. Clark, C. Dallera, G. Cerullo, E. da Como, and E. Carpene, *Investigation of the Non-Equilibrium State of Strongly Correlated Materials by Complementary Ultrafast Spectroscopy Techniques*, New J. Phys. **23**, (2021).

[69] P. Němec, M. Fiebig, T. Kampfrath, and A. V. Kimel, *Antiferromagnetic Opto-Spintronics*, Nat. Phys. **14**, 229 (2018).

[70] S. Shim, M. Mehraeen, J. Sklenar, S. S.-L. Zhang, A. Hoffmann, and N. Mason, *Spin-Polarized Antiferromagnetic Metals*, Annu. Rev. Condens. Matter Phys. 103 (2024).

[71] A. Dal Din, O. J. Amin, P. Wadley, and K. W. Edmonds, *Antiferromagnetic Spintronics and Beyond*, Npj Spintron. **2**, 1 (2024).

[72] D.-F. Shao and E. Y. Tsymbal, *Antiferromagnetic Tunnel Junctions for Spintronics*, Npj Spintron. **2**, (2024).

[73] S. V. Vonsovskyi, *Magnetism* (Moskow Sci., Moscow, 1984).

[74] R. M. White, *Quantum Theory of Magnetism*, 3rd ed. (Springer, New York, 2006).

[75] S. Blundell, *Magnetism in Condensed Matter* (Oxford University Press, New York, 2001).

[76] I. Dzyaloshinsky, *A Thermodynamic Theory of "Weak" Ferromagnetism of Antiferromagnetics*, J. Phys. Chem. Solids **4**, 241 (1958).

[77] T. Moriya, *Anisotropic Superexchange Interaction and Weak Ferromagnetism*, Phys. Rev. **120**, 91 (1960).

[78] R. V. Mikhaylovskiy et al., *Ultrafast Optical Modification of Exchange Interactions in Iron Oxides*, Nat. Commun. **6**, 8190 (2015).

[79] L. D. Landau, *On the Theory of Phase Transitions*, Zh. Eksp. Teor. Fiz. 19 (1937).

[80] L. D. Landau & E. M. Lifshitz, *Statistical Physics, Part 1*, Pergamon (1980).

[81] D. I. Khomskii, *Basic Aspects of the Quantum Theory of Solids: Order And Elementary Excitations* (Cambridge Univ. Press, 2010).

[82] R. A. Cowley, *Structural Phase Transitions I. Landau Theory*, Adv. Phys. **29**, 1 (1980).

[83] K. P. Belov, A. K. Zvezdin, A. M. Kadomtseva, and R. Z. Levitin, *Spin-Reorientation Transitions in Rare-Earth Magnets*, Uspekhi Fiz. Nauk **119**, 447 (1976).

[84] A. Moskvin, E. Vasinovich, and A. Shadrin, *Simple Realistic Model of Spin Reorientation in 4f-3d Compounds*, Magnetochemistry **8**, 1 (2022).

[85] A. K. Zvezdin and V. A. Kotov, *Modern Magnetooptics and Magnetooptical Materials* (IOP Publishing Ltd, Bristol and Philadelphia, 1997).

[86] R. S. Singh and P. K. Sarswat, *From Fundamentals to Applications: The Development of Magnetoplasmonics for next-Generation Technologies*, Mater. Today Electron. **4**, (2023).

[87] A. Stupakiewicz, A. Chizhik, A. Zhukov, M. Ipatov, J. Gonzalez, and I. Razdolski, *Ultrafast Magnetization Dynamics in Metallic Amorphous Ribbons with a Giant Magnetoimpedance Response*, Phys. Rev. Appl. **13**, 1 (2020).

[88] T. Hioki, Y. Hashimoto, T. H. Johansen, and E. Saitoh, *Time-Resolved Imaging of Magnetoelastic Waves by the Cotton-Mouton Effect*, Phys. Rev. Appl. **11**, 1 (2019).

[89] Y. Z. Yexin Jiang, Zhangshun Li, Zhuoyi Li, Zuanming Jin, Xianyang Lu,

Yongbing Xu, Yan Peng, *"Ultrafast Light-Driven Magneto-Optical Nonlinearity in Ferromagnetic Heterostructures,"* Opt. Lett. **48**, 2054 (2023).

[90] J. Jang, J. Park, and H. J. Shin, *Terahertz Spectral Analysis: An in-Depth Exploration of Spectroscopy Approaches for Ultrafast Dynamics*, Curr. Appl. Phys. **59**, 197 (2024).

[91] J. Lai and Y. Yang, *3D Terahertz Antenna Measurement: A Comparison between Solid-State Electronics and Photomixing Approaches*, IEEE Antennas Propag. Mag. **66**, 37 (2024).

[92] A. Leitenstorfer, A. S. Moskalenko, T. Kampfrath, J. Kono, E. Castro-camus, K. Peng, N. Qureshi, and D. Turchinovich, *The 2023 Terahertz Science and Technology Roadmap*, J. Phys. D Appl. Phys. **56**, (2023).

[93] J. H. Scofield, *"Frequency - Domain Description of a Lock - in Amplifier,"* **62**, 129 (1994).

[94] G. Tóth, G. Polónyi, and J. Hebling, *Tilted Pulse Front Pumping Techniques for Efficient Terahertz Pulse Generation*, Light Sci. Appl. **12**, 1 (2023).

[95] T. Taniuchi and H. Nakanishi, *Collinear Phase-Matched Terahertz-Wave Generation in GaP Crystal Using a Dual-Wavelength Optical Parametric Oscillator*, J. Appl. Phys. **95**, 7588 (2004).

[96] J. Hebling, G. Almasi, I. Kozma, and J. Kuhl, *Velocity Matching by Pulse Front Tilting for Large Area THz-Pulse Generation*, Opt. Express **10**, 1161 (2002).

[97] J. Hebling, A. G. Stepanov, G. Almási, B. Bartal, and J. Kuhl, *Tunable THz Pulse Generation by Optical Rectification of Ultrashort Laser Pulses with Tilted Pulse Fronts*, Appl. Phys. B Lasers Opt. **78**, 593 (2004).

[98] L. Tokodi, J. Hebling, and L. Pálfalvi, *Optimization of the Tilted-Pulse-Front Terahertz Excitation Setup Containing Telescope*, J. Infrared, Millimeter, Terahertz Waves **38**, 22 (2017).

[99] L. S. Pedrotti, F.L., Pedrotti, L.M. and Pedrotti, *Introduction to Optics* (2018).

[100] B. Wu, L. Cao, Q. Fu, P. Tan, Y. Xiong, et al., *Comparison of the Detection Performance of Three Nonlinear Crystals for the Electro-Optic Sampling of a FEL-THz Source*, in *Proceedings of the 5th International Particle Accelerator Conference* (2014), pp. 2891–2893.

[101] R. L. White, *Review of Recent Work on the Magnetic and Spectroscopic*

Properties of the Rare-Earth Orthoferrites, J. Appl. Phys. **40**, 1061 (1969).

[102] R. M. Bozorth, H. J. Williams, and D. E. Walsh, *Magnetic Properties of Some Orthoferrites and Cyanides at Low Temperatures*, Phys. Rev. **103**, 572 (1956).

[103] G. S. Krinchik and M. V. Chetkin, *Transparent Ferromagnets*, Usp. Fiz. Nauk. **98**, (1969).

[104] K. P. Belov, A. M. Kadomtseva, and R. Z. Levitin, *On the Nature of the Magnetization Curves of a Single Crystal of Samarium Orthoferrite near the Reorientation Temperature*, Sov. Phys. JETP **24**, 878 (1967).

[105] R. C. LeCraw, R. Wolfe, E. M. Gyorgy, F. B. Hagedorn, J. C. Hensel, and J. P. Remeika, *Microwave Absorption near the Reorientation Temperature in Rare Earth Orthoferrites*, J. Appl. Phys. **39**, 1019 (1968).

[106] H. Horner and C. M. Varma, *Nature of Spin-Reorientation Transitions*, Phys. Rev. Lett. **20**, 845 (1968).

[107] K.P. Belov, A.M. Kadomtseva, R.Z. Levitin, V.A. Timofeeva, *Reorientation of the Antiferromagnetic Vector of Some Rare-Earth Orthoferrites in Strong Magnetic Fields*, Zh. Eksp. Teor. Fiz. **28**, 2151 (1969).

[108] K. P. Belov, A. K. Zvezdin, and A. A. Mukhin, *Magnetic Phase Transitions in Terbium Orthoferrite*, Zh. Eksp. Teor. Fiz. **49**, (1979).

[109] G. P. Vorob'ev, A. M. Kadomtseva, I. B. Krynetkii, and A. A. Mukhin, *Unusual Nature of Spin Reorientation in HoFeO3*, Sov. Phys. JETP **68**, 629 (1989).

[110] Sergey Artyukhin, Maxim Mostovoy, Niels Paduraru Jensen, Duc Le, Karel Prokes, Vinícius G. de Paula, Heloisa N. Bordallo, Andrey Maljuk, Sven Landsgesell, Hanjo Ryll, et al., *Solitonic Lattice and Yukawa Forces in the Rare-Earth Orthoferrite TbFeO3*, Nat. Mater. **11**, 694 (2012).

[111] F. J. Kahn, P. S. Pershan, and J. P. Remeika, *Ultraviolet Magneto-Optical Properties of Single-Crystal Orthoferrites, Garnets, and Other Ferric Oxide Compounds*, Phys. Rev. **186**, 891 (1969).

[112] H. Schuchert, S. Hüfner, and R. Faulhaber, *Optical Investigation of DyFeO3*, Zeitschrift Für Phys. **220**, 273 (1969).

[113] S. L. Gnatchenko, N. F. Kharchenko, P. P. Lebedev, K. Piotrowski, H. Szymczak, and R. Szymczak, *Magneto-Optical Studies of H-T Phase Diagram for DyFeO3 (H ∥ A)*, J. Magn. Magn. Mater. **81**, 125 (1989).

[114] N. Singh, J. Y. Rhee, and S. Auluck, *Electronic and Magneto-Optical Properties of Rare-Earth Orthoferrites RFeO3 (R = Y, Sm, Eu, Gd and Lu)*, J. Korean Phys. Soc. **53**, 806 (2008).

[115] A. M. Balbashov, A. A. Volkov, S. P. Lebedev, A. A. Mukhin, A. S. Prokhorov, *High-Frequency Magnetic Properties of Dysprosium Orthoferrite*, Zh. Eksp. Teor. Fiz **88**, 974 (1985).

[116] A. M. Balbashov, G.V. Kozlov, S. P. Lebedev, A. A. Mukhin, A. Yu. Pronin, and A. S. Prokhorov, *Anomalies of High-Frequency Magnetic Properties and New Orientational Transitions in HoFeO3*, Sov. Phys. JETP **68**, 629 (1989).

[117] S. Venugopalan, M. Dutta, A. K. Ramdas, and J. P. Remeika, *Rare-Earth Orthoferrites:*, Phys. Rev. B - Condens. Matter Mater. Phys. **31**, 1490 (1985).

[118] N Koshizuka and K Hayashi, *Raman Scattering from Magnon Excitations in RFeO3*, J. Phys. Soc. Japan **57**, 4418 (1988).

[119] S. Gupta, R. Medwal, S. P. Pavunny, D. Sanchez, and R. S. Katiyar, *Temperature Dependent Raman Scattering and Electronic Transitions in Rare Earth SmFeO3*, Ceram. Int. **44**, 4198 (2018).

[120] A. S. P. A. M. Balbashov, G. V. Kozlov, A. A. Mukhin, *Submillimeter Spectroscopy of Antiferromagnetic Dielectrics: Rare-Earth Orthoferrites*, in *High Frequency Processes in Magnetic Materials* (World Scientific, Singapore, 1995), pp. 56–98.

[121] C. Huang, L. Luo, M. Mootz, J. Shang, P. Man, L. Su, I. E. Perakis, Y. X. Yao, A. Wu, and J. Wang, *Extreme Terahertz Magnon Multiplication Induced by Resonant Magnetic Pulse Pairs*, Nat. Commun. **15**, 1 (2024).

[122] V. G. Bar'Yakhtar, B. A. Ivanov, and M. V. Chetkin, *Dynamics of Domain Walls in Weak Ferromagnets*, Sov. Phys. - Uspekhi **28**, 563 (1985).

[123] K.P.Belov, A.M.Kadomtseva, S.A.Medvedev, V.V.Uskov, A.Ya. Chervonenkis, *Anomalies in the Temperature Dependence of the Modulus of Elasticity during the Spontaneous Reorientation of Spins in Rare-Earth Orthoferrites*, Zh. Eksp. Teor. Fiz. **57**, 1124 (1969).

[124] V. D. Buchel'nikov, I. V Bychkov, and V. G. Shavrov, *Coupled Oscillations of Iron Rare-Earth and Elastic Subsystems in Orthoferrites with Kramers Rare-Earth Ions*, Zh. Eksp. Teor. Fiz. **101**, 1869 (1992).

[125] V. D. Buchel'nikov, N. K. Dan'shin, L. T. Tsymbal, and V. G. Shavrov, *Magnetoacoustics of Rare-Earth Orthoferrites*, Physics-Uspekhi **39**, 547

(1996).

[126] Y. Tokunaga, Y. Taguchi, T. Arima, and Y. Tokura, *Magnetic Biasing of a Ferroelectric Hysteresis Loop in a Multiferroic Orthoferrite*, Phys. Rev. Lett. **112**, 1 (2014).

[127] Y. Du, Z. X. Cheng, X. L. Wang, and S. X. Dou, *Lanthanum Doped Multiferroic DyFeO3: Structural and Magnetic Properties*, J. Appl. Phys. **107**, 317 (2010).

[128] J. H. Lee, Y. K. Jeong, J. H. Park, M. A. Oak, H. M. Jang, J. Y. Son, and J. F. Scott, *Spin-Canting-Induced Improper Ferroelectricity and Spontaneous Magnetization Reversal in SmFeO3*, Phys. Rev. Lett. **107**, 1 (2011).

[129] Z. Cheng, F. Hong, Y. Wang, K. Ozawa, H. Fujii, H. Kimura, Y. Du, X. Wang, and S. Dou, *Interface Strain-Induced Multiferroicity in a SmFeO 3 Film*, (2014).

[130] X. Li et al., *Observation of Dicke Cooperativity in Magnetic Interactions*, Science (80-.). **361**, 794 (2018).

[131] Takuma Makihara, Kenji Hayashida, G. Timothy Noe II, Xinwei Li, Nicolas Marquez Peraca, Xiaoxuan Ma, Zuanming Jin, Wei Ren, Guohong Ma, Ikufumi Katayama, et al., *Ultrastrong Magnon–Magnon Coupling Dominated by Antiresonant Interactions*, Nat. Commun. **12**, 1 (2021).

[132] M. Bamba, X. Li, N. Marquez Peraca, and J. Kono, *Magnonic Superradiant Phase Transition*, Commun. Phys. **5**, (2022).

[133] Nicolas Marquez Peraca, Xinwei Li, Jaime M. Moya, Kenji Hayashida, Dasom Kim, Xiaoxuan Ma, Kelly J. Neubauer, Diego Fallas Padilla, Chien-Lung Huang, Pengcheng Dai, et al., *Quantum Simulation of an Extended Dicke Model with a Magnetic Solid*, Commun. Mater. **5**, 1 (2024).

[134] A. V. Kimel, A. Kirilyuk, P. A. Usachev, R. V. Pisarev, A. M. Balbashov, and T. Rasing, *Ultrafast Non-Thermal Control of Magnetization by Instantaneous Photomagnetic Pulses*, Nature **435**, (2005).

[135] A. V. Kimel, A. Kirilyuk, A. Tsvetkov, R. V. Pisarev, and T. Rasing, *Laser-Induced Ultrafast Spin Reorientation in the Antiferromagnet TmFeO3*, Nature **429**, 850 (2004).

[136] J. A. De Jong, A. V. Kimel, R. V. Pisarev, A. Kirilyuk, and T. Rasing, *Laser-Induced Ultrafast Spin Dynamics in ErFeO3*, Phys. Rev. B - Condens. Matter Mater. Phys. **84**, 1 (2011).

[137] D. M. Juraschek, M. Fechner, and N. A. Spaldin, *Ultrafast Structure Switching through Nonlinear Phononics*, Phys. Rev. Lett. **118**, 1 (2017).

[138] T. F. Nova, A. Cartella, A. Cantaluppi, M. Först, D. Bossini, R. V. Mikhaylovskiy, A. V. Kimel, R. Merlin, and A. Cavalleri, *An Effective Magnetic Field from Optically Driven Phonons*, Nat. Phys. **13**, 132 (2017).

[139] D. Afanasiev, J. R. Hortensius, B. A. Ivanov, A. Sasani, E. Bousquet, Y. M. Blanter, R. V. Mikhaylovskiy, A. V. Kimel, and A. D. Caviglia, *Ultrafast Control of Magnetic Interactions via Light-Driven Phonons*, Nat. Mater. **20**, 607 (2021).

[140] J. B. Curtis, A. Disa, M. Fechner, A. Cavalleri, and P. Narang, *Dynamics of Photoinduced Ferromagnetism in Oxides with Orbital Degeneracy*, Phys. Rev. Res. **5**, 84 (2023).

[141] J. R. Hortensius, D. Afanasiev, M. Matthiesen, R. Leenders, R. Citro, A. V Kimel, R. V Mikhaylovskiy, B. A. Ivanov, and A. D. Caviglia, *Coherent Spin-Wave Transport in an Antiferromagnet*, Nat. Phys. **17**, (2021).

[142] R. A. Leenders, D. Afanasiev, A. V Kimel, and R. V Mikhaylovskiy, *Canted Spin Order as a Platform for Ultrafast Conversion of Magnons*, Nature **630**, (2024).

[143] R.A. Leenders and R.V. Mikhaylovskiy, *Theory of Optical Generation and Detection of Propagating Magnons in an Antiferromagnet*, Phys. Rev. B **094423**, 1 (2023).

[144] T. Kampfrath, A. Sell, G. Klatt, A. Pashkin, S. Mährlein, T. Dekorsy, M. Wolf, M. Fiebig, A. Leitenstorfer, and R. Huber, *Coherent Terahertz Control of Antiferromagnetic Spin Waves*, Nat. Photonics **5**, 31 (2011).

[145] J. Lu, X. Li, H. Y. Hwang, B. K. Ofori-Okai, T. Kurihara, T. Suemoto, and K. A. Nelson, *Coherent Two-Dimensional Terahertz Magnetic Resonance Spectroscopy of Collective Spin Waves*, Phys. Rev. Lett. **118**, 1 (2017).

[146] Ruslan Salikhov, Igor Ilyakov, Lukas Körber, Attila Kákay, Rodolfo A. Gallardo, Alexey Ponomaryov, Jan-Christoph Deinert, Thales V. A. G. de Oliveira, Kilian Lenz, Jürgen Fassbender, et al., *Coupling of Terahertz Light with Nanometre-Wavelength Magnon Modes via Spin–Orbit Torque*, Nat. Phys. **19**, 529 (2023).

[147] M. Pancaldi, P. Vavassori, and S. Bonetti, *Terahertz Metamaterials for Light-Driven Magnetism*, Nanophotonics **13**, 1891 (2024).

[148] Zhuquan Zhang, Frank Y. Gao, Jonathan B. Curtis, Zi-Jie Liu, Yu-Che Chien, Alexander von Hoegen, Man Tou Wong, Takayuki Kurihara, Tohru Suemoto, Prineha Narang, et al., *Terahertz Field-Induced Nonlinear Coupling of Two Magnon Modes in an Antiferromagnet*, Nat. Phys. 2024 801 (2024).

[149] Zhuquan Zhang, Frank Y. Gao, Yu-Che Chien, Zi-Jie Liu, Jonathan B. Curtis, Eric R. Sung, Xiaoxuan Ma, Wei Ren, Shixun Cao, Prineha Narang, et al., *Terahertz-Field-Driven Magnon Upconversion in an Antiferromagnet*, Nat. Phys. **20**, 788 (2024).

[150] G. Fitzky, M. Nakajima, Y. Koike, A. Leitenstorfer, and T. Kurihara, *Ultrafast Control of Magnetic Anisotropy by Resonant Excitation of 4f Electrons and Phonons in Sm0.7Er0.3FeO3*, Phys. Rev. Lett. **127**, 107401 (2021).

[151] S. Baierl, M. Hohenleutner, T. Kampfrath, A. K. Zvezdin, A. V. Kimel, R. Huber, and R. V. Mikhaylovskiy, *Nonlinear Spin Control by Terahertz-Driven Anisotropy Fields*, Nat. Photonics **10**, 715 (2016).

[152] S. Schlauderer, C. Lange, S. Baierl, T. Ebnet, C. P. Schmid, D. C. Valovcin, A. K. Zvezdin, A. V. Kimel, R. V. Mikhaylovskiy, and R. Huber, *Temporal and Spectral Fingerprints of Ultrafast All-Coherent Spin Switching*, Nature **569**, 383 (2019).

[153] A. K. Zvezdin, V. M. Matveev, A. A. Mukhin, and A. I. Popov, *Rare-Earth Ions in Magnetically Ordered Crystals*, Nauka (Moscow, 1985).

[154] D. Amoroso, B. Dupé, and M. J. Verstraete, *Unraveling the Role of Sm 4f Electrons in the Magnetism of SmFeO3*, Phys. Rev. B **107**, 1 (2023).

[155] Mads C. Weber, Mael Guennou, Donald M. Evans, Constance Toulouse, Arkadiy Simonov, Yevheniia Kholina, Xiaoxuan Ma, Wei Ren, Shixun Cao, Michael A. Carpenter, et al., *Emerging Spin–Phonon Coupling through Cross-Talk of Two Magnetic Sublattices*, Nat. Commun. **13**, 1 (2022).

[156] I. Fita, R. Puzniak, E. E. Zubov, P. Iwanowski, and A. Wisniewski, *Temperature-Driven Spin Switching and Exchange Bias in the ErFeO3 Ferrimagnet*, Phys. Rev. B **105**, 1 (2022).

[157] E. E. Zubov, I. Fita, R. Puzniak, and A. Wisniewski, *Microscopic Description of Magnetic Nonequilibrium Phenomena in Erbium Orthoferrite*, Phys. Rev. B **107**, 1 (2023).

[158] E. E. Zubov, I. Fita, R. Puzniak, and A. Wisniewski, *Spin-Reorientation Phase Transition and Induced Spin Reversals in NdFe O3: Theory and*

Experiment, Phys. Rev. B **110**, 1 (2024).

[159] A. I. Popov, K. A. Zvezdin, Z. V. Gareeva, A. V. Kimel, and A. K. Zvezdin, *Quantum Theory of Femtosecond Optomagnetic Effects for Rare-Earth Ions in DyFeO3*, Phys. Rev. B **103**, 1 (2021).

[160] A. I. Popov, Z. V. Gareeva, and A. K. Zvezdin, *Quantum Theory of the Spin Dynamics Excited by Ultrashort THz Laser Pulses in Rare Earth Antiferromagnets. DyFeO3*, J. Phys. Condens. Matter **37**, 1 (2024).

[161] S. Geller and E. A. Wood, *Crystallographic Studies of Perovskite-like Compounds. I. Rare Earth Orthoferrites and YFeO 3 , YCrO 3 , YAlO 3*, Acta Crystallogr. **9**, 563 (1956).

[162] M. Marezio, J. P. Remeika, and P. D. Dernier, *The Crystal Chemistry of the Rare Earth Orthoferrites*, Acta Crystallogr. Sect. B Struct. Crystallogr. Cryst. Chem. **26**, 2008 (1970).

[163] V. E. Naish and E. A. Turov, *Physical Properties of Magnetically Ordered Crystals*. (1965).

[164] D. Treves, *Studies on Orthoferrites at the Weizmann Institute of Science*, J. Appl. Phys. **36**, 1033 (1965).

[165] X. Li, D. Kim, Y. Liu, and J. Kono, *Terahertz Spin Dynamics in Rare-Earth Orthoferrites*, Photonics Insights **1**, R05 (2022).

[166] A. S. Moskvin and E. V. Sinitsyn, *Antisymmetrical Exchange and Four-Sublattice Model in Orthoferrites*, Fiz. Tverd. Tela **17**, (1975).

[167] K. P. Belov, A. K. Zvezdin, A. M. Kadomtseva, I.B. Krynetskii and A.A.Mukhin, *Metamagnetic Phase Transitions and Instability of Magnetic Structure in Rare-Earth Orthoferrites*, Sov. Phys. JETP **49**, (1979).

[168] A. V. Kimel, C. D. Stanciu, P. A. Usachev, R. V. Pisarev, V. N. Gridnev, A. Kirilyuk, and T. Rasing, *Optical Excitation of Antiferromagnetic Resonance in TmFeO3*, Phys. Rev. B - Condens. Matter Mater. Phys. **74**, 1 (2006).

[169] J. A. De Jong, I. Razdolski, A. M. Kalashnikova, R. V. Pisarev, A. M. Balbashov, A. Kirilyuk, T. Rasing, and A. V. Kimel, *Coherent Control of the Route of an Ultrafast Magnetic Phase Transition via Low-Amplitude Spin Precession*, Phys. Rev. Lett. **108**, 1 (2012).

[170] E. A. Turov and V. E. Naish, *On the Theory of Weak Ferromagnetism in Rare-Earth Orthoferrites*, Fiz. Met. Met. **9**, (1960).

[171] R. P. Feynman, F. L. Vernon, and R. W. Hellwarth, *Geometrical Representation of the Schrödinger Equation for Solving Maser Problems*, J. Appl. Phys. **28**, 49 (1957).

[172] E. Li, Z. Feng, B. Kang, J. Zhang, W. Ren, and S. Cao, *Spin Switching in Single Crystal PrFeO3 and Spin Configuration Diagram of Rare Earth Orthoferrites*, J. Alloys Compd. **811**, 152043 (2019).

[173] D. N. Zubarev, *Nonequilibrium Statistical Thermodynamics*, Consultant (New York, 1974).

[174] V. G. Baryakhtar, *Phenomenological Description of Relaxation Processes in Magnets*, Zh. Eksp. Teor. Fiz. **87**, 1501 (1984).

[175] V. G. Baryakhtar, *Phenomenological Description of Exchange Relaxation Processes in Antiferromagnets*, Fiz. Nizk Temp. **11**, 1198 (1985).

[176] V. G. Bar'yakhtar, *Crystal Symmetry and the Structure of the Relaxation Terms in the Antiferromagnet Dynamic Equations of Motion*, Zh. Eksp. Teor. Fiz **94**, 196 (1988).

[177] V. G. Bar'yakhtar and A. G. Danilevich, *Dissipation Function of Magnetic Media*, Low Temp. Phys. **36**, 303 (2010).

[178] E. V. Gomonay and V. M. Loktev, *Spintronics of Antiferromagnetic Systems (Review Article)*, Low Temp. Phys. **40**, 17 (2014).

[179] G. F. Herrmann, *Resonance and High Frequency Susceptibility in Canted Antiferromagnetic Substances*, J. Phys. Chem. Solids **24**, 597 (1963).

[180] G. F. Herrmann, *Magnetic Resonances and Susceptibility in Orthoferrites*, Phys. Rev. **133**, (1964).

[181] B. A. Ivanov, *Spin Dynamics of Antiferromagnets under Action of Femtosecond Laser Pulses (Review Article)*, Low Temp. Phys. **40**, 91 (2014).

[182] A. P. Malozemoff, *The Optical Spectrum and Magnetic Properties of TmFeO3 in the Single-Ion Model*, J. Phys. Chem. Solids **32**, 1669 (1971).

[183] H. H. Zhang, Zhenya, Minoru Kanega, Kei Maruyama, Takayuki Kurihara, Makoto Nakajima, Takehiro Tachizaki, Masahiro Sato, Yoshihiko Kanemitsu, *Spin Switching in Sm0.7Er0.3FeO3 Triggered by Terahertz Magnetic-Field Pulses*, Nat. Mater. 1 (2024).

[184] V.G. Baryakhtar, *Crystal Symmetry and Structure of Relaxation Terms in Ferromagnetics.*, Zh. Eksp. Teor. Fiz. **94**, 196 (1988).

[185] G. A. Gehring and K. A. Gehring, *Co-Operative Jahn-Teller Effects Co-Operative Jahn-Teller Effects*, Rep. Prog. Phys. **38**, (1975).

[186] H. A. Jahn and E. Teller, *Stability of Polyatomic Molecules in Degenerate Electronic States. I. Orbital Degeneracy*, Proc. Roy. Soc. **161**, 220 (1937).

[187] S. Venugopalan, M. Dutta, A. K. Ramdas, and J. P. Remeika, *Raman Scattering Study of Magnons at the Spin-Reorientation Transitions of TbFeO3 and TmFeO3*, Phys. Rev. B **27**, 3115 (1983).

[188] O. Nikolov, I. Hall, S. N. Barilo, and S. A. Guretskii, *A Mossbauer Study of Temperature-Driven Spin-Reorientation Transitions in TbFeO3*, J. Phys. Condens. Matter **6**, 3793 (1994).

[189] J. Mareschal, J. Sivardière, G. F. De Vries, and E. F. Bertaut, *Magnetic Ordering of Terbium in Some Perovskite Compounds*, J. Appl. Phys. **39**, 1364 (1968).

[190] T. N. Stanislavchuk, Y. Wang, S. W. Cheong, and A. A. Sirenko, *Far-IR Magnetospectroscopy of Magnons and Electromagnons in TbFeO3 Single Crystals at Low Temperatures*, Phys. Rev. B **95**, 1 (2017).

[191] S. Venugopalan, M. Dutta, A. K. Ramdas, and J. P. Remeika, *Raman Scattering Study of Magnons at the Spin-Reorientation Transitions of TbFeO3 and TmFeO3*, Phys. Rev. B **27**, (1983).

[192] A. M. Balbashov, G. V. Kozlov, A. A. Mukhin, and, A. S. Prokhorov, *Submillimeter Spectroscopy of Antiferromagnetic Di- Electrics: Rare-Earth Orthoferrites*, in *High Frequency Processes in Magnetic Materials*, edited by G. Srinivasan and A. Slavin (World Scientific, Singapore, 1995), pp. 56–98.

[193] A.K. Zvezdin, A.A. Mukhin, A.I. Popov, *Level Crossing and Instability of Magnetic Structure in Rare-Earth Iron Garnets*, JETP **45**, 573 (1977).

[194] P. Forn-Díaz, L. Lamata, E. Rico, J. Kono, and E. Solano, *Ultrastrong Coupling Regimes of Light-Matter Interaction*, Rev. Mod. Phys. **91**, 25005 (2019).

[195] A. S. P. A. M. Balbashov, G.V. Kozlov, S. P. Lebedev, A. A. Mukhin, A. Yu. Pronin, *Anomalies of High-Frequency Magnetic Properties and New Orientational Transitions in HoFeO3*, Sov. Phys. JETP **68**, (1989).

[196] N Koshizuka and K Hayashi, *Raman Scattering from Magnon Excitations in RFeO3*, J. Phys. Soc. Japan **57**, (1988).

[197] K. B. Aring and A. J. Sievers, *Role of the Ytterbium Spins in the Spin*

Reorientation in YbFeO3, J. Appl. Phys. **41**, 1197 (1970).

[198] F. T. M. Guillot, A. Marchand, V. Nekvasil, *Step-like Magnetization Curves in Tb3Ga5O12*, J. Phys. C Solid State Phys. **18**, 3547 (1984).

[199] J. B. Gruber et al., *Analyses of the Optical and Magneto-Optical Spectra of Tb3 Ga5 O12*, J. Appl. Phys. **101**, (2007).

[200] A. B. Villaverde, D. A. Donatti, and D. G. Bozinis, *Terbium Gallium Garnet Verdet Constant Measurements with Pulsed Magnetic Field*, J. Phys. C Solid State Phys. **11**, (1978).

[201] P. Thalmeier, *Paramagnetic Acoustic Faraday Rotation in Tb3 Ga5 O12*, Phys. Rev. B - Condens. Matter Mater. Phys. **80**, 1 (2009).

[202] A. Sytcheva, U. Löw, S. Yasin, J. Wosnitza, S. Zherlitsyn, P. Thalmeier, T. Goto, P. Wyder, and B. Lüthi, *Acoustic Faraday Effect in Tb3Ga5O12*, Phys. Rev. B - Condens. Matter Mater. Phys. **81**, 5 (2010).

[203] U. Löw, S. Zherlitsyn, K. Araki, M. Akatsu, Y. Nemoto, T. Goto, U. Zeitler, and B. Lüthi, *Magneto-Elastic Effects in Tb3Ga5O12*, J. Phys. Soc. Japan **83**, 1 (2014).

[204] C. Strohm, G. L. J. A. Rikken, and P. Wyder, *Phenomenological Evidence for the Phonon Hall Effect*, Phys. Rev. Lett. **95**, 1 (2005).

[205] A. V. Inyushkin and A. N. Taldenkov, *On the Phonon Hall Effect in a Paramagnetic Dielectric*, JETP Lett. **86**, 379 (2007).

[206] J. Hamman, P. Manneville, *Ordre Magnétique Électronique Induit Par Les Interactions Hyperfines Dans Les Grenats de Gallium-Holmium et de Gallium-Terbium*, J. Phys. Fr. **34**, 615 (1973).

[207] R. R. Subkhangulov, R. V. Mikhaylovskiy, A. K. Zvezdin, V. V. Kruglyak, T. Rasing, and A. V. Kimel, *Terahertz Modulation of the Faraday Rotation by Laser Pulses via the Optical Kerr Effect*, Nat. Photonics **10**, 111 (2016).

[208] R. V. Mikhaylovskiy, R. R. Subkhangulov, T. Rasing, and A. V. Kimel, *Colossal Magneto-Optical Modulation at Terahertz Frequencies by Counterpropagating Femtosecond Laser Pulses in Tb_3Ga_5O_12*, Opt. Lett. **41**, 5071 (2016).

[209] R. V. Mikhaylovskiy, E. Hendry, F. Y. Ogrin, and V. V. Kruglyak, *Low-Temperature Time-Domain Terahertz Spectroscopy of Terbium Gallium Garnet Crystals*, Phys. Rev. B - Condens. Matter Mater. Phys. **87**, 1 (2013).

[210] A. H. M. Reid, A. V. Kimel, A. Kirilyuk, J. F. Gregg, and T. Rasing, *Investigation of the Femtosecond Inverse Faraday Effect Using Paramagnetic Dy3Al5O12*, Phys. Rev. B - Condens. Matter Mater. Phys. **81**, 1 (2010).

[211] J. A. Koningstein and G. Schaack, *Electronic Raman Spectrum and Crystal Field of the Terbium Ion in Terbium Aluminum Garnet*, Phys. Rev. B **2**, 1242 (1970).

[212] D. Nicollin, J.A. Koningstein, *Interferences in and Lifetime Measurement of a Resonance Electronic Raman Effect Using Tunable Pulsed Laser Techniques*, Chem. Phys. **49**, 377 (1980).

[213] C. Kurtscheid, A. Redmann, F. Vewinger, J. Schmitt, and M. Weitz, *Thermodynamics and State Preparation in a Two-State System of Light*, ArXiv:2411.14838 1 (2024).